

AUTOCATALYSIS OF MARTENSITIC TRANSFORMATION

by

GERALD ALBERT KNOROVSKY

Sc.D.

III

February 1977

AUTOCATALYSIS OF MARTENSITIC TRANSFORMATIONS

By

GERALD ALBERT KNOROVSKY

B.S., Illinois Institute of Technology
1970

Submitted in partial fulfillment of the requirements
for the degree of
DOCTOR OF SCIENCE
at the
Massachusetts Institute of Technology
February 1977

Signature of Author.....*Gerald A. Knorovsky*
Department of Materials Science and
Engineering
January 13, 1977
Certified by.....*John H. Cohen*
Thesis Supervisor
Accepted by.....
Chairman, Department Committee on Graduate
Students

AUTOCATALYSIS OF MARTENSITIC TRANSFORMATIONS

by

GERALD ALBERT KNOROVSKY

Submitted to the Department of Materials Science and Engineering on January 13, 1977 in partial fulfillment of the requirements for the degree of Doctor of Science.

A technique involving the reaction of samples which contain a gradient in chemical driving force is used to study the phenomenon of martensitic autocatalysis in burst-type alloys. The chemical driving-force gradient is produced either by reacting a homogeneous sample in a temperature gradient or a uniformly-cooled sample containing a composition gradient.

By measuring the temperature and composition at the initial (M_b) and terminal nucleation events, values for the chemical driving force at both events can be obtained. The difference between these values is an energetic measure of the effect of autocatalysis.

In single-crystalline samples the region of renucleation above the M_b is amenable to metallographic analysis of the habit-plane variants which form the autocatalytic motifs. Thus both energetic and phenomenologic data are obtained from the same experiment.

In Fe-31 Ni single crystals, the value of the energetic assist is 55 cal/mole (230 J/mole); in Fe-24.4 Ni-0.44 C, it is 61 cal/mole (255 J/mole). In polycrystalline samples, the autocatalytic assist increases with increasing grain size, until it reaches a maximum value about 60% of the single-crystalline value.

By comparing the energy-assist value measured in Fe-31 Ni single crystal experiments (55 cal/mole, 230 J/mole) with that available due to a stress assist acting upon pre-existing nuclei (25.5 cal/mole, 107 J/mole), it is concluded that stress-activation of pre-existing nuclei is not the controlling mechanism. Part of the autocatalytic assist can thus be explained by the creation of higher-than-normal-potency nuclei. Two modes of nuclei production were tested to see if they could account for the autocatalytic motifs observed metallographically. One model, which relies upon the interface between the parent and martensitic phases, was not confirmed; another model, relying upon the dislocations produced by the accommodation deformation in the parent phase, did produce results consistent with experiment.

Based on the conclusion that autocatalysis was due to stress-activation of higher-than-normal-potency nuclei produced by accommodation deformation of the parent phase, the existence of this effective (burst) type autocatalysis appears due to satisfaction of three necessary conditions:

1. Good coupling between variants must be possible.
2. Appreciable numbers of autocatalytic nuclei must be produced.
3. Of those nuclei produced, some must be ones which result in habits with good coupling to the original variant.

In addition to the maximum temperature of nucleation, the single-

crystalline specimens allow measurement of the maximum temperature of growth. Depending upon whether the growth arrest takes place adiabatically or isothermally (which was tentatively decided upon), the minimum chemical driving force for growth varies between ≈ 100 cal/mole (420 J/mole) to 225 cal/mole (940 J/mole).

The variation of the autocatalytic assist with composition and temperature correlated well with the flow stress, while the variation of the minimum driving force for growth correlated with the elastic modulus.

In the polycrystalline samples, M_b was not found to be a function of grain size, but remained constant. ^b Some evidence was found for spurious effects which could give rise to an apparent austenitizing temperature (or grain size) dependence.

Thesis Supervisor: Morris Cohen
Title: Institute Professor

TABLE OF CONTENTS

Abstract	2
List of Figures	6
List of Tables	9
Acknowledgements	10
Chapter I Introduction and Literature Survey	11
Chapter II Purpose of Present Investigation	21
Chapter III Experimental Procedures	23
Choice of Alloys	23
Preparation of Specimens and Heat Treatment	23
Thermal Gradient Apparatus and Measurement	28
Techniques	
Habit Plane Measurements	34
Preparation of Composition-Gradient Specimens	39
Transformation of Composition-Gradient	40
Samples	
Analysis of Composition Gradients	40
Chapter IV Experimental Results	42
Thermodynamic Data	42
Metallographic Data	47
Thermodynamic Driving Forces	66
Chapter V Discussion of Results	68
Introduction	68
Heat-Flow Considerations	68
M_b Data Scatter	72

	Qualitative Metallographic Observations	73
	Implications of the Energy-Assist Due to Autocatalysis	74
	Implications of Metallographic Data	87
	Overview and Implications of Autocatalysis	100
	Composition Gradient Results	106
	Polycrystalline Results	111
	Implications of the Minimum Driving Force for Growth	116
Chapter VI	Conclusions	123
Chapter VII	Suggestions for Further Research	124
Appendix I	Autocatalysis via the Stress-Assisted Strain-Induced Nuclei Mechanism	125
Appendix II	Interfacial Renucleation Model	131
Appendix III	Martensitic Burst Temperature vs Austenitic Grain Size	134
	Bibliography	146
	Biographical Note	147

LIST OF FIGURES

Figure No.		Page No.
1.	Temperature gradient device	29
2.	Very low M_b temperature gradient device	33
3.	Device used for uniform cooling	35
4.	Habit plane determination technique	38
5.	$\Delta T (= T_{\max}^{\text{rn}} - M_b)$ vs grain size (alloy 3)	45
6.	$\Delta T (= T_{\max}^{\text{rn}} - M_b)$ vs grain size (alloy 4)	46
7.	Metallographic panoramas of specimen 1 (alloy 1)	49
8.	Results of metallographic habit plane analysis of specimen 1 (alloy 1)	50
9.	Metallographic panoramas of specimen E (alloy 1)	51
10.	Results of metallographic habit plane analysis of specimen E (alloy 1)	52
11.	Metallographic panoramas of specimen G (alloy 1)	53
12.	Results of metallographic habit plane analysis of specimen G (alloy 1)	54
13.	Metallographic panoramas of specimen Z2 (alloy 1)	55
14.	Results of metallographic habit plane analysis of specimen Z2 (alloy 1)	56
15.	Metallographic panoramas of specimen F (alloy 2)	57
16.	Results of metallographic habit plane analysis of specimen F (alloy 2)	58
17.	Metallographic panoramas of specimen H (alloy 2)	59

<u>Figure No.</u>		<u>Page No.</u>
18.	Results of metallographic habit plane analysis of specimen H (alloy 2)	60
19.	Metallographic panoramas of specimen X1 (alloy 2)	61
20.	Results of metallographic habit plane analysis of specimen X1 (alloy 2)	62
21.	Metallographic panoramas of specimen Y2 (alloy 2)	63
22.	Results of metallographic habit plane analysis of specimen Y2 (alloy 2)	64
23.	Composition gradient specimens	65
24.	A method of obtaining "multiple" midribs	75
25.	Olson-Cohen nucleus dislocation elements	82
26.	Possible autocatalytic sequences via "parallel coupling" leading to 4-habit variant motifs	91
27.	Possible autocatalytic sequence via "perpendicular coupling" leading to 8-habit variant motif	92
28.	A stereographic projection indicating the 8 habit variants of "perpendicular coupling" and a simulated metallographic section showing how it leads to the zig-zag arrays characteristic of burst martensites	93
29.	Autocatalytic sequence using second-shear dislocation as first-shear dislocation for autocatalytic variant	95
30.	Autocatalytic sequence using "edge" component of interfacial dislocations for the first-shear dislocation of the autocatalytic variant	96

<u>Figure No.</u>		<u>Page No.</u>
31	Autocatalytic sequence using "screw" component of interfacial dislocations for first-shear dislocation of autocatalytic variant (screw dissociates in second-shear plane of original variant)	97
32.	Same as Fig. 31 except screw dissociates on first-shear plane of original variant	98
33.	Coupling factors between (2- 2+ 5) and other (2 2 5)-type variants	102
34.	Coupling factors between (3 10 15) and other (3 10 15)-type variants	103
35.	Selected coupling factors between (3 3 1)-type habit variants	105
36.	Temperature gradient results for alloy 4 superimposed upon composition gradient results modified as noted in text	108
37.	$\Delta T (=T_{\max}^{\text{rn}} - M_b)$ and $\rho\bar{V}/5$ vs grain size for alloy 4	115
38.	Approximation to determine the minimum driving force for growth under adiabatic conditions	119
39.	M_b vs grain size (alloy 3)	140
40.	M_b vs austenitizing temperature (alloy 3)	141

LIST OF TABLES

<u>Table No.</u>		<u>Page No.</u>
1.	Alloy compositions	24
2.	Compilation of single-crystal temperature-gradient data obtained from metallographic panoramas	43
3.	Chemical driving-force values	44
4.	Compilation of composition-gradient data obtained from metallographic panoramas and microprobe results	48
5.	Dislocation elements of Olson-Cohen martensitic nucleation site	83
6.	Coupling factors calculated by Bokros and Parker modified to refer to (3 10 15) instead of (10 3 15)	84
7.	Coupling factors for slip systems (absolute values) activated by a (3 10 15) martensite plate	89
8.	Composition gradient driving forces using modified microprobe results	109

ACKNOWLEDGEMENTS

Though the title page of this thesis bears only the author's name, it should be obvious that many people actually participated in its conception and accomplishment.

Without much encouragement and guidance by Prof. Morris Cohen this work could never have been completed; without stimulating discussions with faculty and graduate students at M.I.T. too numerous to mention, the author could not have attained a necessary grasp of the concepts involved. Especial thanks are intended for Prof. J.W. Cahn, Dr. G.B. Olson, Dr. R.J. Salzbrenner, A.K. Sachdev, and M.L. Green.

The experimental assistance of Ms. M. Rich must be acknowledged, as without it, the author would still be in the lab with no end in sight. The capable aid of Mr. J. Adario must also be mentioned.

Beyond the confines of the lab, the liberal (or sometimes, conservative) education of the author was furthered by discussion on a wide range of subjects. Especial gratitude must be extended to Ms. M.A. Meyer, D. and A. Patten, P. and S. DeCicco, J. Clow, and F. Smith for their warm friendship.

Financial assistance from the N.S.F. and O.N.R. were essential during the past few years, and must also be acknowledged.

Finally, without the presence, encouragement, and love of the author's spouse, Margery, life would have been much less satisfying and rewarding.

CHAPTER I

INTRODUCTION AND LITERATURE SURVEY

Martensitic phase transformations have been described in the past as "military" in character.⁽¹⁾ This choice of word emphasizes the coordinated nature of the atomic motions required for the parent phase to form a single region of martensite. On another level, however, the term is also appropriate when one considers the formation of groups of martensitic units (referred to as "plates" hereafter). Because of the shear-like nature of the transformation, the immediate vicinity of a plate is disturbed quite severely by a combination of elastic and plastic deformation processes. Thus, it is likely that the nucleation and growth of succeeding plates will tend either to minimize the work involved in growth or to utilize the energy already expended to nucleate new plates of martensite in a very cooperative manner. Such succeeding generations of plates which take advantage of (a) the strain energy transferred to the surrounding matrix, or (b) the defects generated by the occurrence of plastic accommodation, or (c) the transformation interface itself, are said to be autocatalytically stimulated. By comparing the numbers of pre-existing nucleation sites with the total number of martensite plates obtained, it is found that autocatalysis is essential for the formation of much of the martensite that is actually produced.

The small-particle experiments of Cech and Turnbull⁽²⁾ demonstrated the heterogeneous nature of martensitic transformations. Such behavior raises an important question: If martensite nucleates heterogeneously, what are the heterogeneities and how many of them are necessary to obtain the observed numbers of martensitic plates?

Magee⁽³⁾ has estimated that about 2×10^6 plates/cm³ are necessary for detection of M_s at the 0.1% transformation level. Simple multiplication of this number by 1000 for complete transformation, yields a value of 2×10^9 sites/cm³. This is an underestimate because the average volume per plate⁽⁴⁾ (taken as 5×10^{-10} cm³ for an austenitic grain size of 80 microns), while remaining reasonably constant for a good part of the transformation range,^(5,6) must eventually decrease due to partitioning, especially towards completion in plate-type martensites.

Others^(4,7-10) have made estimates ranging from $10^5 - 10^7$ sites per cm³ for the number of pre-existing nucleation sites, based on attempts to fit isothermal nucleation-rate theories to experimental data. Recently, Olson and Cohen⁽¹¹⁾ re-analyzed the small-particle experiments of Cech and Turnbull⁽²⁾ to calculate the density of operable nucleation sites pre-existing in the parent phase (Fe-30.3 w/o Ni) as a function of undercooling below M_s . These data indicate that the density of nucleation sites is approximately 10^6 /cm³ at M_s , and increases to about 10^8 sites/cm³ at the liquid-nitrogen temperature. One sees immediately that the pre-existing sites are at least an order of magnitude fewer in number than the plates actually obtained.

The experiments on isothermal nucleation rates also provide a quantity called the autocatalytic factor, which tries to compensate for the discrepancy between the number of sites originally present and the observed numbers of martensitic plates. This is a coefficient which yields the number of autocatalytic nucleation sites made available by prior transformation when multiplied by the fraction transformed, and is determined by curve-fitting a theoretical equation to experimental results. The

autocatalytic factor is one of two disposable parameters in this analysis, the other being the activation energy. Values of the autocatalytic factor are essentially temperature independent, lying in the range of 0.45-1.2

$$\times 10^{10} / \text{cm}^3 \quad (5)$$

Other authors have commented upon the importance of autocatalysis in martensitic transformations, ^(7,10,12) but have not distinguished between less-potent pre-existing sites which may be autocatalytically triggered and new sites which may be freshly created. Comparison of the total number of pre-existing operable nucleation sites (based on the small-particle data) with other experiments showing the number of martensitic plates actually formed indicates that newly-created nucleation sites are quite important to the kinetics of martensite formation.

While autocatalysis is seen to be significant in many, although not necessarily all, martensite transformations, its presence is most clearly demonstrated in alloys which exhibit "burst" transformations. In such cases, a large amount of martensite, up to as much as 60-75%, forms in milliseconds. Examples of alloy systems which show burst behavior are: Fe-Ni, Fe-Ni-C, ⁽¹³⁾ Fe-Ni-Cr-C, ⁽¹⁴⁾ Fe-Ni-Co, ⁽¹⁵⁾ Cu-Zn, ⁽¹⁶⁾ Cu-Sn. ⁽¹⁷⁾ The compositions are usually such that M_s is below or around the ambient temperature.

Machlin and Cohen ⁽¹³⁾ coined the word "burst" in this connection, but the actual discovery of these sudden transformations seems to date back to work done earlier by Scheil and co-workers. ^(18,19) Acoustic emissions during the burst appear to have been the first evidence noted, as suggested by the word "umklapp" applied to this type of martensitic transformation. The earliest evidence found by this author for such acoustic events is due

to Benedicks,⁽²⁰⁾ who cooled a high-carbon (1.99 w/o C, 0.42 w/o Mn) steel to the liquid-air temperature, and upon removing the sample from the bath heard clicking noises while the sample warmed back to room temperature. Possibly this alloy exhibited isothermal martensitic behavior, or else the thermal expansion of the outer shell of the sample released internal stresses which had restrained the transformation on cooling.

Though it was suggested by Scheil's work⁽²¹⁾ that mechanical stresses play an important part in the transformation, it was not until Machlin⁽²²⁾ that any explanation for the burst behavior was forthcoming. Part of his research involved the determination of habit planes and macroscopic shear directions, and he found that the (2 5 9)-type of martensite had the possibility of reducing back stresses by cooperatively transforming to allow regions of austenite to undergo translation rather than shear. Extending this argument, he noted that (2 2 5)-type martensites had less ability for cooperatively accommodating the transformation strain, and thus he explained their reduced bursting tendencies. Also, he postulated that momentum generated by the transformation, and which would be used in this mechanical coupling, might be the determining factor in establishing the burst temperature M_b . If not enough momentum is available, the autocatalytic burst will not result, but by cooling further the momentum can be increased.

These ideas were introduced because he had detected small amounts of martensite (~0.5%) above M_b . However, surface martensite offers an alternative explanation for the precursor martensite.⁽²³⁾

Machlin's analysis of the motions of the austenite adjacent to the various martensitic plates proved to be correct, though unwieldy because the orientation of the plate intersections was a necessary consideration. The

austenite could be moved in opposite directions depending upon whether or not one was "above" or "below" the plate in question. Bokros and Parker's analysis⁽²⁴⁾ of the same question was a great simplification because they treated the shear strains rather than the shear directions. In their paper, they basically performed a Schmid factor analysis.⁽²⁵⁾ The operative stress was that stress which they assumed would be set up in the austenite around a given plate, and their shear systems were the macroscopic shears of all the other possible martensitic-plate variants. The resulting Schmid factor, which they called the "coupling factor," indicated whether the subsequent formation of a specific habit variant in the vicinity of the original plate was then favored or hindered. The experimental verification showed that groups of four plates with their habits in the four unit triangles adjacent to a common $\langle 110 \rangle$ direction were favored. These groups did not have the highest coupling factors, but they did have large positive ones. The group of four about a common $\langle 110 \rangle$ direction was also consistent with Machlin's analysis, although this was not expressed explicitly.

Entwistle⁽²⁶⁾ adapted the theory of isothermal martensitic nucleation to the problem by suggesting that autocatalysis activates immediately all the embryos available; thus, he calculates the saturation value of martensite expected to form isothermally over long times as the measure of autocatalytic transformation during cooling. This theory, however, relies upon an autocatalytic factor which is strongly temperature dependent. In isothermally transforming alloys at least, this is contradictory to the experimental findings.⁽⁵⁾ Magee's small-particle experiments on a bursting alloy⁽⁹⁾ (which showed isothermal behavior in the absence of

autocatalysis), do not lead to a strong temperature dependence for the autocatalytic factor, either.

Patel and Cohen⁽²⁷⁾ analyzed the energetics of stress-aided martensite formation and their results predict that the M_s temperature for a given plate should be raised by uniaxial tensile or compressive stresses and depressed by hydrostatic compressive stresses. Their argument involves calculating the mechanical work done by the applied stress on the plate in question and using it with the chemical driving force. On the other hand, a number of investigators have conducted experiments determining the effect of applied stress on M_s with conflicting results.^(15,21,27-31,39) The resolution of the conflict does not seem obvious. The evidence accumulated seems to indicate that M_s is, indeed, raised by elastic stresses, though not necessarily at the rate predicted by Patel and Cohen.

It has also been established that the application of elastic stress during transformation serves to stimulate the transformation rate.⁽²²⁾ Thus, the application of elastic stress can be expected to shift the entire transformation curve, not just the M_s .

Increasing the stress level to the point where plastic deformation occurs induces martensitic transformation in a temperature range well above M_s (as much as 270°C). Nevertheless, above a temperature called M_d , martensite cannot be produced by plastic deformation.⁽³²⁾ Well before that temperature has been reached, the morphology of the martensite changes from the regular type found on cooling, to a fine lath or stringer-type associated with deformation bands in the austenite.⁽³³⁾ This rather distinct change in morphology is found at about 70°C above the M_s . Some investigators report M_d as being only about 70-80°C above M_s .^(24,28,34)

It is not clear whether they did not detect martensite above this temperature because of its morphology, or relative scarcity, or because the mode of transformation which acts at these relatively high transformation temperatures is actually suppressed in some alloys.

Plastic deformation of the austenite in a temperature regime where deformation-induced martensite is not produced can either stimulate subsequent transformation^(22,24) on cooling, or inhibit it.^(21,28,35) Apparently the amount and character of the deformation, and the substructure generated, are controlling factors. There is also a question as to whether some deformation-induced martensite might be formed but not detected. The presence of such martensite and the possibility of thermal stabilization in interstitial-containing alloys could have a profound influence on any subsequently measured M_s , aside from possible direct effects of the deformation per se.

The martensite-austenite interface also plays a very important role in the transformation. At the nucleation stage, interfacial energy acts as a barrier to nucleation, and during growth the nature of the interface must allow freely glissile movement. Speculation on whether the energetics of interfacial movement⁽³⁶⁾ or growth⁽³²⁾ controls nucleation has shaped some recent theories of martensitic nucleation. The loss of coherence has been suggested as the reason for the cessation of growth of martensite plates.⁽³⁷⁾ A recent theory due to Olson and Cohen⁽³⁸⁾ envisages the possibility of an interfacial type of autocatalysis, where dislocations in the interface can act to nucleate other plates of martensite.

A few models of the interface have been proposed to explain crystallographic^(39,40) or growth-rate⁽⁴¹⁾ data; however, because of experimental

difficulties, not much work has been done in determining the actual mobility or structure of the interface. Suggestions have been made that since the interface must be composed of dislocation arrays, it should behave similarly.⁽⁴²⁾ Yet, one might expect some dissimilarities, and any direct information obtained as to interfacial structure or mobility will be welcome.

The crystallographic aspects of martensitic transformations have been extensively studied,⁽⁴³⁻⁴⁵⁾ and the orientation relationships and shear directions for a given habit plane are amenable to measurement. Most theories of martensitic nucleation have not been sufficiently detailed to include or explain this information, concentrating instead upon the energetics and kinetics of the reaction.

Olson and Cohen⁽³⁸⁾ have recently proposed a theory of martensitic nucleation which incorporates both crystallographic and energetic phenomena. Because of this, it can be tested against the measured autocatalytic groupings observed by Bokros and Parker,⁽²⁴⁾ De Philippi,⁽⁴⁶⁾ and in the present work. Their model of the martensitic nucleus and the dislocations necessary to produce it uses the Bogers-Burgers two-shear mechanism⁽⁴⁷⁾ for generating a bcc lattice from an fcc parent. This mechanism is similar to a number of others proposed for the fcc-bcc lattice change⁽⁴⁸⁻⁵¹⁾ in that the first shear is of the type $(111) [\bar{1}21]$. It differs in its magnitude, and in the choice of a second shear system.

Starting from a theory which accounts for the temperature variation of stacking-fault energy in terms of the relative chemical free energy of the parent phase and that of a second phase which is effectively created by the stacking fault (for example, a stacking fault in fcc on (111) can be

thought of as a two-atom-layer volume of hcp), Olson and Cohen develop a model for martensitic nuclei and then derive the criterion for growth of these nuclei.

One advantage of their nucleation mechanism is that the nuclei can arise from normal lattice dislocations, and the presence of elaborate "frozen-in" embryos⁽³⁰⁾ becomes unnecessary. The effective nucleation site consists of four or five dislocations vertically stacked three atom planes apart. Further specific details of this theory will be given in interpreting the results of this thesis.

Inasmuch as the experiments conducted in the present investigation rely upon gradients of one kind or another, it is desirable to review the previous work incorporating gradients at this time.

Some early work by Hanneman et al.⁽⁵²⁾ noted that, in samples surface decarburized during heat treatment, the density of martensite at the surface was higher than in the center. This result is explained easily by the gradient in composition and thus driving force.

Several years later, in their studies of the effect of stress on M_s , Kulin et al.⁽²⁹⁾ transformed samples subjected to elastic bending. Because of the gradient in stress (and thus driving force), the transformation occurred preferentially in the surface region under tension, and propagated only part-way into the central region of the sample.

Honma⁽⁵³⁾ transformed a single crystal sample in a temperature gradient, and found that martensite propagated to a temperature 85-90°C above the normal M_s (-45°C) of the alloy (Fe-31 Ni). He interpreted his results in terms of the kinetic energy generated during transformation being able to sustain the reaction to higher-than-normal temperatures. In the same

series of experiments, Honma artificially induced a burst of transformation in a sample by locally cooling it with liquid air while the remainder was at a uniform higher temperature, and he observed the highest temperature at which the burst would occur. He compared this temperature (-15°C) to that extrapolated from measurements of the temperature recalescence (proportional to burst size) as a function of M_b during normal cooling experiments. The extrapolation was made to the point where there was no rise in temperature, and this yielded -25°C , thus constituting fairly good agreement between the two values.

Entwisle and Feeney⁽⁵⁴⁾ also applied the technique of artificially stimulating a burst (by mechanical means) above the normal M_b to determine the effect of austenitizing conditions and grain size upon the magnitude of the burst in a series of Fe-Ni-C alloys. They found a C-curve behavior. At the highest burst temperature, produced by high temperature austenitizing treatments, the burst size was small. As the burst temperature decreased, and thus the chemical driving force increased, the burst magnitude grew until at the very lowest burst temperatures it diminished again, due to the small grain sizes resulting from the lower austenitizing temperatures employed.

Bokros and Parker⁽²⁴⁾ attempted to transform one of their deformed austenite single crystals in a temperature gradient, but the extent of the gradient (about 25°C) was not enough to note the cessation of renucleation up the gradient. In their experiment, transformation appeared uniform along the length of their sample.

The foregoing gradient experiments suggested the feasibility of the course of experimentation undertaken in this thesis.

CHAPTER II

PURPOSE OF PRESENT INVESTIGATION

It is the purpose of this work to measure quantitatively the autocatalytic assist in the nucleation of succeeding generations of martensitic plates. The manner in which this is to be accomplished is to start the martensitic transformation in the normal manner by cooling part of a specimen to its M_s temperature and then allowing the reaction to propagate as far as it can into regions where the chemical driving force is deliberately reduced by a temperature or composition gradient. By calculating the difference in chemical driving force at the initial nucleation event and the terminal nucleation event, the magnitude of the energy assist can be determined.

In the case where a single crystal has been thus reacted, additional information about distinct habit-plane spatial groupings within the autocatalytic chains can be obtained by metallographic serial sectioning techniques. Also, because the reaction is unimpeded by grain boundaries or other barriers, the growth of an individual martensite plate can continue until the energetics of its interfacial growth mechanism dictate a halt. Hence, the minimum chemical driving force for growth can be measured.

The information gathered from single-crystal experiments can be thought of as applying to processes which take place in the grain interiors. It is also desirable to consider the propagation of the transformation across grain boundaries. To this end, a series of temperature-gradient experiments will be conducted on samples of varying grain size, obtained by austenitizing at different temperatures. In these poly-crystalline experiments, the possibility arises of two separate rate-controlling steps. In

one, grain-interior processes may control, while in the other, boundary-crossing processes may control.

By obtaining both phenomenologic and thermodynamic information about autocatalysis in single and polycrystals, and comparing it with the predictions of theoretical models it is hoped that a much clearer picture can be achieved concerning the relative importance and validity of various autocatalytic mechanisms.

CHAPTER III

EXPERIMENTAL PROCEDURES

Choice of Alloys

The alloys selected for the temperature-gradient portion of this work were typical of burst-type transformations. Since the efficiency of the experimental technique was not established in non-burst alloys, it was reasoned that a first investigation of martensitic autocatalysis should begin with systems where its magnitude is known to be large. An additional constraint was the necessity of having the M_b temperature well below ambient so that up-quenching to room temperature would eliminate the possibility of further martensite formation. Finally, the compositions chosen had to be sufficiently well studied that the thermodynamic driving force could be calculated as a function of temperature.

These criteria were all met by the Fe-Ni and Fe-Ni-C systems. Suitable alloys were already available from reliable sources, and in single-crystalline form as well as polycrystalline. Two of the alloys (numbers 1 and 2) were supplied by F. X. Kayser of Iowa State University (as cylindrical ingots 25 mm diameter x 40 mm long and 20 mm diameter x 25 mm long, respectively) in very large polycrystalline form, suitable for cutting out single-crystalline samples of adequate size; and the remaining two (numbers 3 and 4) were received from W. S. Owen. Compositions of the alloys are listed in Table 1.

Preparation of Specimens and Heat Treatment

Alloy 1 (Fe-24Ni-0.44C) had already received an anneal of 133 hours at 1200°C for homogenization purposes, so samples were taken from it

Table 1

Alloy compositions

	Fe (w/o)	Ni (w/o)	C (w/o)
Alloy 1	bal.	24.43	0.441
Alloy 2	bal.	30.93	0.004
Alloy 3	bal.	30.89	0.290
Alloy 4	bal.	31.32	0.004

The carbon analysis was determined by a Leco combustion-type apparatus with 1-gram samples.

The nickel analysis was carried out by wet chemical procedures per ASTM E-38.

without further heat treatment. Slices were cut from the annealed ingot with an abrasive wheel, and were then ground carefully on silicon carbide papers to reduce the damaged layer. Samples approximately 25 mm x 1.5 mm x 1.5 mm were then spark-machined from these slices and extensively electropolished, removing at least 0.1 mm from all surfaces, and even more at the ends due to the accelerated electropolishing action at the sample corners.

The Fe-31Ni single crystal (alloy 2) was not fully homogenized when received; it had been given a treatment of 24 hours at 1000°C, and contained several grains of about 1 cm diameter. It was given a further anneal of more than 50 hours at 1200°C, encapsulated in an ultrahigh-purity argon back-filled quartz ampoule. The capsule was cracked open upon water quenching after the annealing treatment.

Samples of this alloy were spark-machined to shape, again about 25 mm x 1.5 mm x 1.5 mm, and then extensively electropolished, removing about 0.1 mm from each surface.

Several electropolishing solutions were employed in the course of the work, the best of which were:

1. 120 g chromic acid (CrO_3), 500 ml phosphoric acid, at 70°C, 7 volts.
2. 33 ml conc. nitric acid, 66 ml methanol, at 10°C, 57 volts open circuit, with 10 ohm load in series.
3. 25 ml sulfuric acid, 75 ml water, at 40°C, 6 volts.

The first of these solutions was found to be the best, although it was the last discovered. Additionally, when used at 2 volts, it acted as an excellent electro-etch for revealing grain boundaries and martensitic plates.

The polycrystalline samples of alloy 3 (Fe-31Ni-0.3C) and alloy 4 (Fe-31.3Ni) had been studied in a previous thesis and had been fully homogenized by hot deformation and annealing, so further heat treatment was only needed for austenitization and grain-size modification. These specimens took the form of rectangular strips about 40 mm x 5 mm x 0.5 mm.

All heat treatments during the course of this investigation were carried out with the sample thoroughly degreased, and the encapsulation material (vycor or quartz) chemically cleaned and baked out. The tubes were evacuated to approximately 10^{-6} Torr, flushed (at least twice) with ultrahigh-purity argon, and then back-filled to yield a pressure of one atmosphere within the capsule at the selected heat-treatment temperature.

Preliminary experiments showed that the heat treatment of the polycrystalline alloys had a very important effect upon their M_b temperatures. For alloy 4 the heat treatment cycle was as follows: A number of samples were austenitized at 1000°C for one hour followed by quenching into water without breaking the capsule in this case. Mechanical polishing via wet silicon carbide papers and 0.3 micron alumina produced a surface suitable for observation of surface relief effects resulting from subsequent transformation studies. The samples were then vycor re-encapsulated in batches and annealed at temperatures and times ranging from one hour at 1000°C to 25 hours at 1200°C in order to vary the grain size.

Grain-size measurements were conducted by counting grain boundary intersections with a microscope cross-hair while translating the specimen on a metallograph stage. The grain size is given here as the mean diameter:

$$G.S. = 1.65 \times (\text{distance translated/no. of intersections})$$

At least 300 and usually 500 intersections were counted.

After the grain-size anneal, the samples were removed from the unbroken capsule and subcooled to their transformation start-up temperature in the temperature-gradient device. The M_b temperatures obtained in this way were quite inconsistent.

The martensite-containing ends of the gradient specimens were spark-cut from the overall samples; since the gradient technique produced martensite at only one end of the sample over a small distance compared to its total length, most of the sample remained austenitic.

The remaining austenitic samples were then re-encapsulated into one ampoule and annealed at 800°C for one hour. Reacting the samples in a temperature gradient after this treatment produced consistent results. After thus reacting one end of the specimen, and then electropolishing the entire sample, the other end of the sample was also reacted in a temperature gradient. Results from both ends of the samples were reasonably consistent.

Alloy 3 was given a basically similar procedure to that for alloy 4 but still did not yield consistent findings. Accordingly, a different procedure was adopted. Three specimens which had previously received identical processing treatments were carried through an austenitizing treatment/electropolishing operation/subzero transformation for M_b measurement/grain-size determination cycle four times, increasing the austenitizing temperature (and thus increasing the grain size) each time, until the very last cycle when the initial cycle heat-treat temperature was repeated. The austenitizing temperatures were 950°C, 1050°C, and 1150°C. The gradient-specimen results from these experiments were satisfyingly consistent, and the M_b measurements thus made were then used to select data from the preliminary experiments which seemed to fall in the

appropriate range. Discussion of these effects takes place in Appendix III.

Thermal-Gradient Apparatus and Measurement Techniques

Production of a suitable thermal gradient in the various specimens was accomplished by two different techniques. One was used in the temperature range down to about -145°C , and the other in the range below -145°C to -196°C .

The first method consisted of two thin copper anvils which could be adjusted in separation distance to accommodate specimens of various lengths. These two anvils were soldered to brass chambers which, in turn, were connected either by copper tubing to a pressurized tank of liquid nitrogen which provided cold nitrogen vapor as a coolant, or by tygon tubing to a constant hydraulic-head supply of laboratory hot water (Figure 1). For good thermal contact, silver past obtained from Engelhard Industries, Inc., East Newark, N.J. was applied at the sample/anvil interfaces. Measurement of the thermal gradient was obtained with a series of four 0.075 mm diameter chromel-alumel thermocouples spark-welded to the sample. Since this spark-welding could produce a disturbed region, placement of the thermocouple to reach the lowest temperature was about 0.5 to 1.0 mm from the actual end of the sample, thus eliminating any effect upon the M_b . Placement of the remaining thermocouples was also carefully noted, and those samples where a thermocouple might have affected the data were specially recorded to check for any anomalies. However, this happened only rarely.

The thermocouple attachments were made directly to the sample, usually on opposite sides. Hence, the thermocouples were intrinsic in nature.

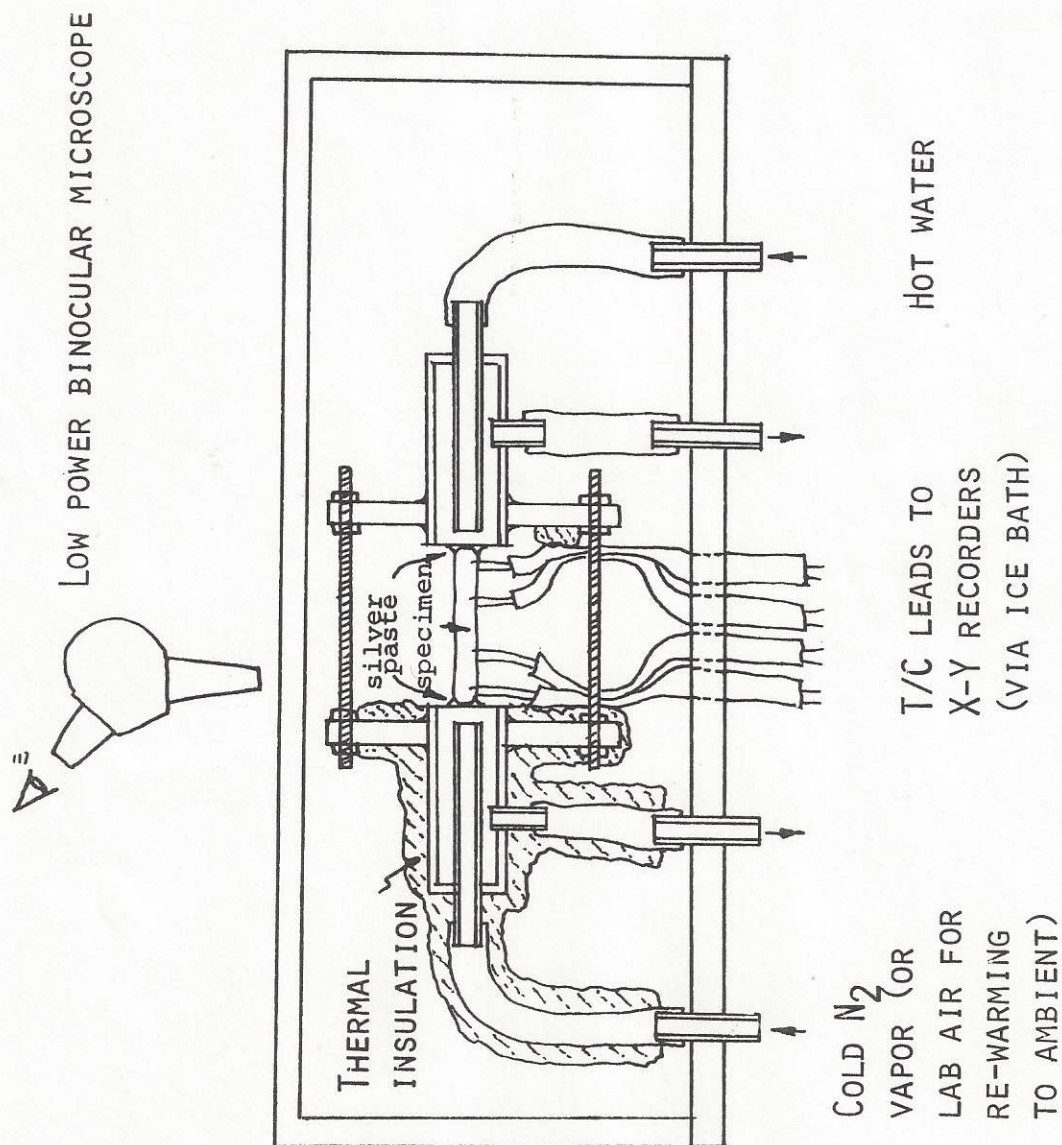


FIG. 1 TEMPERATURE GRADIENT DEVICE

Assuming that both leads in a pair were at the same temperature, no spurious effects upon their reading should be expected. Evidence of condensation fronts as the sample was cooled and re-warmed showed that the isotherms were, indeed, virtually perpendicular to the specimen axis. Condensation could not be completely suppressed, even though the entire sample holder was placed in an enclosed plexiglas box. In those cases where the thermocouple leads were not at exactly the same temperature according to the condensing front the thermocouple reading should correspond to an average temperature between the two leads. This temperature was then plotted at the average position of the thermocouple leads for determining the gradients. The positions of the leads were measured with a vernier microscope to 0.1 mm by noting the position of the crater left behind when the leads were removed from the sample after the run.

The thermocouple emf's were traced on two X-Y recorders, one a Hewlett-Packard model 7004 and the other a Moseley 2 DR-2, used with their most sensitive 0.5 mv/in settings. Readings were taken to the nearest 0.01 mv, though temperatures are only reported here to the nearest 0.5°C.

For the single-crystal specimens, measurements of the positions at which autocatalytic martensitic renucleation and plate growth stopped (later converted to temperatures) were made upon photographs which had been assembled into panoramic views of the microstructure. Serial-section metallography was adopted to ascertain the interior features which were not available otherwise. For obtaining the maximum propagation or plate-growth distance, the maximum distance measured from the end of the sample was chosen on whichever level it occurred in the serial sectioning. For the maximum distance of autocatalytic martensitic renucleation, a more

complicated procedure was necessary to ensure a conservative measurement. Assuming that renucleation takes place along the line of intersection between the initiating and autocatalytic plates, the actual location of the renucleation event is not metallographically discernable along this line. The conservative choice is to pick the lowest temperature point of the line of intersection. This was done in the highest temperature region of each sample where the number of plates becomes small. The maximum value obtained from these determinations was picked as the maximum distance of renucleation. This was probably the largest uncertainty in the data obtained.

Additionally, when plotting the temperature-distance profile of the sample from the thermocouple readings, except for the very shortest samples (about 1 cm), it was found that linear steady-state temperature conditions were not established for the cooling rates employed (about 2-5°C/min). Rather than try to fit a smooth curve through the four points obtained, three straight line segments were used instead. This should yield conservative (on the low side) temperature values, as the curve was concave downward. The error introduced by this procedure was never more than about 4°C and usually less, depending upon the distance from the nearest thermocouple.

For the polycrystalline samples, serial sectioning was not carried out, and measurements of the distance reached by autocatalysis were taken by etching the surface of the transformed sample (or in some cases by unetched surface relief).

Detection of the M_b temperature by the gradient method was not difficult in these bursting alloys except for the smallest grain sizes. Evidence of the burst occurrence was obtained in different ways. First, a low

power (27X) binocular microscope was used to monitor the surface of the samples; second, the thermocouple readings would "jump" during the burst, due to the release of the heat of transformation. This event caused the servo-controlled pen of the chart recorder to generate considerable noise. Thus, both visual and aural signals provided an indication of the martensitic reaction. When these signals occurred, a switch was thrown which closed a magnetically-operated valve to shut off the flow of coolant. This was followed by opening a valve allowing the room-temperature laboratory-air supply to warm the sample. At the same time, the pens for the chart recorders were raised, and the ends of the traces (both X and Y readings) marked the onset of the burst event.

The aforementioned second set-up was only used for the polycrystalline samples of alloy 3, which had a very low M_b . It consisted of a bar of copper which extended beneath a plexiglas case. The bar was notched to hold the sample in a vertical position in conjunction with a gravity-loaded sliding notched rod, which held the other end (Figure 2). Cooling was effected by lowering this entire assembly until the copper bar (projecting below) entered a dewar containing liquid nitrogen. The level of the liquid nitrogen with respect to the sample-containing end of the copper bar controlled the rate of cooling and the minimum temperature reached. Silver paste was again applied to insure good thermal contact between specimen and cooling bar. The sample was warmed back to room temperature by removing the holder from the liquid nitrogen dewar and immediately plunging it into a bath of water.

Temperature measurements were the same as in the previous set-up.

To verify that the M_b temperatures as observed were not influenced substantially by the gradient-cooling technique, a number of samples were

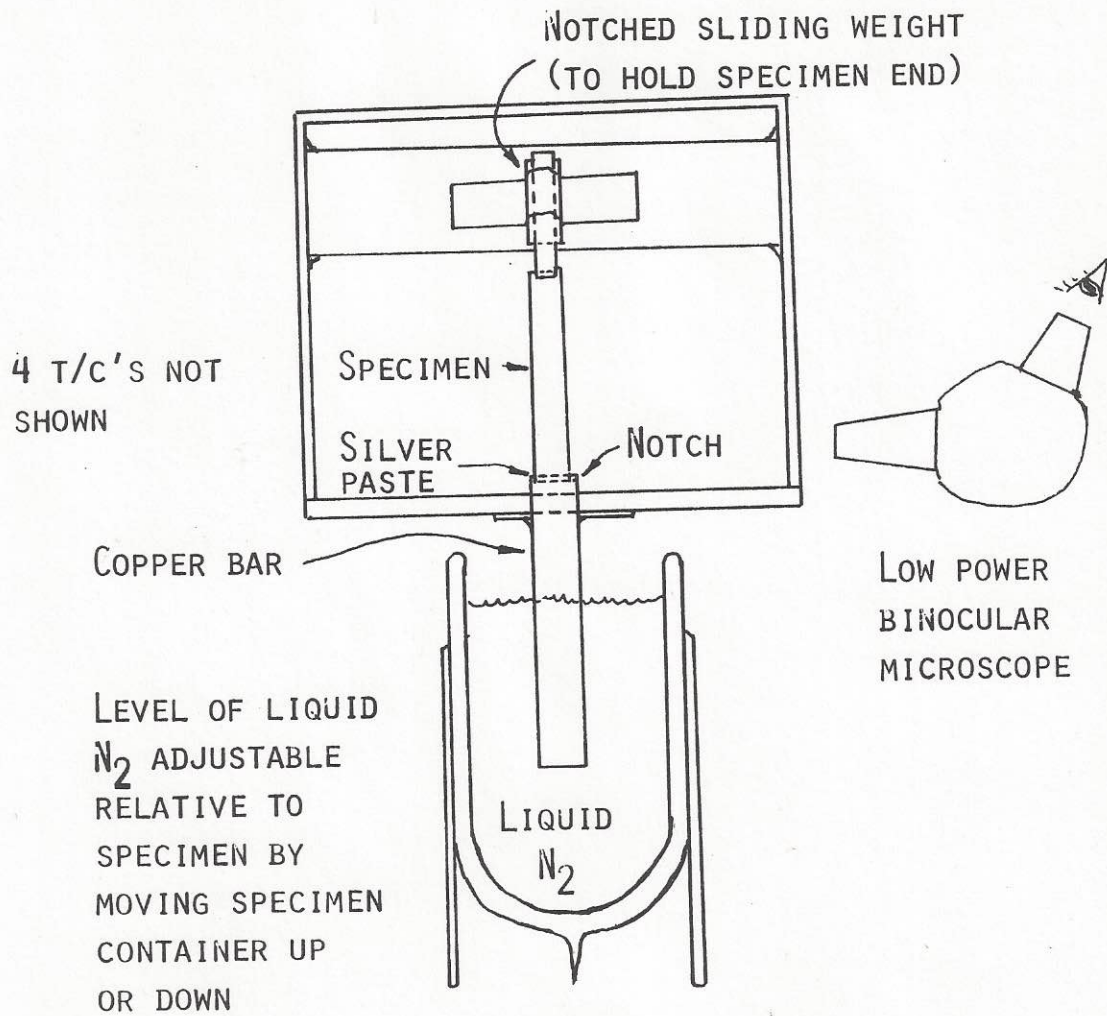


FIG. 2 VERY LOW M_B TEMPERATURE GRADIENT DEVICE

cooled uniformly in the chamber described in Figure 3. Dry laboratory air, cooled by flowing through copper tubing immersed in liquid nitrogen, was the coolant, and was allowed to impinge directly on the sample through an evenly staggered array of holes in the small diameter tubing within the cold chamber. In this case, spark welding the thermocouple directly to the sample was not needed. Normal thermocouples were attached at each end of the sample via silver paste. The sample was held lightly between two glass capillary tubes, which also served to separate the thermocouple leads.

Habit Plane Measurements

The necessary information for determining the habit planes of the various autocatalytic groupings of martensitic plates was obtained by an "effective" two-surface analysis. This means that successive parallel metallographic sections were photographed and the second-surface data deduced from the serial section information.

The first attempts involved mounting the sample in bakelite, and either using the specimen edge or a pin mounted in a hole drilled perpendicular to the mounting surface as a reference. Measurements of the thickness of the mount taken at several points around the rim yielded the amount of material removed.

It was decided, however, that multiple samples per mount would minimize the amount of polishing labor involved, so brass mounts with slots machined in them were made, which allowed holding as many as six samples in one mount. Also, the edges of the slots served as excellent reference marks. Samples were held in the slots with epoxy glue. However, a disadvantage of this technique was that the epoxy did not hold the samples

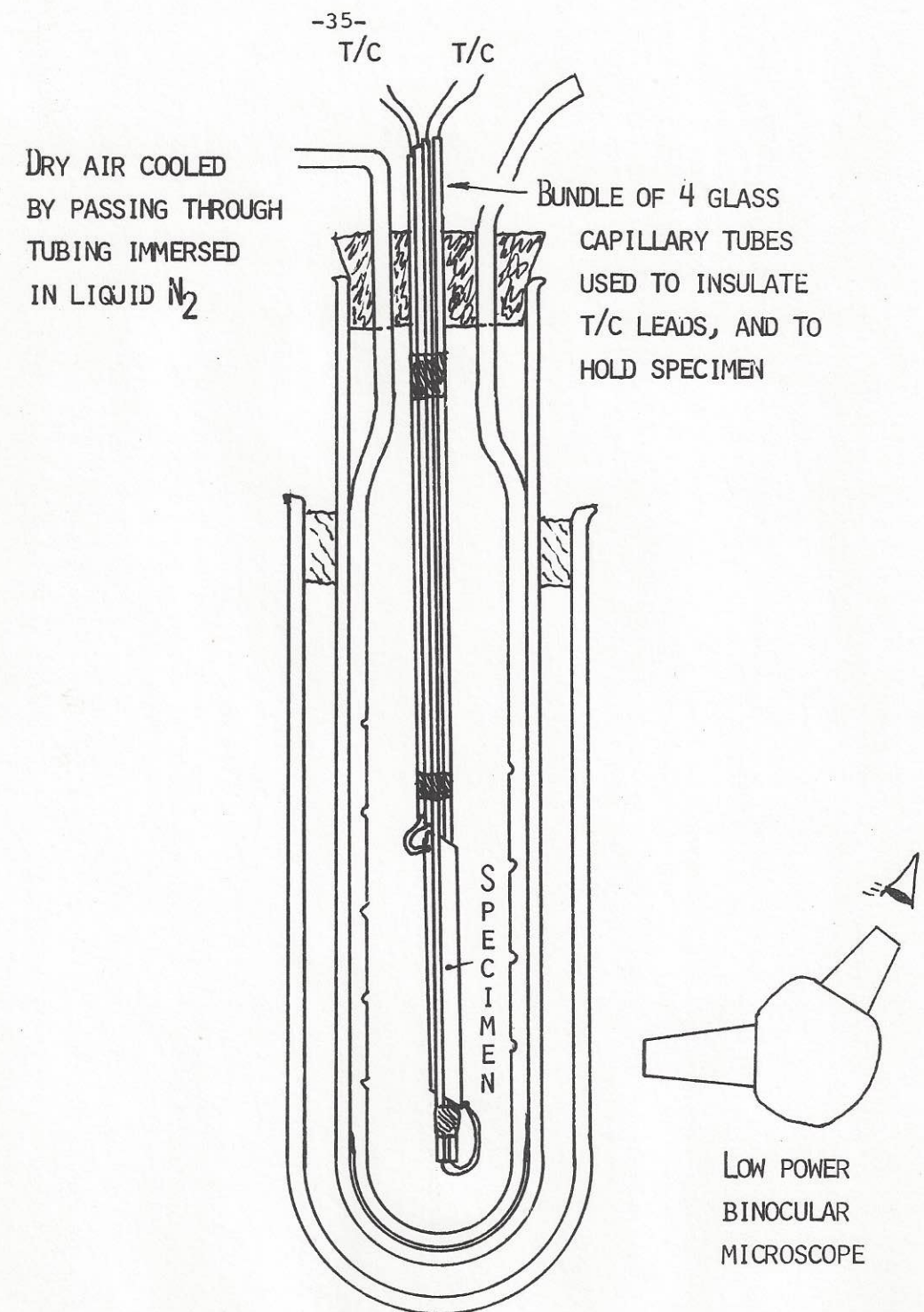


FIG. 3 DEVICE USED FOR UNIFORM COOLING

well enough to prevent them from coming out of the mount during mechanical polishing. A similar problem occurred with the bakelite mounts, though only after several levels had been removed. This difficulty was solved by spark cutting two bevelled notches into the sample, and by cutting a bevel on the end of the sample not containing martensite, which helped mechanical retention of the specimen and indicated if the sample was being retained properly in the mount. The latter circumstance was deduced by plotting the distance from a reference plane to the end of the notch versus the amount of material removed from the brass mount. Ideally, this should plot as a straight line. Any change in slope could be taken as an indication that breakaway from the mount had occurred. Thus, measurements taken beyond this point could be ignored or corrected, depending upon how late the discrepancy took place.

Polishing of the samples was carried out in the standard manner; silicon carbide papers, followed by 0.3 micron and 0.06 micron alumina powders. Returning to 240 grit paper between levels removed about 0.05 mm. Etching before photography was done with one of three etchants as follows:

1. 1% nital solution for about 30 seconds.
2. Modified Marble's reagent for 5 seconds, composed of 20 g copper sulfate, 100 ml conc. HCl, 100 ml H_2O , 200 ml ethanol.
3. Sodium bisulfate solution for 5 seconds, composed of 25 g sodium bisulfite, 100 ml H_2O .

The nital solution was excellent for the carbon-containing alloys, and the other two solutions were used interchangeably for the low-interstitial alloys.

Photography was carried out on either an AO or Leitz metallograph using either Kodak metallographic plates or Polaroid-type 55 P/N film. Measurements were usually taken directly from a positive print of the Polaroid. This yielded a result quickly, and by a relatively dry process, so that paper shrinkage did not influence the measurements or decrease the accuracy with which the panoramas could be assembled. This feature was important because in some cases extrapolation from one photo to the next was necessary before the trace of a plate intersected a reference mark.

The technique of determining the habit orientation (Figure 4) involved first drawing a line through the center of the plate in question (its midrib if possible). Measuring its angle with reference to a fixed direction (either the slot edge or the sample edge) yielded intersection points on a given great circle (that parallel to the polished surface). Next, measurement was made of the distance from a reference point on a reference line and the intersection of the trace of the plate of interest with the reference line. This distance was recorded for the same plate on several sectioning levels and then plotted on graph paper as a function of the amount of material removed. A line drawn through these points was then the intersection of the plate being measured with a second "surface." An angle could then be measured in this plane, yielding the intersection points of the plate with a second great circle. Given the intersections with two great circles allows determination of the habit plane, as in Figure 4, once the austenite orientation is known.

A standard Laue back-reflection X-ray photograph was taken to determine the orientation of the austenite. This orientation pattern was obtained with the X-ray spot in the austenite just ahead of the furthest

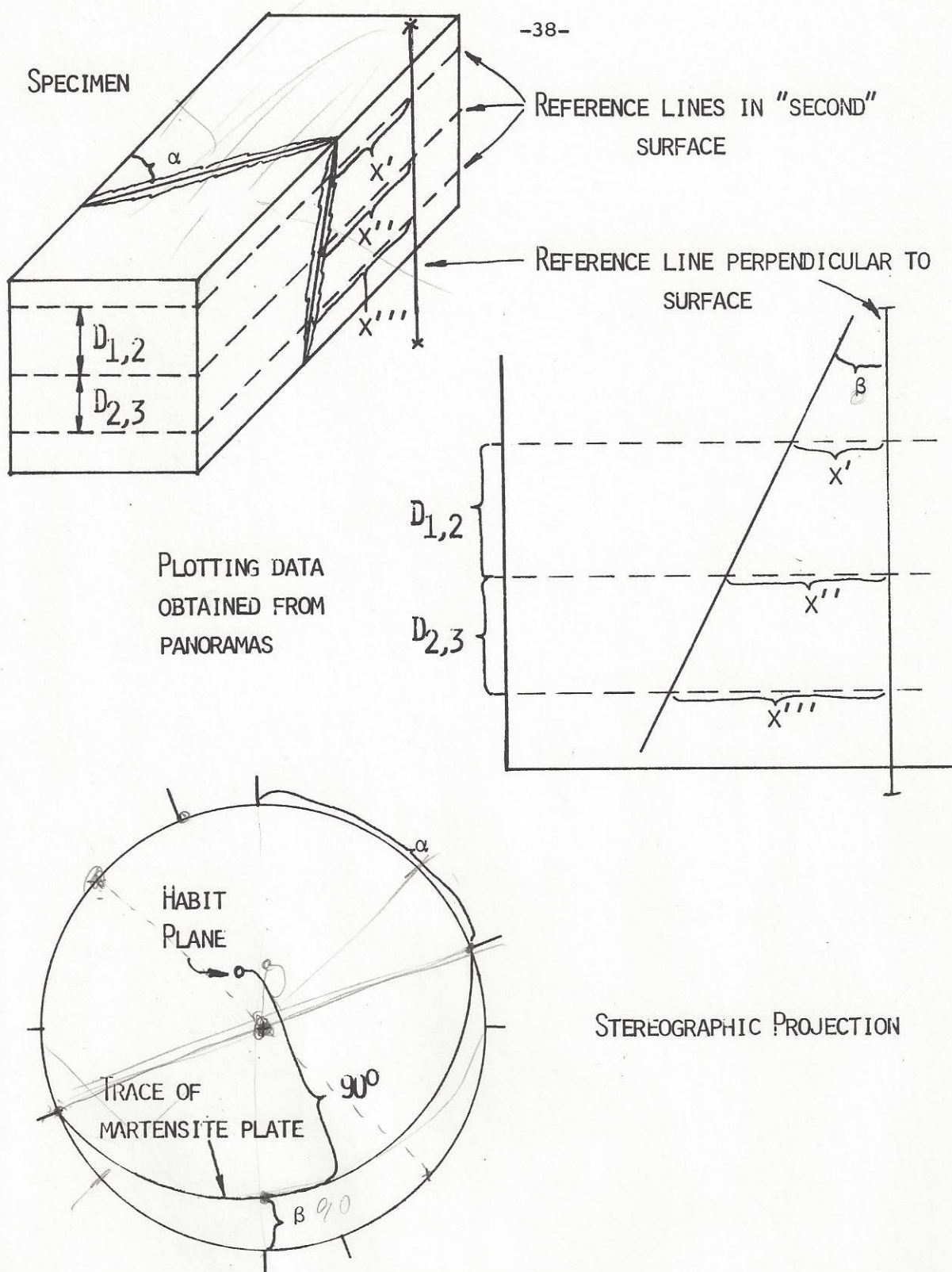


FIG. 4 HABIT PLANE DETERMINATION TECHNIQUE

martensitic plates along the gradient, after the sample had been mounted and polished a number of times. The accuracy of these habit determinations was adequate to locate the habit plane within a unit triangle, but was not sufficient to fix the habit indices with any certainty. Nevertheless, the habit planes thus obtained seemed consistent with reported determinations on similar alloys, being near $(3\ 10\ 15)_{\text{fcc}}$.

Preparation of Concentration-Gradient Specimens

Specimens containing a composition gradient, necessary for the complementary experiments in which temperature and composition exchange roles, were prepared by multiple-pass zone refining of an alloy containing nominally 35 w/o Ni. Four passes were made with an MRC electron-beam zone refiner under a vacuum of 10^{-6} Torr.

Small rectangular bars 0.8 mm x 1.5 x 20 mm were spark cut from the appropriate region of the sample, chemically polished lightly in an 80 ml conc. H_3PO_4 -20 ml H_2O_2 (30% solution) mixture in order to remove the thin copper layer resulting from the spark cutting, and homogenize-annealed in a quartz tube at a temperature of 1200°C for 24 hours to eliminate micro-segregation. A foil of tungsten was inserted as a barrier between the samples and the quartz. After this annealing, final spark cutting was done to ensure that the ends of the specimens would correspond to a 1 mm difference in position along the axis of the composition gradient. Six specimens were obtained from four pieces originally treated. Before transformation, the specimens were electropolished to provide a smooth surface for observation.

Transformation of Composition-Gradient Samples

Uniform cooling of these specimens was carried out by mounting each sample on a brass block (with silver paste) containing internal passages through which cold nitrogen vapor could be passed. The sample was protected from condensation by a plexiglas cover. Additional internal passages in the block could be flooded with hot water to warm the sample immediately upon the first detection of martensite.

The burst was disclosed by the presence of surface relief observed through a low power (56X) binocular microscope. A thermocouple was spark-welded to the sample (away from the low Ni-concentration end) to monitor its temperature.

Analysis of Composition Gradients

The reacted samples were mounted in bakelite and analyzed in an ARL microprobe using a technique of concentration determination suggested by Ogilvie and Ziebold.⁽⁵⁵⁾ Data were taken at 30 kV with a specimen current of 0.030×10^{-6} Amp. Pure standards of Fe and Ni were included in the specimen mount.

Before fixed-point counting, continuous scans were made across each specimen with the counting rate for Ni radiation displayed on a chart recorder. The resulting profiles were then used to decide upon the locations for fixed-point counting. Counting times were at least 50 seconds at each location chosen.

Compositions were obtained from the raw data via the equation

$$\frac{1 - K_a}{K_a} = A_{ab} \times \frac{1 - C_a}{C_a}$$

where $K_a = \frac{\text{Element "a" specimen intensity}}{\text{Element "a" pure standard intensity}}$

and where a background correction was subtracted from the raw intensities measured. A_{ab} is a calibration curve constant. For the Fe-Ni system @ 30 kV and with a take-off angle of 52.5° (appropriate for the ARL probe), this constant has been determined as 1.158 for Ni radiation and 0.847 for Fe radiation. C_a is the atomic fraction of element "a."

Intensities of the standards were taken both before and after analysis of the specimens. Compositions were determined independently for both Fe and Ni. Addition of the two should yield 100% ideally, with any discrepancy indicating the relative accuracy of the determination. The accuracy in this method was usually much better than $\pm 2\%$ relative to the amount present. For example, at 35% Ni this would indicate an error bar of less than $\pm 0.7\%$.

After the probe work was done, the sample was etched lightly (to bring out the trace along which the electron beam had travelled) and photographed. Measurements of the maximum Ni content to which martensitic growth had occurred were taken near where the electron beam trace had passed, and measurements of the maximum Ni content at which autocatalytic renucleation had occurred took into account a previous serial section to help choose conservative values (as discussed earlier in connection with the temperature-gradient experiments).

CHAPTER IV

EXPERIMENTAL RESULTS

Results from the experimental program followed in this work can be grouped into two broad categories. The first, on thermodynamic driving forces, encompasses data derived from single and polycrystalline temperature-gradient samples as well as single-crystal composition-gradient samples. The second, concerning autocatalytic-plate spatial groupings, stems from the serial section metallography performed on the single-crystal temperature-gradient specimens.

In both categories there are subgroups corresponding to each alloy studied, and in the first category there is an additional division between single and polycrystalline results.

Thermodynamic Data

Results of the single-crystalline temperature-gradient experiments are presented as distances and temperatures in Table 2. d^{rn} and T_{max}^{rn} refer to the maximum distance (from the sample cold end) and temperature of renucleation, and d^{gr} and T_{max}^{gr} refer to the maximum distance (from the sampled cold end) and temperature of growth. Temperatures are converted to driving forces (see the last section of this chapter) and listed in Table 3. The autocatalytic assist, calculated from:

$\Delta G^{\gamma \rightarrow \alpha'}(T_{max}^{rn}) - \Delta G^{\gamma \rightarrow \alpha'}(M_b) = \delta \Delta G$, will be compared with the energetic predictions of the various autocatalytic models on pages 74-87 and discussion of the minimum driving force for growth will take place on pages 116-122.

The temperature differences $T_{max}^{rn} - M_b = \Delta T$ achieved in the polycrystalline temperature-gradient samples are presented in Figure 5 and Figure 6

Table 2

Compilation of single-crystal temperature-
gradient data obtained from metallographic
panoramas

Specimen	M_b ($^{\circ}\text{C}$)	d^{rn} (mm)	$T_{\text{max}}^{\text{rn}}$ ($^{\circ}\text{C}$)	d^{gr} (mm)	$T_{\text{max}}^{\text{gr}}$ ($^{\circ}\text{C}$)
Alloy 1					
X2	-78	7.0	-24.5	11.9	-1
G	-43	4.4	-18	5.1*	-1.5*
E	-56	10.9	-12.5	14.4	1
S	-82	6.6	-15	9.0	6
N	-90	12.5	-11	15.6	-3
A2	-70	10.4	-17	13.5	-4
C	-86	9.0	-23	14.9	7
M27	-60	9.1	-15	12.4	-3
A3	-77	8.0	-26	11.4*	-10*
1-75	-72	6.2	-27	10.8	-9
average:	-77**		-19		-1
standard deviation:	9.5		5.8		5.0
Alloy 2					
Y1	-63	8.6	-8	10.0	-0.5
F	-49.5	9.1	-2.5	10.5*	2.5*
H	-42.5	8.8	-5.5	10.0	-1.5
D	-56	12.2	-1	13.4	3
Y2	-51.5	5.5	-18	6.4*	-12.5*
X1	-61	8.2	-12	12.9	10
average:	-54		-8		3
standard deviation:	7.6		6.4		4.5

* Indicates that last plate ran off side of specimen and thus should be higher.

** Ignores M_b for specimens G & E.

Table 3

Chemical driving-force values (cal/mole)							
Specimen	M_b	$\Delta G_{\gamma \rightarrow \alpha'}(M_b)$	T_{max}^{rn}	$\Delta G_{\gamma \rightarrow \alpha'}(T_{max}^{rn})$	T_{max}^{gr}	$\Delta G_{\gamma \rightarrow \alpha'}(T_{max}^{gr})$	$\delta \Delta G$
SINGLE CRYSTALS							
<u>Alloy 1</u>	196°K	-308	254°K	-247	272°K	-226	61
<u>Alloy 2</u>	219	-286	265	-231	276	-218	55
POLYCRYSTALS							
<u>Alloy 3</u>							
small grain size	111	-210	131	-202			8
large grain size	111	-210	186	-166			44
<u>Alloy 4</u>							
small grain size	198	-294	211	-281			13
large grain size	198	-294	229	-261			33

Temperatures used for single crystal results are averages from Table 2. Temperatures used for polycrystalline results (except for M_b , which is a multi-specimen average) are taken off the data envelope vs grain size at the data limits.

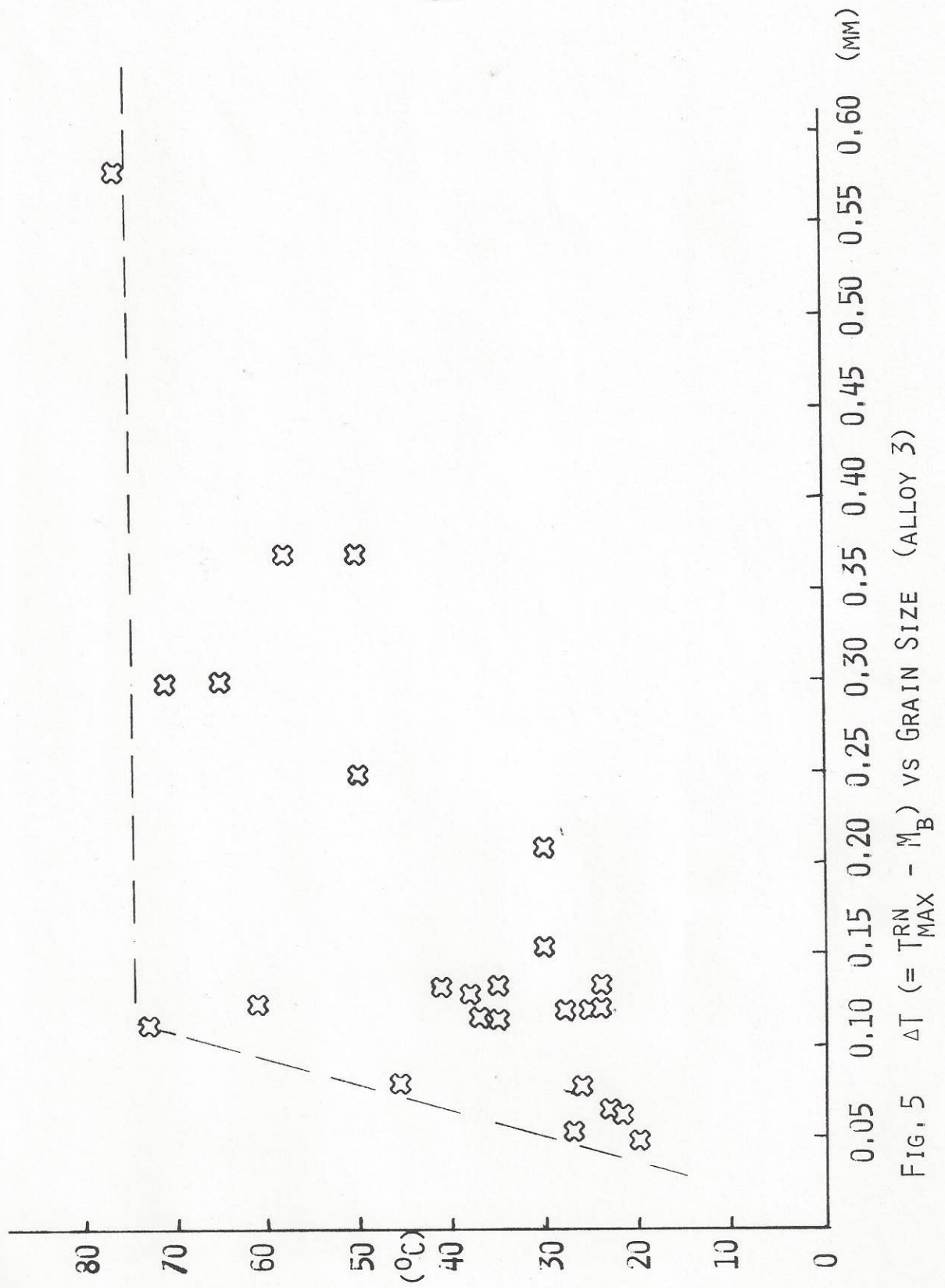


FIG. 5 $\Delta T (= T_{\text{RN}} - M_B)$ VS GRAIN SIZE (ALLOY 3)

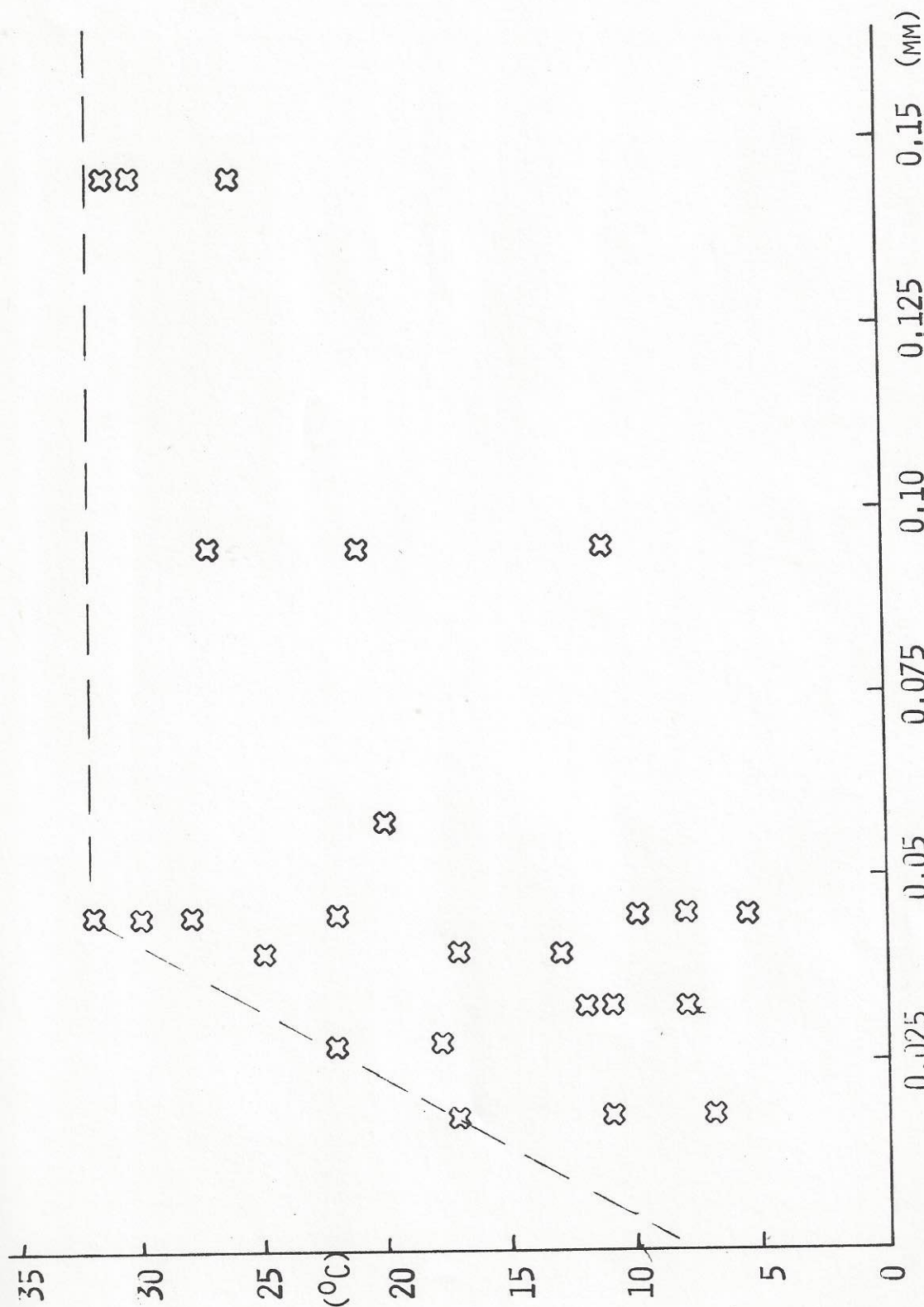


FIG. 6 $\Delta T (=T_{MAX}^{RN} - M_B)$ VS GRAIN SIZE (ALLOY 4)

for alloys 3 and 4 respectively. Representative values are converted to driving forces and shown in Table 3. Discussion of these values and their implications about the mechanism of autocatalysis across grain boundaries takes place on pages 111-116.

Results from the composition-gradient experiments are presented in Table 4. C_{M_b} refers to the composition at which the reaction was triggered. d^{rn} and d^{gr} refer to the distances from the low-Ni end of the specimen to which renucleation and growth (respectively) proceeded. C_{max}^{rn} and C_{max}^{gr} refer to the compositions at those distances. Calculation of the driving forces will be presented on pages 106-11 after discussion of modifications to the composition data that have to be introduced. After incorporating these modifications, temperature and composition dependencies of $\delta\Delta G$ and $\Delta G^{\gamma \rightarrow \alpha'}(T_{max}^{gr})$ are also discussed on pages 106-11.

Metallographic Data

Selected serial-section metallographic panoramas are presented for representative samples of each single crystalline alloy in Figures 7, 9, 11, 13, 15, 17, 19 and 21. Following each page of panoramas is a stereographic projection which indicates the analyzed habit planes of the variants noted (Figures 8, 10, 12, 14, 16, 18, 20 and 22). The habits contained within the characteristic autocatalytic motifs will be used to check predictions of the various models. Discussion of these models and their predictions takes place on pages 74-87 & 88-100 of the next chapter.

Panoramas of the composition gradient specimens are presented in Fig 23.

The curvature of Specimen E, and the notches at the cold end of Specimen Z2 are due to an unsuccessful attempt to further simplify the morphology.

Table 4

Compilation of composition-gradient data obtained
from metallographic panoramas and microprobe results.

M_b	$C_{M_b}^{(w/oNi)}$	$d^{rn}(mm)$	$C_{max}^{rn}(\%Ni)$	$d^{gr}(mm)$	$C_{max}^{gr}(w/oNi)$
257°K	29.1**	2.45	30.7	3.35	31.5*
242	29.8	2.15	31.5	2.80	34.8
223	29.4	1.60	31.5	1.65	32.4
134	31.5***	1.15	34.5	1.35	35.1

* Ran off end of specimen, should be higher.

** Measured at end of lath-martensite region. The lath martensite was present prior to subcooling.

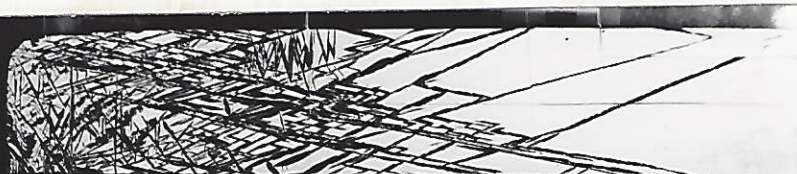
*** Measured on adjacent specimen.

PAN
No.

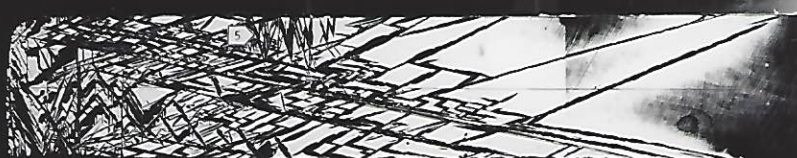
-49-

AMOUNT
REMOVED
(MM)

8



9



10



11



12



13



14



15



0.05

0.07

0.11

0.06

0.05

0.06

0.05

FIG. 7 METALLOGRAPHIC PANORAMAS OF SPECIMEN 1 (ALLOY 1)
(15.3 X)

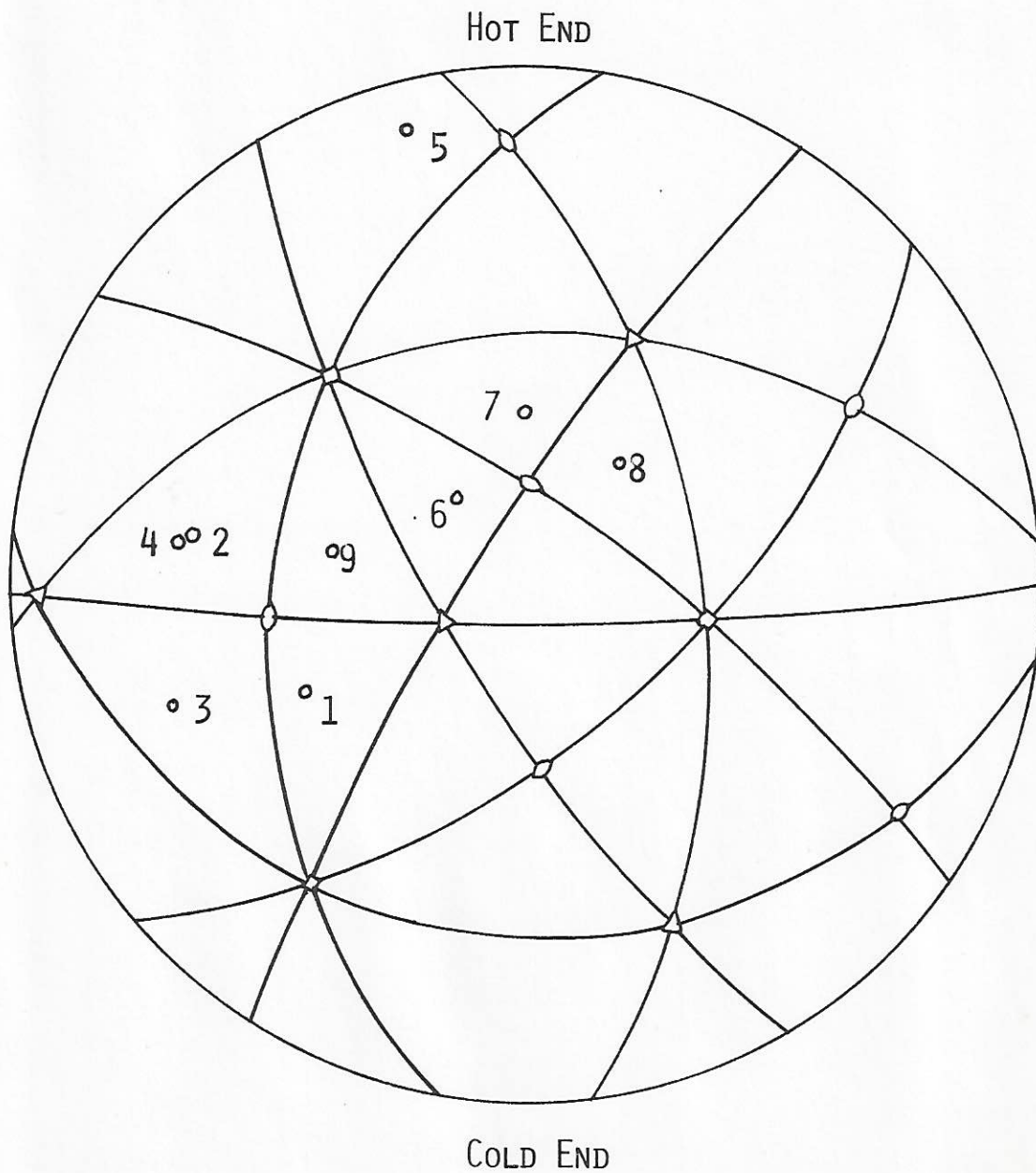


FIG. 8. RESULTS OF METALLOGRAPHIC HABIT PLANE
ANALYSIS OF SPECIMEN 1 (ALLOY 1)

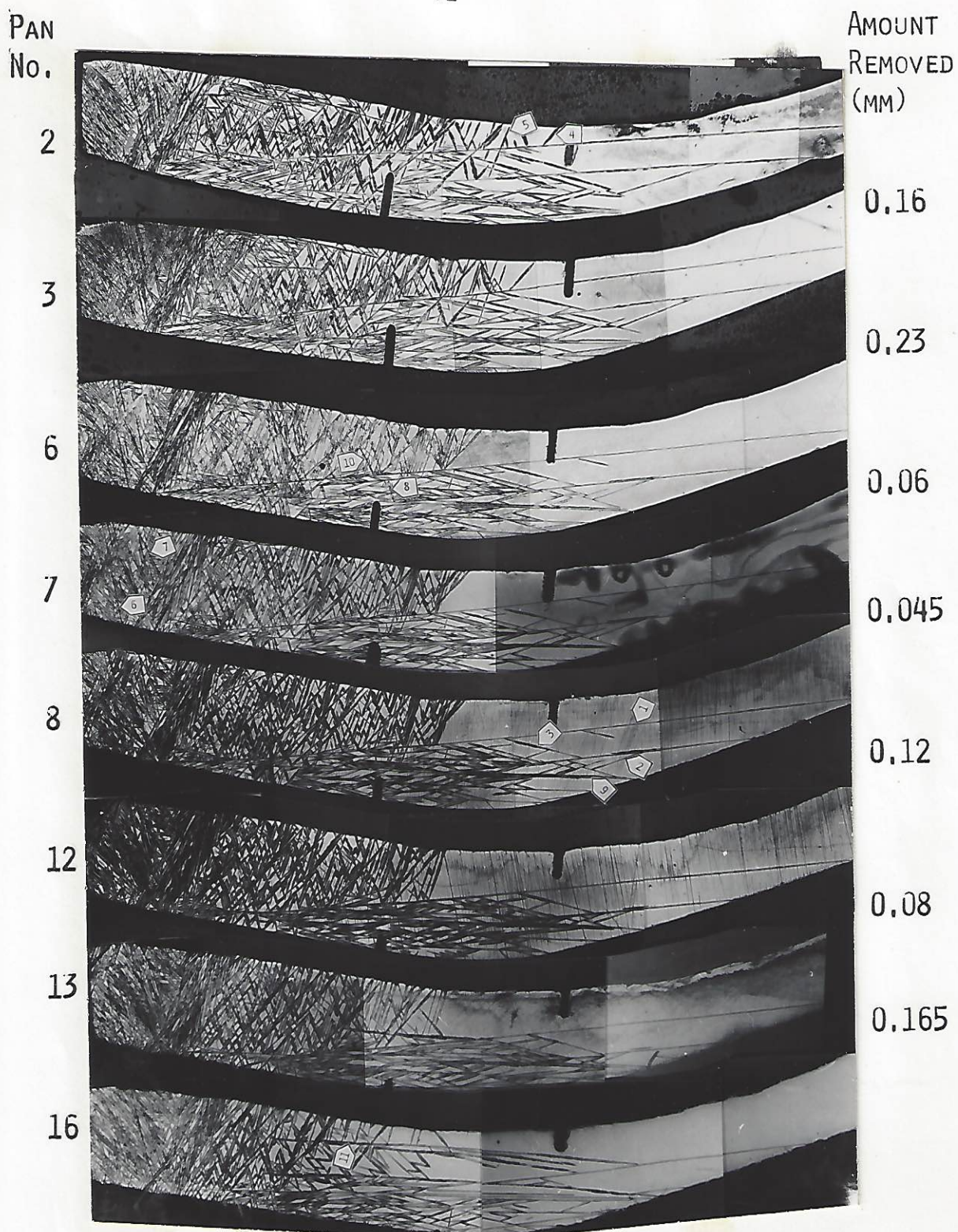


FIG. 9 METALLOGRAPHIC PANORAMAS OF SPECIMEN E
(ALLOY 1) (8.6 X)

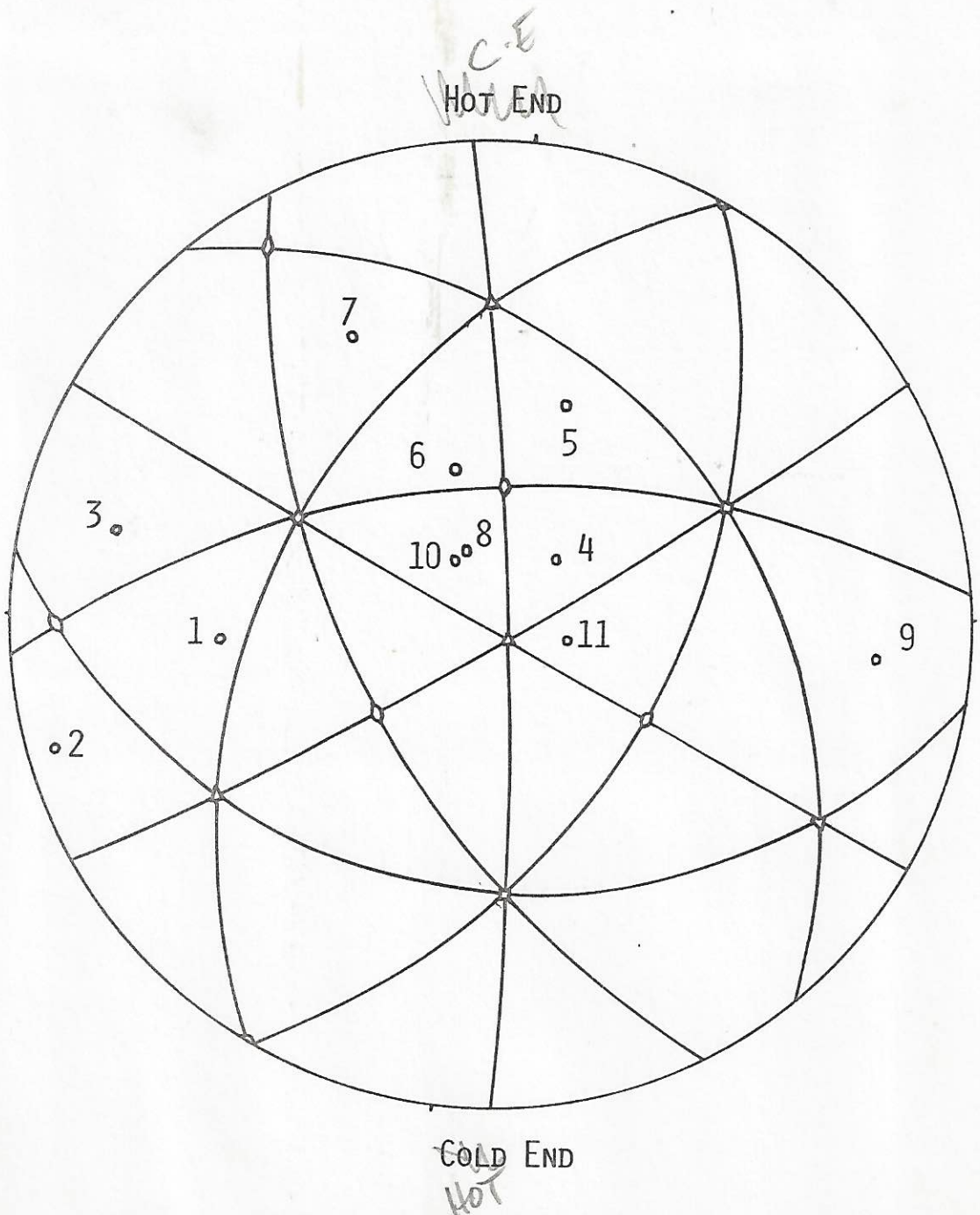
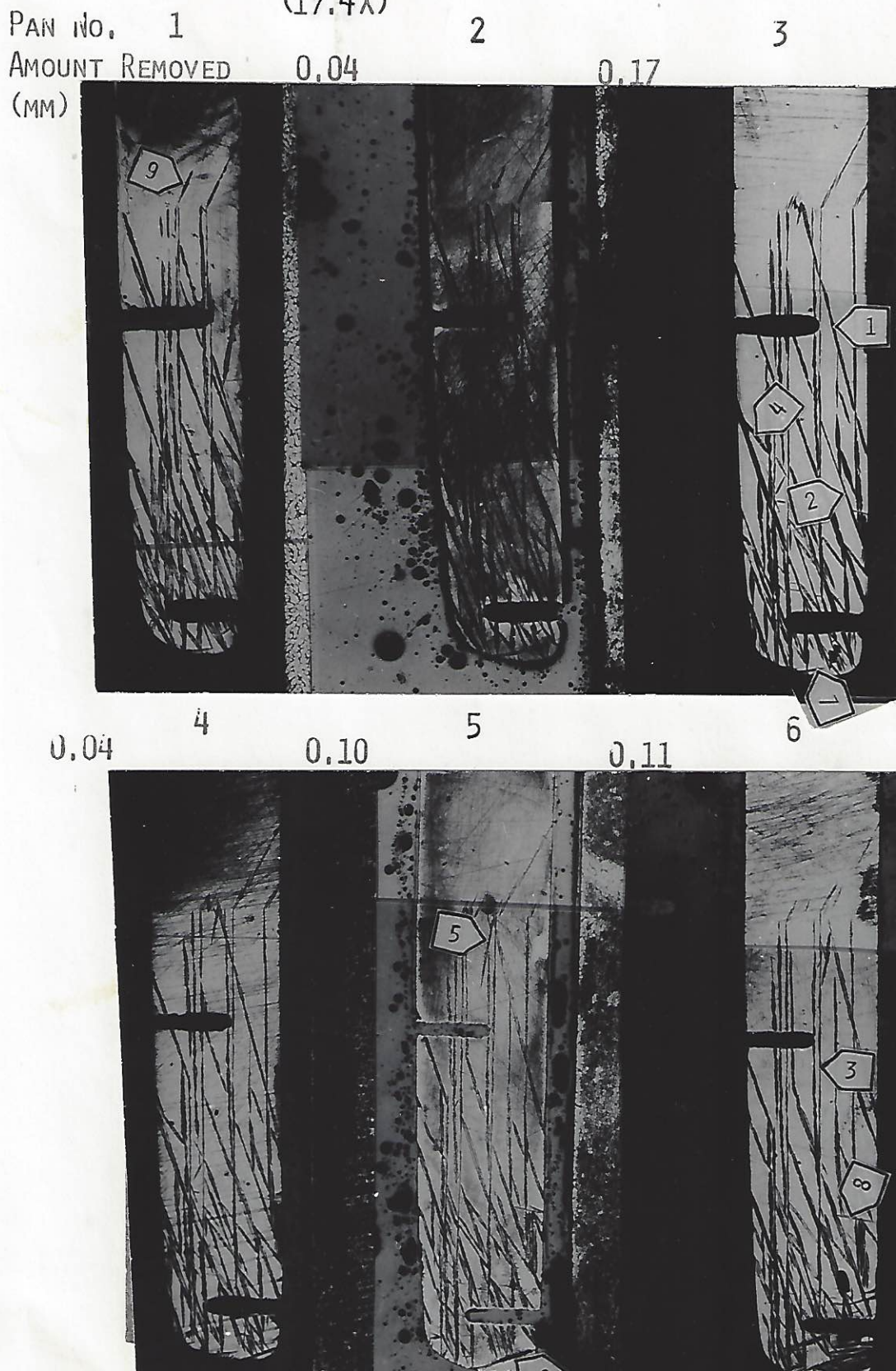


FIG. 10 RESULTS OF METALLOGRAPHIC HABIT PLANE
ANALYSIS OF SPECIMEN E (ALLOY 1)

FIG. 11 METALLOGRAPHIC PANORAMAS OF SPECIMEN G (ALLOY 1)
(17.4X)



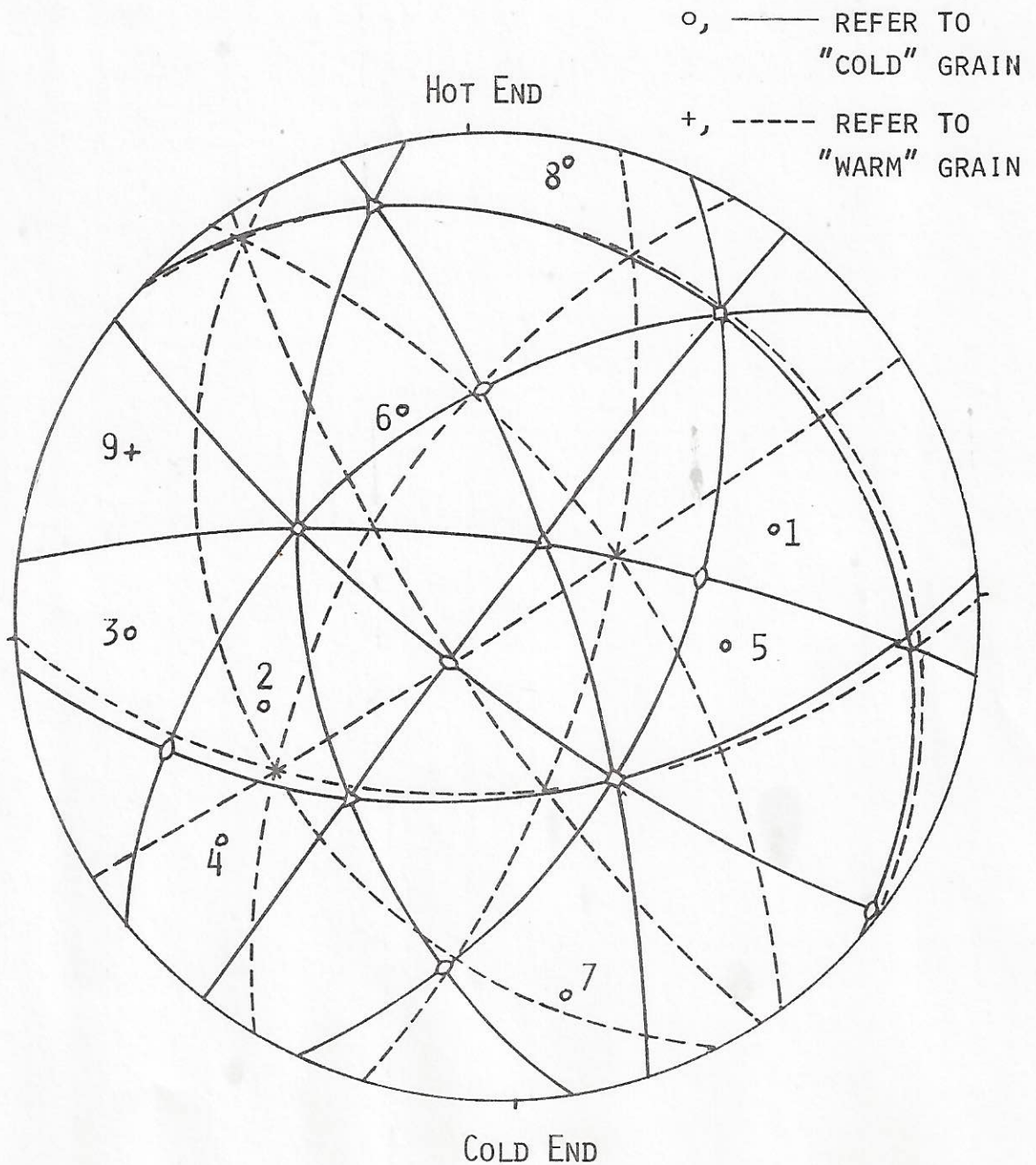


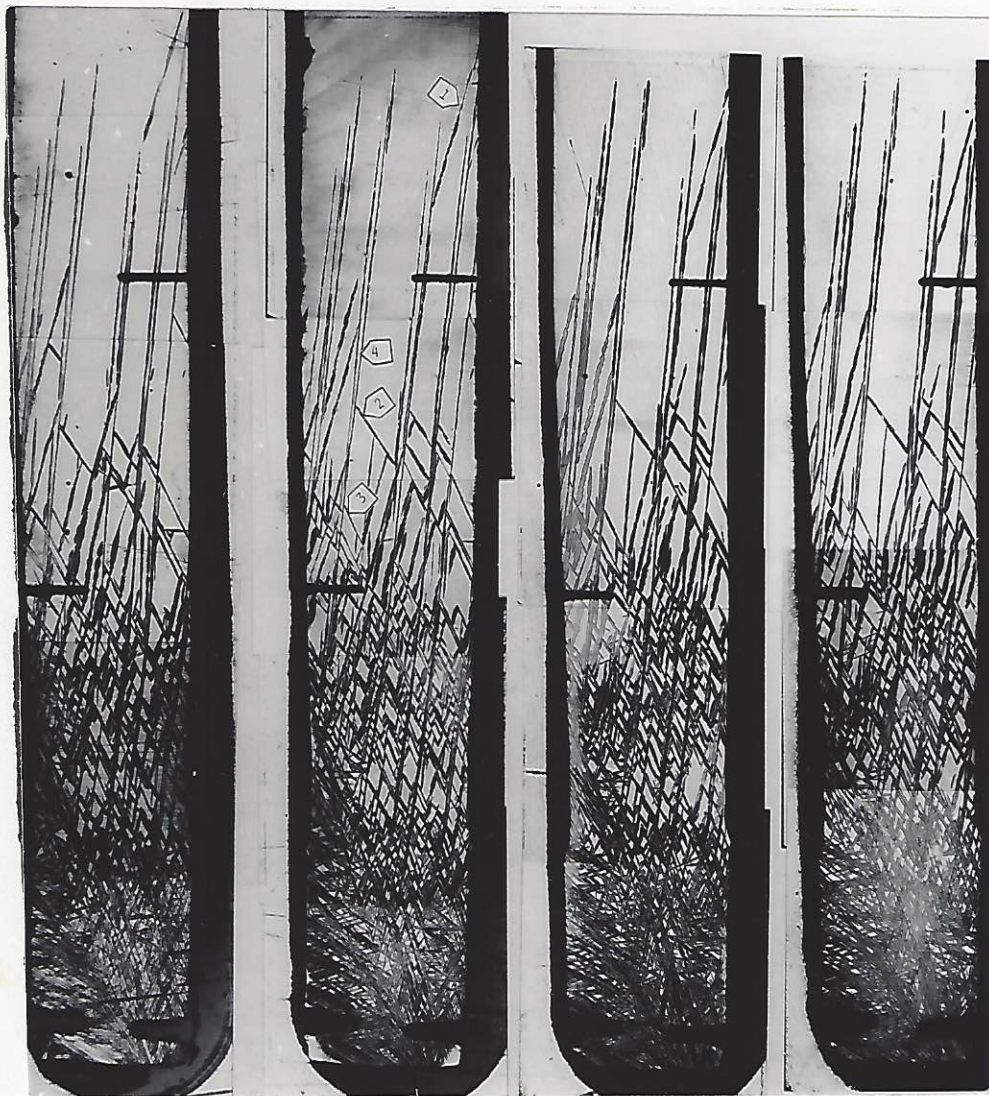
FIG. 12 RESULTS OF METALLOGRAPHIC HABIT PLANE
ANALYSIS OF SPECIMEN G (ALLOY 1)

AMOUNT
REMOVED
(MM)

0.11

0.06

0.02



PAN
No.

1

3

5

6

FIG. 13 METALLOGRAPHIC PANORAMAS OF SPECIMEN Z2
(ALLOY 1) (8.7 X)

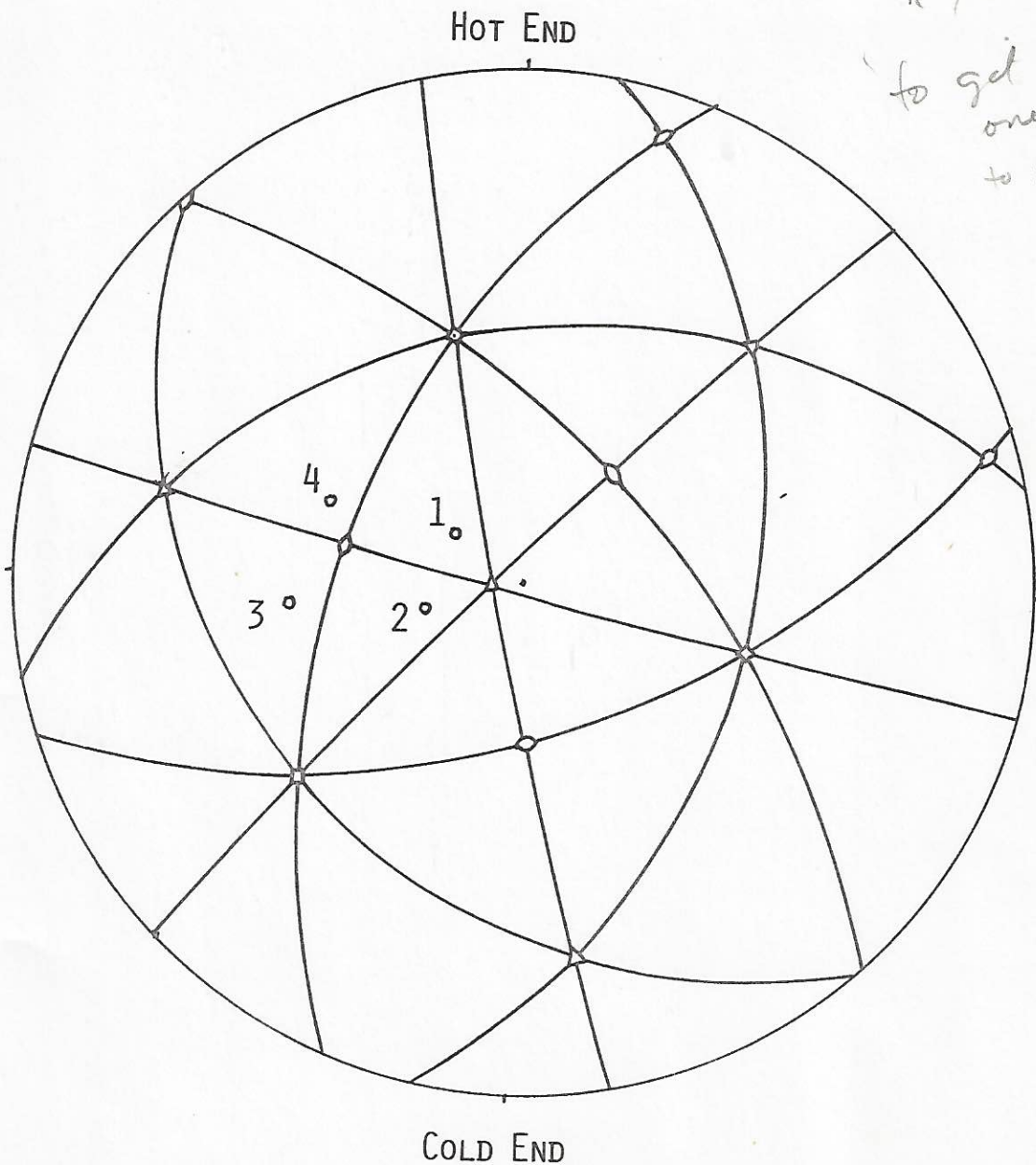


FIG. 14 RESULTS OF METALLOGRAPHIC HABIT PLANE
ANALYSIS OF SPECIMEN Z2 (ALLOY 1)



0.045	0.16	0.04	0.105	0.10	0.07	AMOUNT REMOVED (MM)
FIG. 15 METALLOGRAPHIC PANORAMAS OF SPECIMEN F (ALLOY 2) (12.2X)						

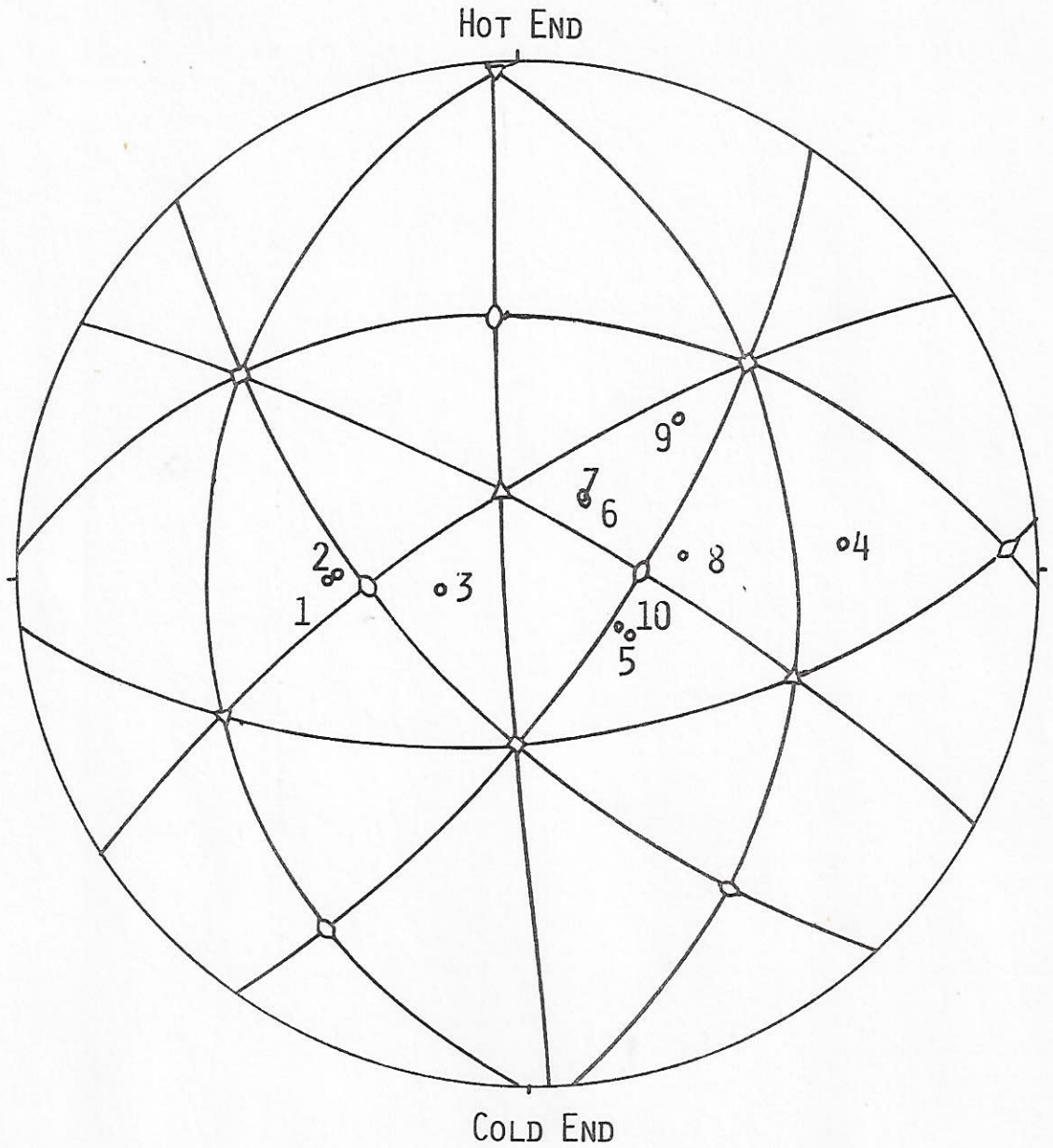


FIG. 16 RESULTS OF METALLOGRAPHIC HABIT PLANE ANALYSIS OF SPECIMEN F (ALLOY 2)

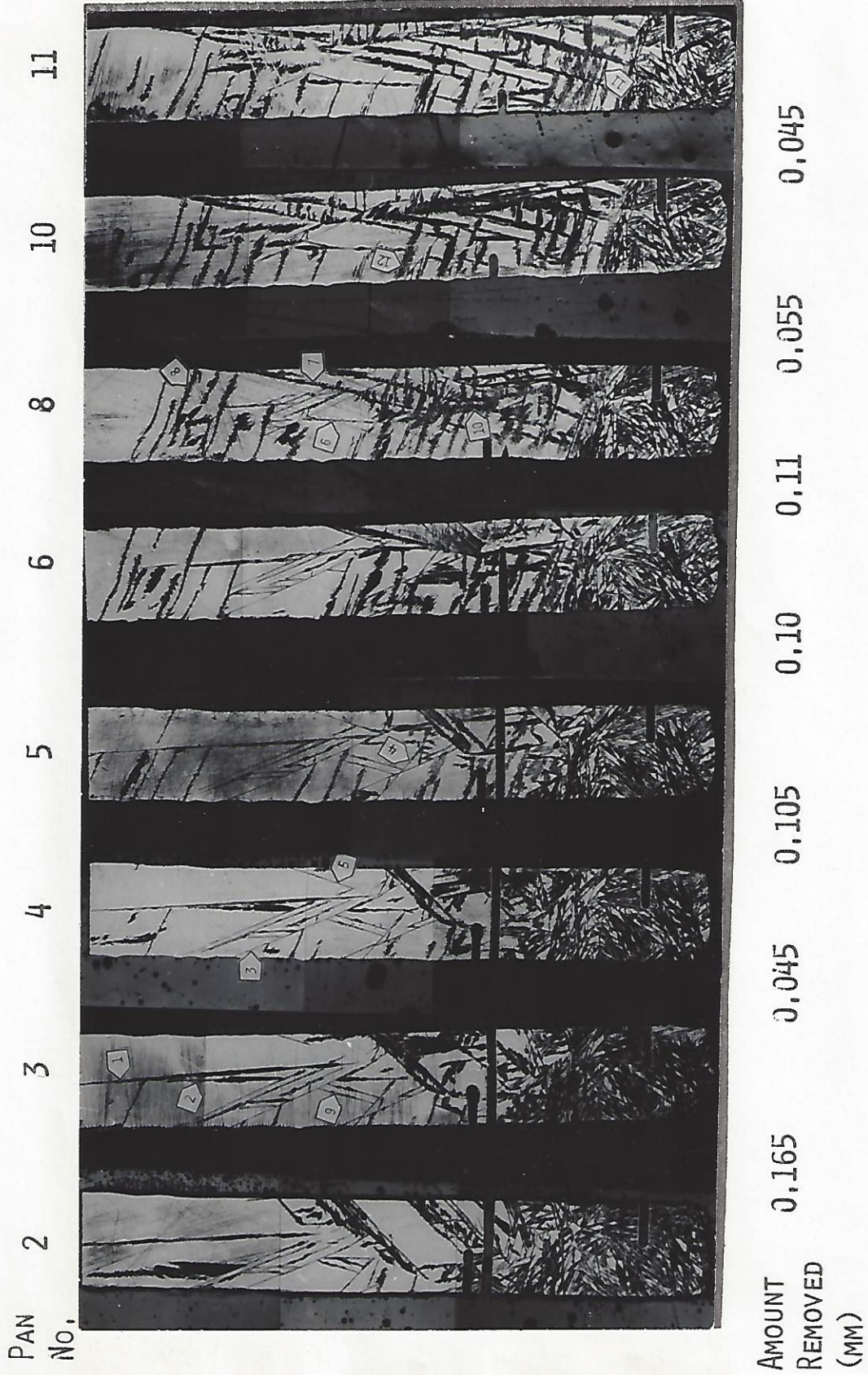


FIG. 17 METALLOGRAPHIC PANORAMAS OF SPECIMEN H (ALLOY 2) (10.7X)

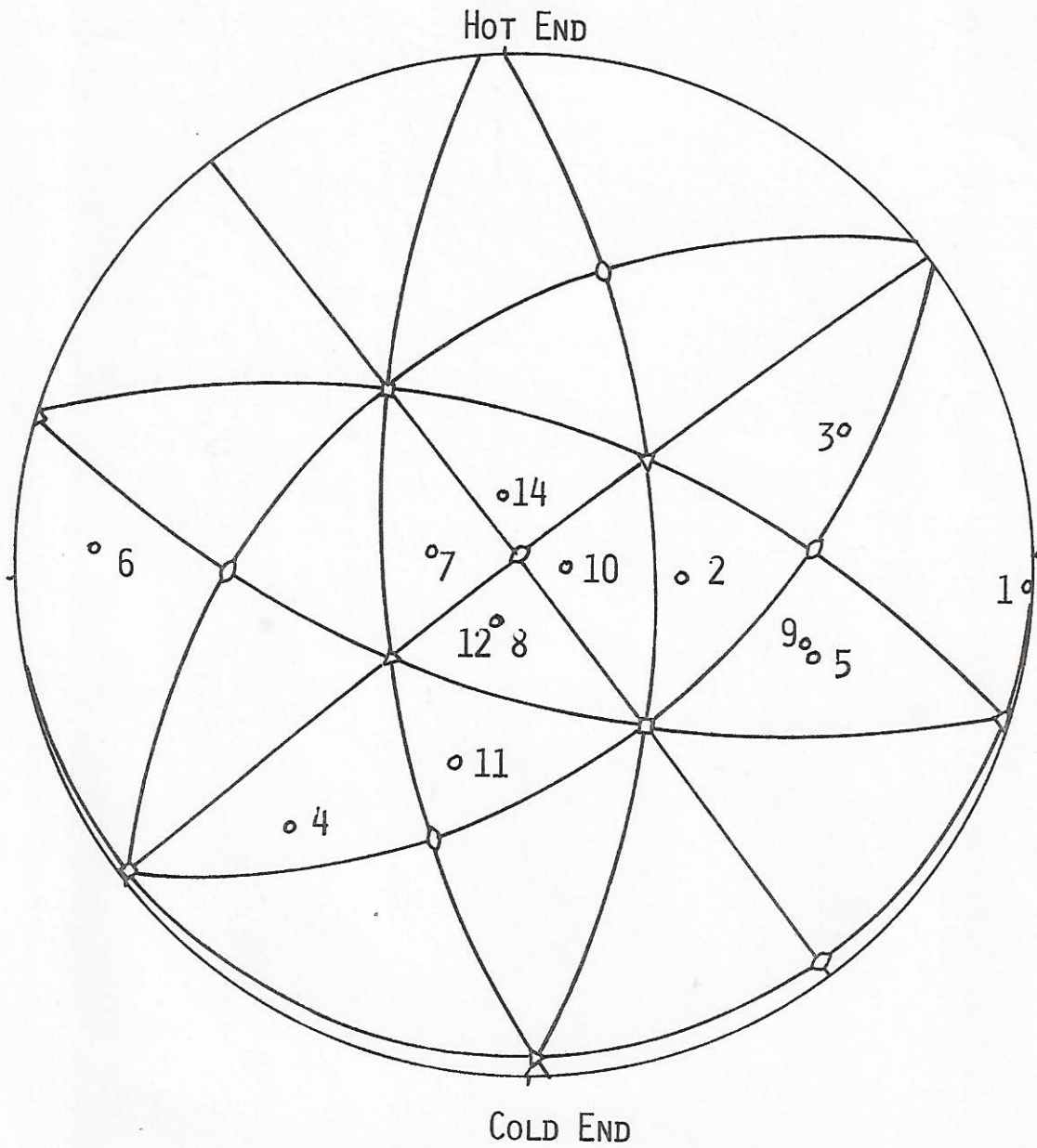


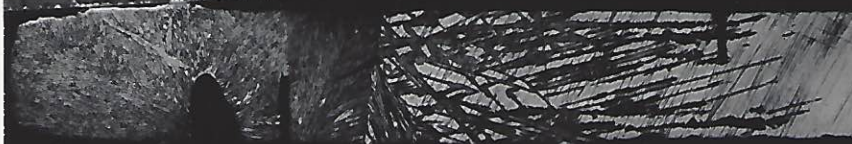






FIG. 18 RESULTS OF METALLOGRAPHIC HABIT PLANE ANALYSIS OF SPECIMEN H (ALLOY 2)

FIG. 19 METALLOGRAPHIC PANORAMAS OF SPECIMEN X1 (ALLOY 2)
(9.5X)

PAN No.		AMOUNT REMOVED (MM)
2		0.09
4		0.13
8		0.07
10		0.05
12		0.05
14		0.045
16		

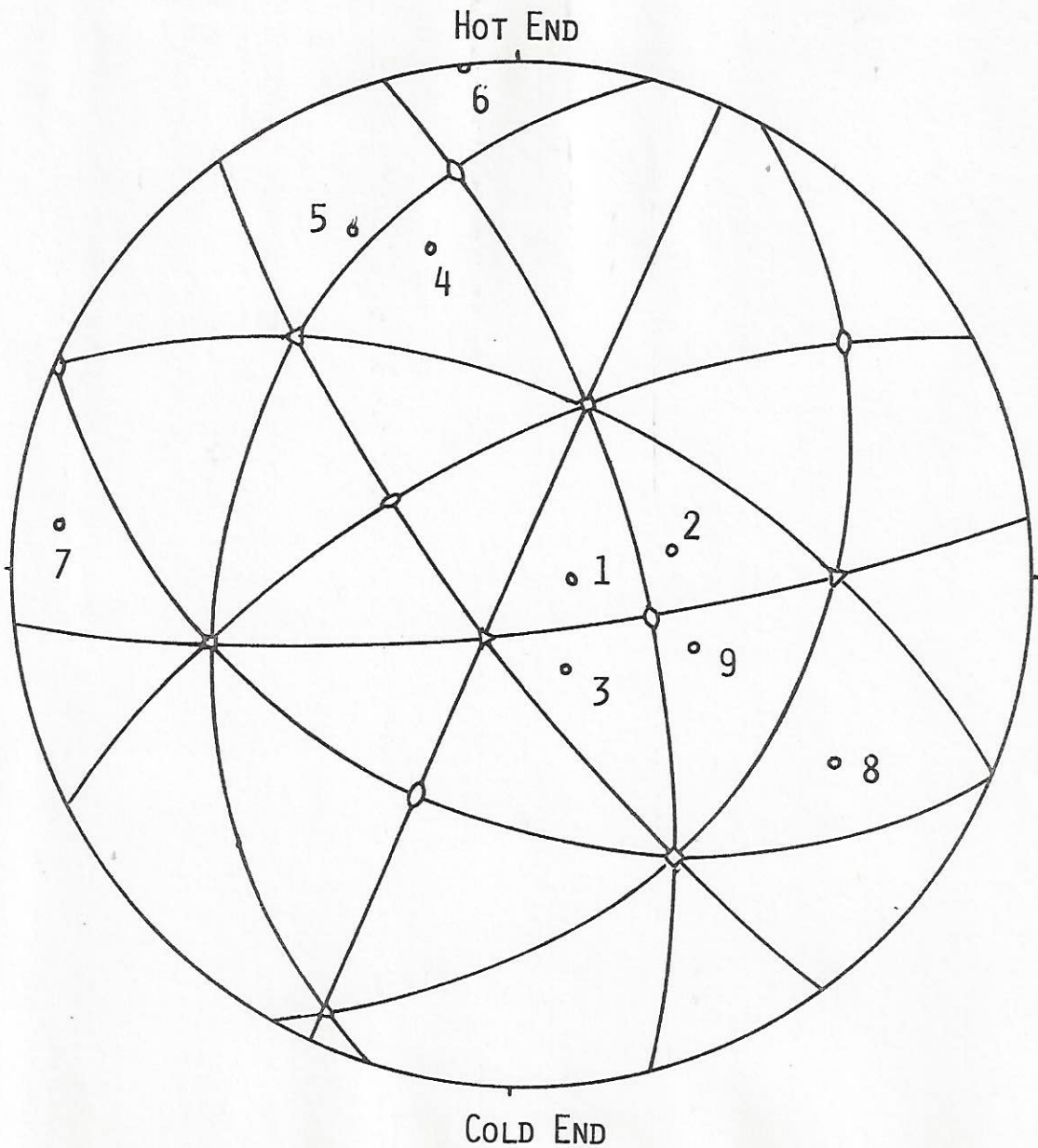
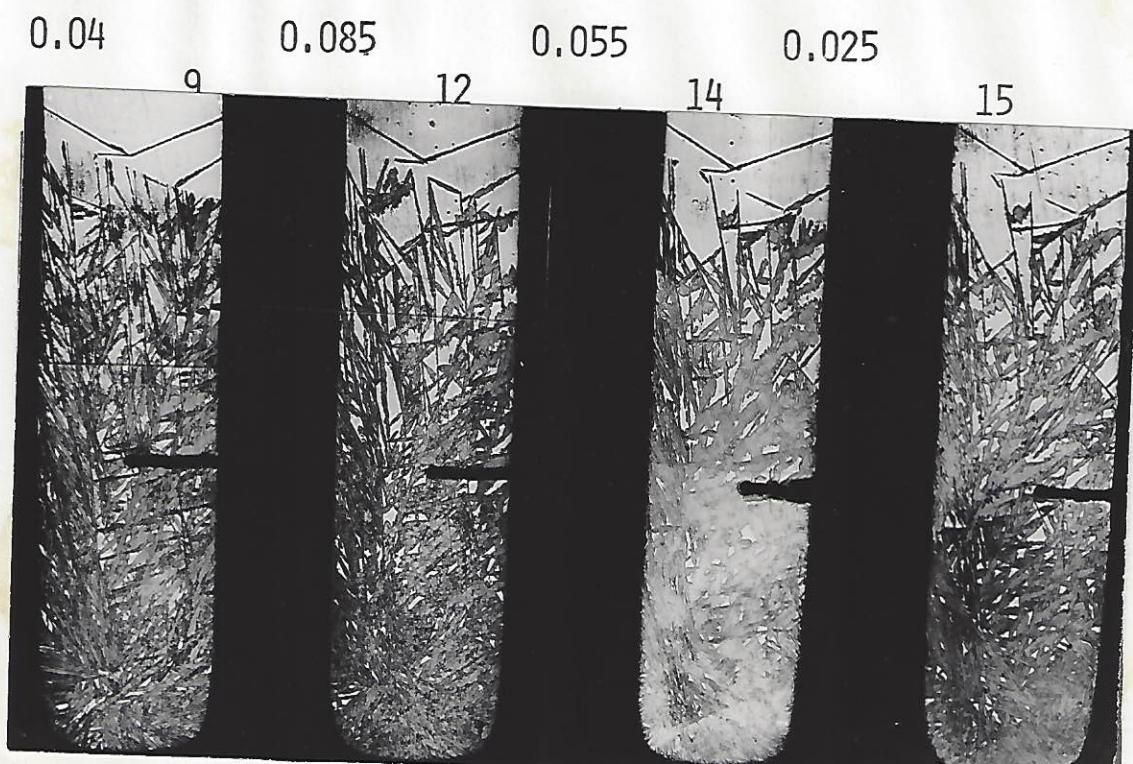
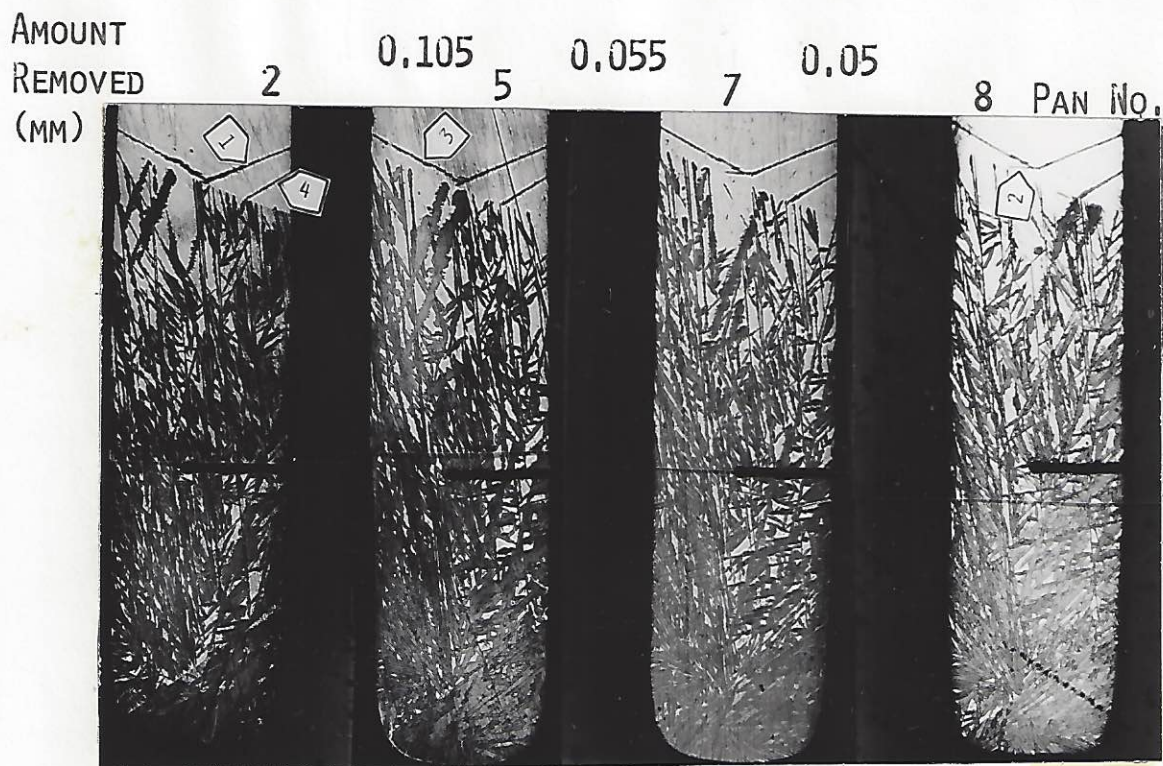


FIG. 20 RESULTS OF METALLOGRAPHIC HABIT PLANE
ANALYSIS OF SPECIMEN X1 (ALLOY 2)

FIG. 21 METALLOGRAPHIC PANORAMAS OF SPECIMEN Y2 (ALLOY 2)
(13.1X)



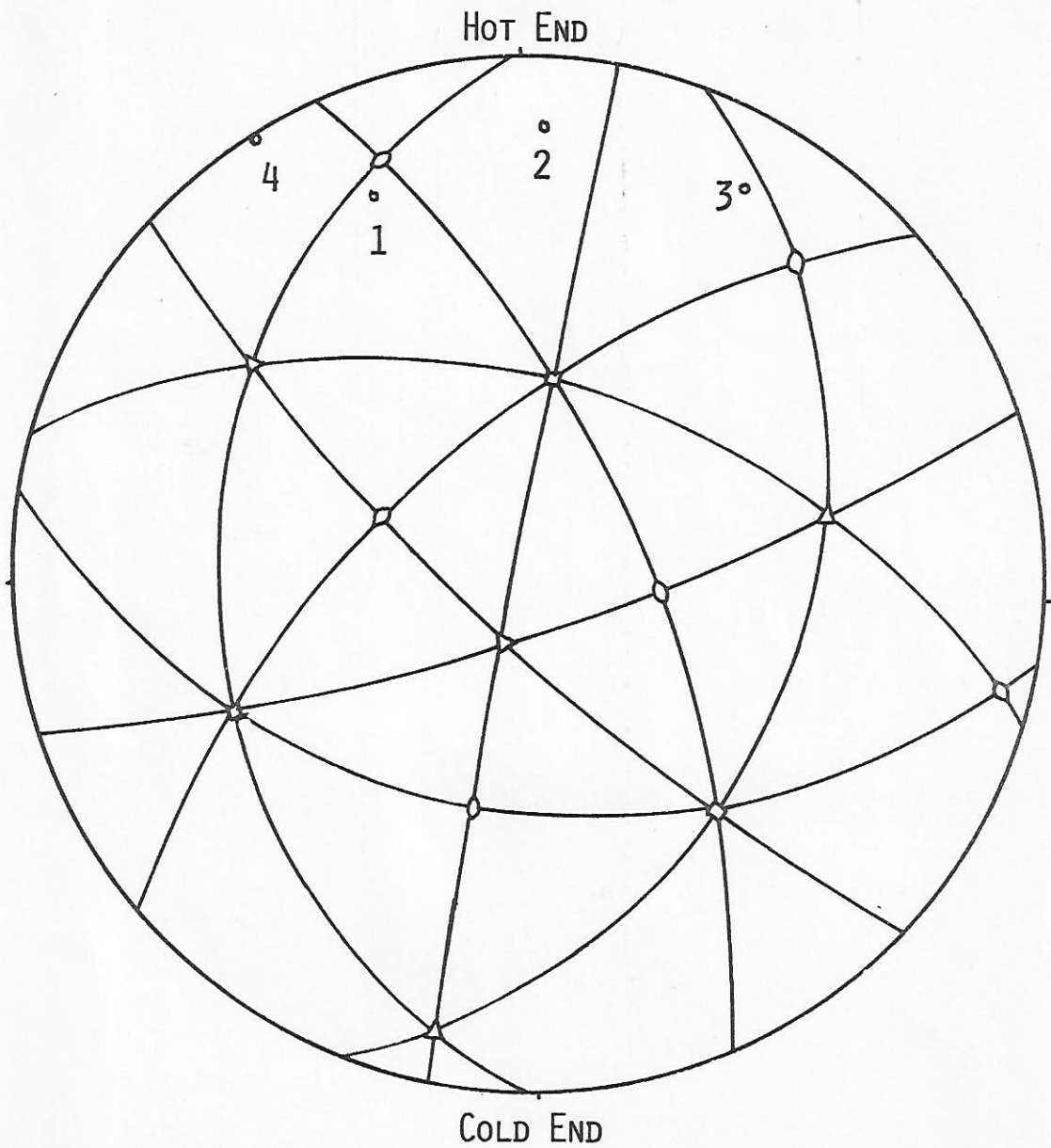


FIG. 22 RESULTS OF METALLOGRAPHIC HABIT PLANE
ANALYSIS OF SPECIMEN Y2 (ALLOY 2)

FIG. 23 COMPOSITION GRADIENT SPECIMENS (45.3X)

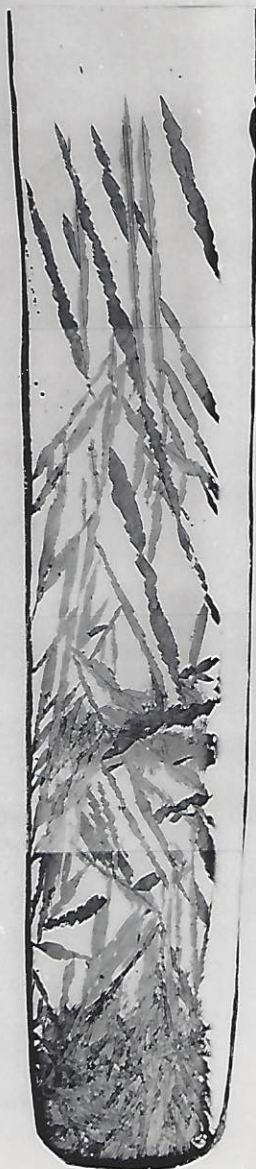
134 °K



223 °K



242 °K



257 °K



Thermodynamic Driving Forces

The data gathered in the various experiments involved the state variables of temperature and composition. These values allow calculation of the local thermodynamic driving forces at the sites of interest. The equations used are those due to Kaufman et al. (56) For the binary Fe-Ni system:

$$\Delta G^{\gamma \rightarrow \alpha'} = x_{Fe} g_{Fe} + x_{Ni} g_{Ni} + x_{Ni}^2 x_{Fe} g_{FeNi*} + x_{Fe}^2 x_{Ni} g_{Fe*Ni}$$

where:

$$g_{Fe} = -1303 - (1.78 \times 10^{-3})T^2 + (2.87 \times 10^{-5})T^3 - (4.91 \times 10^{-8})T^4$$

$$g_{Ni} = +940 + (0.74167 \times 10^{-3})T^2 - (0.5555 \times 10^{-6})T^3$$

$$g_{FeNi*} = 4430 + (0.2631 \times 10^{-2})T^2 - (0.6669 \times 10^{-6})T^3$$

$$g_{Fe*Ni} = -180 + (0.1233 \times 10^{-2})T^2 - (0.7696 \times 10^{-6})T^3$$

where:

x_i = atomic fraction of element i

T = temperature in $^{\circ}K$.

$\Delta G^{\gamma \rightarrow \alpha'}$ is the free-energy change in units of cal/mole. For the ternary Fe-Ni-C system:

$$\Delta G^{\gamma \rightarrow \alpha'} = \Delta G^{\gamma \rightarrow \alpha} + \Delta G^{\alpha \rightarrow \alpha'}$$

where:

$$\begin{aligned} \Delta G^{\gamma \rightarrow \alpha} = & x_{Fe} g_{Fe} + x_{Ni} g_{Ni} + x_C g_C + [x_{Ni}^2 x_{Fe} / (1-x_C)] g_{FeNi*} \\ & + [x_{Fe}^2 x_{Ni} / (1-x_C)] g_{Fe*Ni} + x_{Fe} x_C g_{FeC} \end{aligned}$$

where:

$$g_{FeC} = 14,200 - 8.34T$$

$$g_C = 2000$$

$$\Delta G^{\alpha \rightarrow \alpha'} = -50,000 [x_C^2 p^2 / (1-x_C)] + 0.7 x_C T \Phi(p)$$

where:

p = order parameter.

p and $\Phi(p)$ are tabulated. ⁽⁵⁷⁾ Some representative values are:

T/T_C	p	$\Phi(p)$
0.50	0.987	3.126
0.40	0.997	3.246
0.30	1.000	3.289
0.25	1.000	3.295

where T_C is given by:

$$T_C = 28000 x_C / (1-x_C) .$$

The uncertainty involved in these equations is greater for the ternary Fe-Ni-C system because a term for the Ni-C interaction is unknown, and the carbon-atom ordering energy is calculated for the Fe-C system only. Thus, the absolute values, said to be accurate to better than about 10-15% in the Fe-Ni system ⁽⁵⁸⁾ are probably not quite as good for the Fe-Ni-C system. On a relative basis, however, the difference values which are used to measure the magnitude of the autocatalysis, are probably correct to within a couple of percent.

CHAPTER V

DISCUSSION OF RESULTS

Introduction

In this chapter I will compare the data obtained from experiment with the theoretical models for autocatalysis. As there are two types of data (thermodynamic and phenomenologic), the main body of the discussion is divided into two sections, each of which treats the appropriate data.

By a process of elimination, the mechanism thought to be responsible for autocatalysis is determined. After determining this mechanism, its implications about other martensitic systems are explored, and a set of necessary conditions for "effective" autocatalysis are proposed.

Following these considerations, discussion of the polycrystalline data and the minimum driving force for growth takes place.

A brief discussion of the validity of the experimental autocatalytic assist values, and some interesting qualitative metallographic observations begin the chapter.

Heat-Flow Considerations

Because of the rapid nature of the martensitic transformation, it might be regarded as a nearly adiabatic process;⁽⁵⁹⁾ in the bursting alloys studied here, this is certainly an important consideration although some martensitic reactions show slower growth rates. The adiabatic behavior and the temperature-rise associated with the heat of reaction suggest that the bulk temperatures measured by the thermocouples (and subsequently used to find the maximum temperature of autocatalytic renucleation in a gradient specimen) may be considerably lower than the local temperatures encountered

by the renucleation sites near transforming martensite plates. An analysis of the heat flow can be employed to indicate the magnitude of the error which results.

In order to calculate the maximum adiabatic temperature-rise possible, $\Delta H_v^{\gamma \rightarrow \alpha'}$ and the specific heat (C_p) must be known. From Kaufman,⁽³²⁾ $\Delta H_v^{\gamma \rightarrow \alpha'}$ for Fe-30a/o Ni is -600 cal/mole (2500 J/mole). The molecular weight of Fe-30 Ni \approx 58 and $C_p = 0.11$ cal/g- $^{\circ}$ C (0.46 J/g- $^{\circ}$ C); thus, $\Delta T = \Delta H_v^{\gamma \rightarrow \alpha'} / (C_p \times MW) \approx 100^{\circ}$ C.

This calculation overestimates the temperature-increase because it does not take into account the elastic and plastic work which must be done to accommodate the martensite (usually estimated as 50-65 cal/mole⁽⁶⁰⁾ (210-270 J/mole)).

Having estimated the adiabatic temperature rise ΔT , the thick-film solution for Fourier's law of heat conduction will yield the unsteady-state temperature versus time and distance, at least for those times and distances appropriate to the problem. The liberation of heat as the martensitic interface goes by a given position is, of course, a dynamic phenomenon, but if one considers distances (x) of only a few microns, and times much greater than $t = x/v$, where v is the velocity of the interface, this solution is appropriate. Setting $x = 10$ microns and $v = 1.1 \times 10^9$ micron/sec, then $t = 10/10^9 = 10^{-8}$ seconds. Thus, at 10 microns distance, as long as we consider times of 10^{-7} seconds or greater, the thick-film solution is adequate.

The thick-film solution is given by:

$$\frac{\delta T(x,t)}{\Delta T} = \left\{ \operatorname{erf} \left[\frac{x+a}{\sqrt{4\alpha t}} \right] - \operatorname{erf} \left[\frac{x-a}{\sqrt{4\alpha t}} \right] \right\} \times \frac{1}{2} \quad (5.1)$$

where a is the half-thickness of the martensitic plate, ΔT is 100°C as noted above, and $\alpha = 0.11 \text{ cm}^2/\text{sec}$.

It has been suggested that the rapid adiabatic growth stage of martensite corresponds to the midrib growth only, with thickening taking place subsequently.⁽⁶¹⁾ Evidence for this is mainly metallographic; one notes a change in structure outside the region of the midrib (especially in T.E.M. investigations). Furthermore, intersecting plates are sometimes seen to penetrate each other to the midrib, thereby indicating that two stages of growth may take place. Theoretical considerations are also consistent with such a two-stage behavior. As transformation occurs, first an elastic precursor wave is radiated, travelling at the shear wave velocity c_s , followed by the martensite/austenite interface travelling at a slower velocity. The latter velocity is that measured as the growth velocity of martensite and may be as high as about $c_s/3$. According to the Van Karman analysis⁽⁶²⁾ ($v = [d\sigma/d\varepsilon/\rho]^{1/2}$), this velocity would be consistent with a stress-strain slope of about $\mu/10$. At static-test strain rates, in stage II (multiple slip), the normal slope of the shear-stress/shear-strain curve is about $\mu/400$ ⁽²⁵⁾ (and is temperature independent), which would suggest either that the reported martensitic growth rate is too high by a factor of $\sqrt{40}$, or that the transformation dislocations in the interface do not behave like ordinary dislocations. This discrepancy may also explain the difference in growth rates between the midrib and the remainder of the plate. If the midrib is elastically accommodated, it can grow at the rate-limiting velocity set by its transformation dislocations, rather than being limited by a plastic accommodation wave. One could consider the midrib as a case of a "supersonic" plastic wave. The lattice-invariant strain in the midrib

is twinning, which is possibly a faster form of deformation than slip. Others have suggested that a difference in martensitic morphology results because of the choice of twinning rather than slip as the lattice-invariant shear.⁽⁶³⁾ The question is then posed, does the transformation choose twinning rather than slip because it is propagating so rapidly,⁽⁶⁴⁾ or does it propagate so rapidly because it can choose twinning rather than slip?⁽⁶⁵⁾ To this writer it seems intuitively more logical that the high velocity of growth would be a consequence of the accommodation mode, rather than its determinant.

Thus, a reasonable choice for the effective value of "a" in eq. (5.1) is 1 micron, the approximate half-thickness of the midrib.⁽⁶⁶⁾ With x as 1.01 microns, $\delta T/\Delta T$ varies as follows:

$t = 10^{-8} \text{ s}$	10^{-7} s	10^{-6} s	10^{-5} s	10^{-4} s
$\delta T/\Delta T = 0.98$	0.82	0.33	0.11	0.03

With x as 10 microns, the values are:

$t = 10^{-8} \text{ s}$	10^{-6} s	10^{-4} s	10^{-2} s
$\delta T/\Delta T = 0.00$	0.04	0.04	0.003

The heat-flow calculations indicate that any error in temperature measurement will be appreciable (more than 10°C) only for autocatalytic nucleation which occurs very near to the midrib of the prior plate and within microseconds; for example, 90% of the heat has been conducted away 100 Å ahead of the interface after 10^{-5} seconds.

The implication of all this is that only if the autocatalytic nucleation takes place right at the γ/α' interface while the growth is

occurring, or very shortly thereafter, can the measured maximum temperature of renucleation be significantly in error due to adiabatic heating.

A further assumption of this calculation is that the matrix behaves as an infinite sink; no recalescence is allowed. In a bulk sample, this is not such a good approximation for a bursting alloy, as recalescence of about 40°C may be observed with large bursts. However, in the gradient experiments, the amount of transformation is relatively small in the region of the maximum temperature of renucleation, and the approximation becomes valid.

M_b Data Scatter

Much scatter in M_b values has been reported for most studies of bursting alloys, (13,54) and so the scatter found in this work does not seem excessive. Actually, because of the gradient, data scatter was expected to be larger than normal in much the same way that small-particle experiments show rather large depressions of M_s for some samples. The region in the gradient specimen which reaches the coldest temperature is small, and the change of finding a highly effective nucleation site there may be appreciably less than unity. For example, if 5°C of scatter is to be explained in a sample with a gradient of 100°C/cm, this would indicate that about 0.5 mm of the sample (of about 1 mm² cross-sectional area) is below the supposed M_b temperature, thus representing a volume of 5×10^{-4} cm³. If, indeed, there are 10^6 nucleation sites /cm³ at M_b , (11) there would not be any basis for this argument; however, bursting alloys are thought to show such extreme autocatalysis that a much smaller density of initial sites can produce measurable amounts of martensite. In terms of nucleation theories, a factor

of 5×10^2 (10^6 sites/cm³ $\times 5 \times 10^{-4}$ cm³) is not much of a discrepancy in the density of nuclei.

Qualitative Metallographic Observations

In conventional experiments performed on bursting alloys, even for single crystals, the resulting arrays of martensitic plates are very difficult to analyze via metallography. The few studies in the past attempting to do such work relied upon prior deformation of the austenite to inhibit the formation of several variants, and thus the morphology of the resulting martensitic structures was greatly simplified.

The problem with such previous investigations is that the dislocation arrays produced by the prior deformation may have had a serious influence on the subsequent processes of nucleation. Bokros and Parker⁽²⁴⁾ found that the habit variants in the four unit triangles about the $\langle 110 \rangle$ direction parallel to the Burger's vector of the operating slip systems were suppressed in deformed single crystals of Fe-31.7 w/o Ni. DePhilippi⁽⁴⁶⁾ observed that the four habit variants around a $\langle 110 \rangle$ direction 35.3° from the poles of the primary and conjugate slip planes, and 60° from the primary slip direction were enhanced in a deformed maraging alloy.

By transforming undeformed single crystals in a temperature gradient, much simplification of the morphology results without the necessity of modifying the processes of autocatalysis.

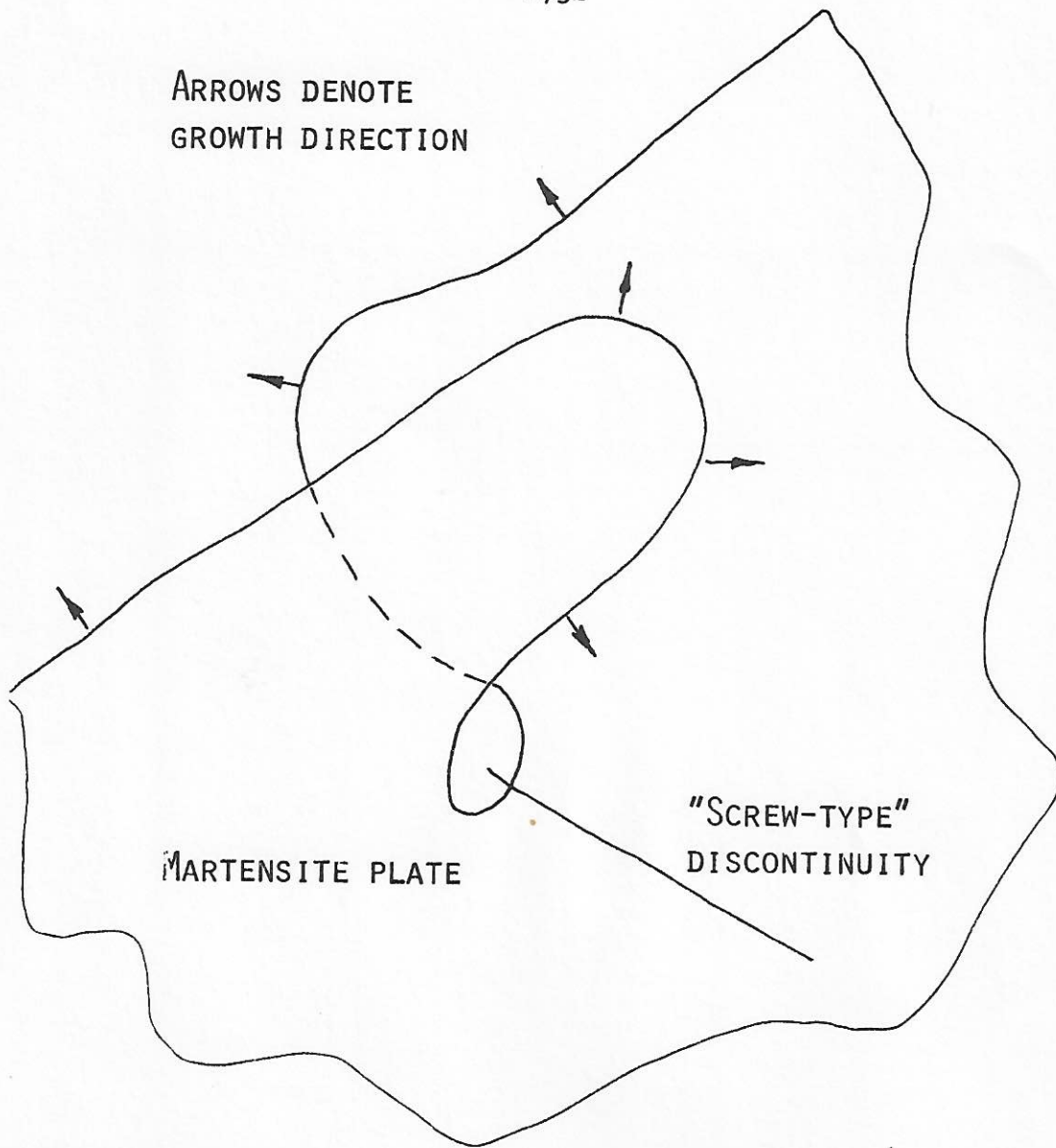
A few observations of a qualitative nature were made in the course of the extensive metallographic investigation which yielded the habit relations within the autocatalytic motifs.

The overall morphology is often composed of a mosaic of regular units. That is to say, small regions which contain repetitive patterns of martensitic plates are seemingly randomly juxtaposed. As the temperature increases above M_p in the gradient specimen, the size of these repetitive-pattern regions grows. A reasonable explanation for this behavior is that autocatalysis can act in two ways. It can include stimulation of random pre-existing nucleation sites (one per small region), and it can also operate independently of pre-existing sites in a repetitive manner within a small region. Consequently, with increasing temperature, relatively fewer random pre-existing sites can be triggered and the repetitive process can extend over larger volumes until the next random pre-existing site is encountered.

In several cases, plates of martensite appeared to contain multiple midribs nearly parallel to each other and very closely spaced; see for example, Figure 23 (242 °K) in the previous chapter. These were usually noted only in the very longest plates. The metallographic sectioning often showed that, in nearby sections, the plate was continuous without exhibiting this multiple midrib behavior. A simple explanation of the effect may be that, as the plate grows, it encounters local regions of lattice distortion which cause the plate to "ramp up or down" into folds or overlaps which produce the apparent multiple midribs, as illustrated in Figure 24.

Implications of the Energy-Assist Due to Autocatalysis

What does the value of 55-60 cal/mole (230-250 J/mole) found for the energy assist due to autocatalysis imply? In this section, we analyze each



ON A METALLOGRAPHIC SECTION, THE ABOVE WOULD LOOK LIKE:

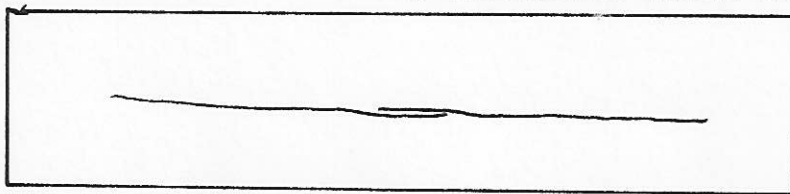


FIG. 24 A METHOD OF OBTAINING "MULTIPLE" MIDRIBS

of the proposed mechanisms.

The first is due to a thermodynamic elastic-stress-interaction energy assist to the driving force acting upon pre-existing nuclei. Neglecting the small volume expansion associated with martensite, what kind of shear stress level would be necessary to result in an energy of 50 cal/mole (230 J/mole)? From the equation $\tau\gamma = \Delta U_{\text{int.}}$, and assuming $\gamma = 0.2$, $\tau = 21,800$ psi (150 MPa).

At 25°C the critical resolved shear stress for Fe-30w/o Ni single crystals is 7800 psi (53.8 MPa), as determined by Breedis et al.,⁽³⁵⁾ and a value of 8800 psi (60.7 MPa) may be calculated for Fe-32w/o Ni from the work of Bush and Bokros.⁽⁶⁷⁾ These stresses are obtained from static tensile tests at strain rates of about 10^{-4} sec⁻¹. At the high strain rates involved in martensitic transformations, one might expect that the dynamic yield stress would be increased. FCC metals, however, exhibit very little strain-rate dependence.⁽⁶⁸⁾ To evaluate the possible increase in flow stress, it is necessary to know the strain rate at the elastic wave front in order to obtain the appropriate yield stress. In order to calculate this strain rate, the strain gradient associated with the wave front, as well as the velocity, is required.

Rise times for the elastic precursor waves of shock-deformed samples determined via free-surface-velocity measurements are in the range of 10^{-7} seconds for longitudinal waves.⁽⁶⁹⁾ The maximum elastic shear strain is probably on the order of 0.01, which would indicate a strain rate of about $10^{-2}/10^{-7} = 10^5$ sec⁻¹. The plastic-wave strain rate is probably of the same order of magnitude, or a little less. Use of the activation theory of plastic flow for an extrapolation over 8 or 9 orders of magnitude to

calculate the dynamic yield stress at these strain rates seems questionable; fortunately, shock-deformation experiments have been performed on invar-like alloys and data on the flow stress may be obtained directly.⁽⁷⁰⁾ Comparison of the static 0.2% offset yield stress (40,000 psi, 276 MPa)⁽⁷¹⁾ in a polycrystalline Fe-30% Ni commercial alloy (Compensator 30, Carpenter Steel Co., Fe-29.5 w/o Ni, 0.12 w/o C, 0.4 w/o Mn, 0.2 w/o Si), with the yield stress (44,600 psi, 308 MPa) calculated from the Hugoniot elastic limit (yielding under conditions of uniaxial strain) via the equation $\sigma = \sigma_{\text{Hel}} (1-2\nu)/(1-\nu)$ of the same alloy under shock-loading conditions shows that strain-rate effects cannot be called upon to raise the yield stress to the necessary level. Assuming that this increase, about 11%, applies proportionately to the CRSS values, a stress level of about 9300 psi (64.2 MPa) would be obtained (taking the average of the two literature values noted before as the static test value for Fe-31 Ni). Then, relying upon strain hardening to reach the necessary level would require a shear strain of about $(21.8 - 9.3) \times 10^3 / \mu / 400 \approx 0.5$. $\mu / 400$ is the work-hardening coefficient for stage II deformation in single crystals,⁽²⁵⁾ where μ is the shear modulus, with a value of 9.15×10^6 psi (6.3×10^4 MPa) at room temperature.⁽⁷²⁾ It seems unlikely that the austenite surrounding a martensitic plate would be subjected to a strain as large as 0.5 when the macroscopic shape change shear is only about 0.2.

Therefore, it is doubtful that elastic strain energy can be totally responsible for the observed magnitude of the energy assist.

The above discussion considered that the state of strain about a martensite plate was one of pure shear; however, biaxiality cannot be expected to raise the yield stress by more than about 15%, assuming that the

ratio of $\frac{\text{shear strain}}{\text{normal strain}} \geq 5$ as indicated by scratch-displacement measurements. (22)

Actually, once the yield point has been exceeded and gross dislocation movement has begun, the likelihood of a pre-existing site remaining unchanged and benefiting from the increased strain energy due to strain hardening becomes small. Rather more likely would be the creation of new sites.

It is well known that deformation above M_s up to the M_d temperature results in the formation of martensite. Furthermore, some martensite forms upon the start of plastic deformation at temperatures above the range where stress-assisted nucleation of pre-existing sites is believed to operate (above M_s^σ as defined by Olson and Cohen⁽⁷³⁾). Significantly, $M_s^\sigma - M_b$ measured by Bolling and Richman⁽⁷⁴⁾ in Fe-30 Ni and Fe-32 Ni is about half of $T_{\max}^{\text{rn}} - M_b$ measured in this work. For this reason, it seems reasonable to postulate that fresh nucleation sites created by plastic deformation are more potent than those pre-existing in the austenite. Their potency may be short-lived or over-shadowed, however, as studies of deformed austenites show that depression of M_s sometimes results. In interstitial-containing alloys, the phenomenon of stabilization is known to take place, and dislocation rearrangements would also be expected in low-interstitial alloys.

It is difficult to quantitatively discuss the possible high-potency defects created during deformation. The identity of the pre-existing embryos is little known, and the details of the deformation surrounding a martensitic plate--especially at the state where the midrib has stopped growing--is not directly accessible experimentally. Recent work indicates that "thin plate" martensites encountered in some alloy systems containing

substantial amounts of carbon with very low M_s temperatures may be useful in studying the dislocation arrays produced in the austenite. (75)

A semiquantitative analysis of the increased potency nucleation sites can be carried out by using the recent Olson-Cohen theory⁽³⁸⁾ of martensitic nucleation. These authors noted that all major martensitic reactions in metallic systems show an orientation relationship which exhibits near parallelism between the closest-packed planes of the parent and product phases. Accordingly, they reasoned that any operable nucleation site will tend to start out in a highly coherent form, and as the reaction proceeds will begin to deviate from this highly coherent stage to one in which an invariant-plane strain is ultimately established. This seems quite reasonable, since the surface area/volume ratio of the plate would be high in the initial stages, decreasing with growth, and the relative contributions of surface energy and strain energy would follow the same trend.

The highly-coherent initial nucleation site is a special type of stacking fault which can have a negative fault energy under conditions where the chemical driving force is sufficiently negative. If the fault energy is negative, the fault can grow, and this is the condition for athermal nucleation. If one takes into account a lattice-friction term for the motion of the partial dislocations bounding the fault, isothermal nucleation can also be explained. The equation for the fault energy is given by:

$$\gamma = n\rho_a (\Delta G^{\text{chem}} + E^{\text{str}}) + 2\sigma(n) \quad (5.2)$$

where γ is the specific fault energy, n is the thickness of the fault (in atom planes), ρ_a is the molar density of atoms per unit area of a close-

packed plane, ΔG^{chem} is the change in chemical free energy per mole, E^{str} is the strain energy per mole of fault, and $\sigma(n)$ is the surface energy per unit area of the fault. One sees immediately that when the magnitude of the chemical driving force exceeds the strain energy, it is possible to overcome the surface energy term if the fault is thick enough. In practice, however, n cannot be too large because of the unlikelihood of finding a large number of correctly spaced dislocations of the correct type (from which the fault forms). Substituting reasonable values of ΔG^{chem} , E^{str} , σ , and ρ_a , and setting $\gamma = 0$ (the nucleation condition in the absence of lattice friction) yields a value of 14.5 for n in Fe-31Ni at M_b . The description of the specific nature of the fault will be deferred until later, but the spacing of the dislocations necessary to provide the fault is 1 per 3 atom layers. Hence, the nucleating defect consists of about 5 dislocations. Putting into eqn. 5.2 the conditions at $T_{\text{max}}^{\text{rn}}$, with the elastic stress interaction energy estimated as:

$$\begin{aligned} \Delta U_{\text{int}} &= (\text{coupling factor} \times \text{estimate of flow stress, including strain-rate} \\ &\quad \text{and work-hardening effects} \div \text{flow stress to produce 50 cal/mole} \\ &\quad \text{assist}) \times 50 \text{ cal/mole} \\ &= \frac{0.78 \times (9300 + 0.2(\mu/400))}{21,800} \times 50 = 25.5 \text{ cal/mole (107 J/mole)}. \end{aligned}$$

This gives a value of n of 17.8 at $T_{\text{max}}^{\text{rn}}$. This more-potent nucleating defect is only about one more dislocation thick than the pre-existing ones. Thus, the energetics of the situation does not rule out a combination of stress-assisted and strain-induced autocatalytic nucleation; that is, strain-induced nuclei being stress-assisted by the elastic stress field of the original plate.

The third possibility of autocatalysis, that of interfacial generation of new nuclei, suggests itself from the model of the martensitic nucleus proposed by Olson and Cohen. A schematic description of the path followed by the nucleus is given in Figure 25. The separation into distinct steps is done to clarify the individual elements of the model nucleus, but they are more nearly simultaneous in nature (though the first shear must take place before the second shear). Conceptually, the interfacial mode of autocatalytic nucleation operates by permuting the roles of the various dislocation elements making up the nucleus. Lattice dislocations act as the origin of the first-shear fault in "regular" nucleation, whereas in autocatalytic nucleation, the dislocations associated with the plastic accommodation in the austenite due to a first-generation martensitic plate, as just discussed, or the interfacial dislocations themselves, must serve to generate the first-shear faults of the second-generation plates.

Because of the necessity of producing the appropriate orientation relations, as well as the correct shear direction and habit plane, the specific dislocation Burgers vectors for the various elements are uniquely specified by the Olson-Cohen theory for each habit plane. These are summarized in Table 5. To analyze the energetics of the interfacial mechanism, one must provide information about two factors: What is the value of n for autocatalytic nucleation and what sense and magnitude does the shear stress generated by the initial plate have with respect to the possible autocatalytic variant?

In order to answer the latter question the coupling factors calculated by Bokros and Parker⁽²⁴⁾ were used. These are listed in Table 6, modified to correspond to (3 10 15) as the initial plate instead of (10 3 15)

$$\frac{a_{\text{fcc}}[1\bar{1}0]}{2} \quad \text{---} \bigcirc \text{---} \quad \text{lattice dislocation}$$

-82-

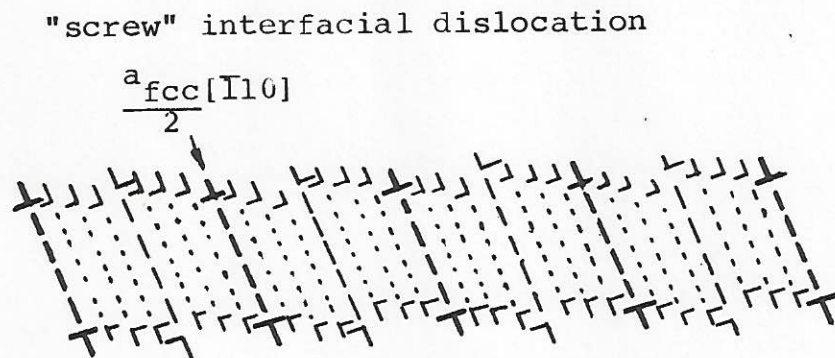
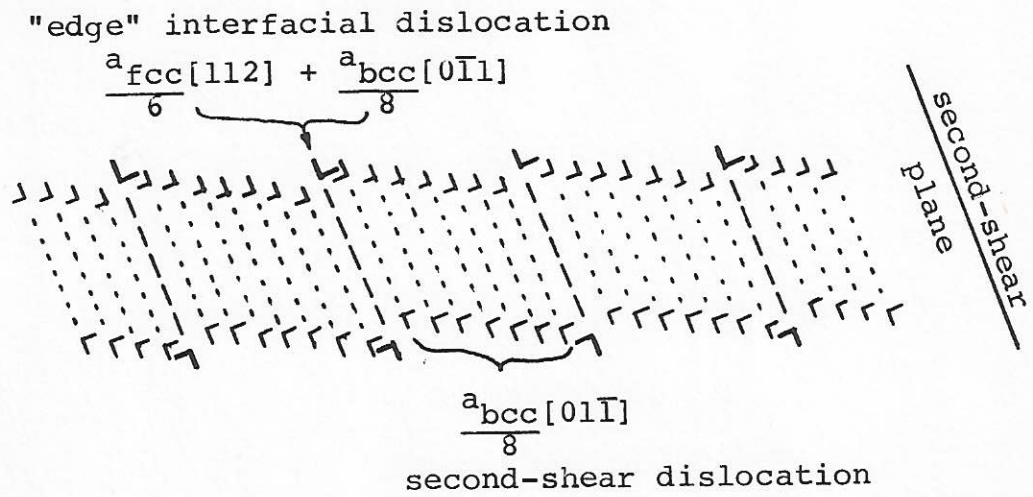
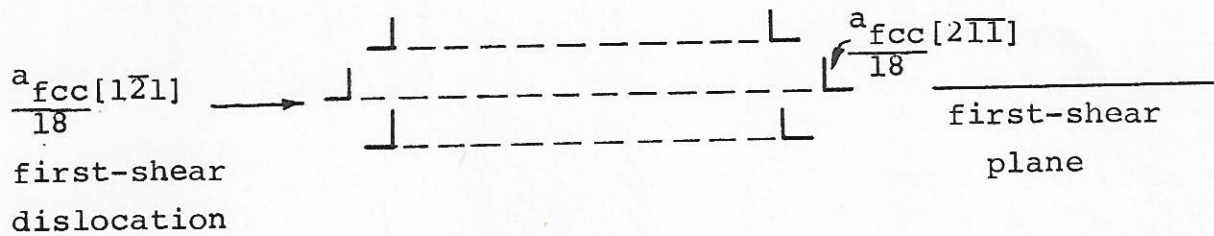


FIG. 25 OLSON-COHEN NUCLEUS DISLOCATION ELEMENTS

Table 5

-83-

Dislocation elements of Olson-Cohen martensitic nucleation site

1st shear	2nd shear*	"edge"* interfacial	"screw" interfacial	habit**			
(111) [1 $\bar{2}$ 1]	($\bar{1}\bar{1}$ 1) [$\bar{1}$ 21]	[$\bar{1}\bar{1}\bar{2}$]	[1 $\bar{1}$ 0]	3	10	15	2-2+5
[$\bar{2}$ 11]	($\bar{1}\bar{1}$ 1) [$\bar{2}$ 11]	[$\bar{1}\bar{1}\bar{2}$]	[$\bar{1}$ 10]	10	3	15	2+2-5
[$\bar{2}$ 11]	($\bar{1}\bar{1}$ 1) [$\bar{2}$ 11]	[$\bar{1}\bar{2}\bar{1}$]	[$\bar{1}$ 01]	10	15	3	2+5 2-
[11 $\bar{2}$]	($\bar{1}\bar{1}$ 1) [$\bar{1}$ 12]	[$\bar{1}\bar{2}\bar{1}$]	[10 $\bar{1}$]	3	15	10	2-5 2+
[11 $\bar{2}$]	($\bar{1}\bar{1}$ 1) [$\bar{1}$ 12]	[$\bar{2}\bar{1}\bar{1}$]	[01 $\bar{1}$]	15	3	10	5 2-2+
[121]	($\bar{1}\bar{1}$ 1) [$\bar{1}$ 21]	[$\bar{2}\bar{1}\bar{1}$]	[0 $\bar{1}$ 1]	15	10	3	5 2+2-
($\bar{1}\bar{1}\bar{1}$) [21 $\bar{1}$]	($\bar{1}\bar{1}\bar{1}$) [$\bar{2}$ 11]	[11 $\bar{2}$]	[110]	10	3	15	2+2-5
[121]	($\bar{1}\bar{1}\bar{1}$) [$\bar{1}$ 21]	[11 $\bar{2}$]	[$\bar{1}\bar{1}$ 0]	3	10	15	2-2+5
[121]	($\bar{1}\bar{1}\bar{1}$) [$\bar{1}$ 21]	[21 $\bar{1}$]	[0 $\bar{1}\bar{1}$]	15	10	3	5 2+2-
[112]	($\bar{1}\bar{1}\bar{1}$) [$\bar{1}\bar{1}$ 2]	[21 $\bar{1}$]	[011]	15	3	10	5 2-2+
[112]	(111) [$\bar{1}$ 12]	[121]	($\bar{1}$ 01]	3	15	10	2-5 2+
[211]	(111) [$\bar{2}$ 11]	[121]	[10 $\bar{1}$]	10	15	3	2+5 2-
($\bar{1}\bar{1}\bar{1}$) [$\bar{1}$ 21]	(111) [121]	[11 $\bar{2}$]	[$\bar{1}\bar{1}$ 0]	3	10	15	2-2+5
[211]	(111) [$\bar{2}$ 11]	[11 $\bar{2}$]	[110]	10	3	15	2+2-5
[211]	($\bar{1}\bar{1}\bar{1}$) [$\bar{2}$ 11]	[121]	[101]	10	15	3	2+5 2-
[112]	($\bar{1}\bar{1}\bar{1}$) [$\bar{1}$ 12]	[121]	[$\bar{1}$ 01]	3	15	10	2-5 2+
[112]	($\bar{1}\bar{1}\bar{1}$) [$\bar{1}$ 12]	[211]	[0 $\bar{1}\bar{1}$]	15	3	10	5 2-2+
[121]	($\bar{1}\bar{1}\bar{1}$) [$\bar{1}$ 21]	[211]	[011]	15	10	3	5 2+2-
(11 $\bar{1}$) [21 $\bar{1}$]	($\bar{1}\bar{1}\bar{1}$) [211]	[$\bar{1}$ 12]	[$\bar{1}\bar{1}$ 0]	10	3	15	2+2-5
[121]	($\bar{1}\bar{1}\bar{1}$) [$\bar{1}$ 21]	[$\bar{1}$ 12]	[110]	3	10	15	2-2+5
[121]	(111) [121]	[211]	[011]	15	10	3	5 2+2-
[112]	(111) [112]	[211]	[0 $\bar{1}\bar{1}$]	15	3	10	5 2-2+
[112]	($\bar{1}\bar{1}\bar{1}$) [$\bar{1}$ 12]	[121]	[101]	3	15	10	2-5 2+
[211]	($\bar{1}\bar{1}\bar{1}$) [211]	[121]	[$\bar{1}$ 01]	10	15	3	2+5 2-

* Both the 2nd shear and "edge" interfacial are on the same shear plane.

** Refers to habit chosen for differing lattice-invariant deformation.

Coupling factors calculated by Bokros and Parker
modified to refer to (3 10 15) instead of (10 3 15)

$\bar{3} \ \bar{15} \ 10$	0.9092
$3 \ \bar{15} \ 10$	0.9092
$\bar{3} \ 15 \ 10$	0.7770
$3 \ 15 \ 10$	0.6751
$\bar{15} \ \bar{3} \ 10$	0.4981
$10 \ \bar{15} \ 3$	0.4981
$15 \ \bar{3} \ 10$	0.4890
$\bar{10} \ 15 \ 3$	0.4890
$\bar{15} \ 3 \ 10$	0.3936
$\bar{10} \ \bar{15} \ 3$	0.3936
$15 \ 3 \ 10$	0.2827
$10 \ 15 \ 3$	0.2827
$15 \ \bar{10} \ 3$	-0.1155
$\bar{15} \ \bar{10} \ 3$	-0.2625
$\bar{15} \ 10 \ 3$	-0.2625
$15 \ 10 \ 3$	-0.4395
$10 \ \bar{3} \ 15$	-0.4793
$\bar{10} \ 3 \ 15$	-0.4793
$\bar{10} \ \bar{3} \ 15$	-0.5633
$10 \ 3 \ 15$	-0.6712
$3 \ \bar{10} \ 15$	-0.6854
$\bar{3} \ \bar{10} \ 15$	-0.7984
$\bar{3} \ 10 \ 15$	-0.8493
$3 \ 10 \ 15$	-1.000

as originally published.

Deciding upon an n value requires consideration of the interfacial dislocation elements and their distribution. There are three possible sets of interfacial dislocations which could act as the first-shear fault for an autocatalytic plate. Two of them are distributed every 8 planes, and the third is distributed every plane. See Figure 25. The $a_{\text{fcc}}/6$ [112] interfacial dislocations are spaced 8 planes apart, and their Burgers vector is 3 times the $a/18$ [121] of the required first-shear fault. Hence, their stacking density is $3 \times 1/8 = 3/8$ the required value. Accordingly, to provide n of about 18, as necessary to explain the results previously deduced, a fairly large number of these type dislocations (4 or 5) would have to be "squeezed" together, and thus seriously perturbed from their normal spacing.

Dislocation arrays provide a way of calculating the energy of low-angle boundaries. The functional form of the energy is $E = E_0 \theta (A - \ln \theta)$.⁽⁷⁶⁾ Because this relation is concave downward, it can be expected that deviation from uniformity of the dislocation spacing can occur. That is, the energy of two regions of $\theta = \theta_1$ and $\theta = \theta_2$, each with a given area A , would be lower than one region of area $2A$ with $\theta_1 < \theta < \theta_2$. Derivation of a quantitative result for the martensitic case will not be attempted. Although there remains some doubt as to the possibility of clustering the required number of this type of interfacial dislocations for nucleation, it does not have to happen with great frequency.

The $a_{\text{fcc}}/2$ [110] set of interfacial dislocations, also spaced every 8 planes, is not of the proper type. These dislocations can dissociate in the normal fcc manner, however, to yield the $a/6$ [112]-type dislocations in

the same density as the previously discussed set. The same argument about the number of dislocations being displaced from their normal positions applies. The $a/2[110]$ dislocation is screw-type in nature, however, and such a perturbation may be more likely before dissociation than after. Unfortunately, habits resulting from this set of dislocations do not have especially favorable coupling factors; only one out of the four possible factors is positive and that one is not large in magnitude (0.4). (See Appendix II.)

The $a_{\text{bcc}}/8[011]$ set of interfacial dislocations, when referred to the fcc lattice becomes $a_{\text{fcc}}/16 [112]$ -type. Thus, they are of almost the correct magnitude and stacking density to serve as first-shear faults for an autocatalytic nucleus. Conceivably, n could be quite large in this case (twin spacing/lattice parameter $\approx 140/3 \approx 46$). However, the coupling factor is negative for both the possible habits that might form. These two effects can be combined in Eqn. (5.2) for the nucleation condition, and rearranged into the following form (expressed in cal/mole):

$$-\Delta G = 2390/n + 123 - U \quad (5.3)$$

where U = coupling factor \times maximum amount of elastic stress interaction energy-assist. Setting $U = -0.25 \times 25 \text{ cal/mole} = -6.25 \text{ cal/mole}$ (26.2 J/mole), and $n = 46$, results in $-\Delta G^{\gamma \rightarrow \alpha'} = 182 \text{ cal/mole}$ (762 J/mole) at the theoretical $T_{\text{max}}^{\text{rn}}$. Since $-\Delta G^{\gamma \rightarrow \alpha'}(M_s) = 290 \text{ cal/mole}$ (1210 J/mole), this implies a possible $\delta \Delta G$ of about 110 cal/mole (460 J/mole). This value is greater than the measured energy-assist; however, in its calculation no attempt was made to correct for adiabatic heating or the small mismatch between the interfacial dislocation stacking density and the required

stacking density for a first-shear fault. The calculated value would be smaller if these factors were taken into account.

For the two other modes of interfacial nucleation using the other sets of interfacial dislocations, the analysis applied to stress-assisted strain-induced nucleation seems appropriate. That is, for the given values of driving force at T_{\max}^{rn} and the elastic stress interaction energy assist (25 cal/mole, 105 J/mole), a value of n is predicted requiring one dislocation more per autocatalytic nucleus than the pre-existing nuclei contain.

The only modification necessary is a slightly smaller energy-assist, because the coupling factors are less favorable, but that should have minimal effect.

To summarize here, the analysis of this section indicates that experimental results on the energetics of autocatalysis are not consistent with the hypothesis of stress-assisted nucleation of pre-existing nucleation sites. On the other hand, the results are energetically consistent with stress-assisted nucleation of more-potent nuclei produced by plastic accommodation in the parent phase. They are also consistent with simple predictions as to the efficacy of stress-assisted nucleation via interfacial dislocations.

To decide between the latter two mechanisms, consideration of the metallographic results is necessary.

Implications of the Metallographic Data

Having analyzed the energetic results and finding that a number of models remain feasible for autocatalytic nucleation, one asks if their predictions can be verified further. Of course the answer is yes, if they

predict different sequences of autocatalytic habits. It has been noted earlier that the autocatalytic groupings are at times significantly regular, and the habit plane variants within these groups can be determined. Therefore, the test is to compare the experimentally determined autocatalytic habit groups with those cyclic or repetitive sequences predicted by the models.

The stress-assisted strain-induced mechanism relies upon the plastic accommodation of the surrounding austenite to produce appropriate arrays of dislocations. These can then act as nucleation sites of higher-than-normal potency which will be further aided (or hindered) by the stress field around the original plate. We need to know (a) which dislocation arrays will form about a martensitic plate, (b) which habits can result from those dislocation arrays, and (c) which of the possible habits will be favored by the stress field existing around the initiating plate.

The first question can be answered by calculating the Schmid factors of the slip systems around a selected martensitic plate. To decide which slip systems would be activated, the absolute values of the Schmid factors obtained were used to rank the slip systems from highest to lowest probability. Additionally, since only five independent slip systems are necessary to accommodate any arbitrary shape change, the systems were ranked down to the point at which five independent slip systems could be obtained. The Schmid factors are tabulated in Table 7. The calculation is identical to the Bokros-Parker⁽²⁴⁾ procedure except that slip planes and slip directions are used (instead of habit planes and shear directions) in determining the appropriate direction cosines. Only perfect dislocations were dealt with, since the intrinsic stacking fault energies of the alloys considered

Table 7

-89-

Coupling factors for slip systems (absolute values)
activated by a (3 10 15) martensite plate

<u>Slip plane</u>	<u>Slip direction</u>	<u>Coupling factor</u>
(111)	$[\bar{1}01]$	0.385
	$[1\bar{1}0]$	0.409
	$[0\bar{1}1]$	0.795
$(\bar{1}\bar{1}1)$	$[1\bar{1}0]$	0.226
	$[\bar{1}0\bar{1}]$	0.657
	$[011]$	0.883
$(1\bar{1}1)$	$[011]$	0.580
	$[110]$	0.137
	$[10\bar{1}]$	0.442
$(\bar{1}11)$	$[110]$	0.498
	$[01\bar{1}]$	0.668
	$[101]$	0.170

are relatively high.⁽⁷⁷⁾ The determination of the combinations of slip systems yielding five independent ones was carried out by a graphical method suggested in Hirth and Lothe.⁽⁷⁸⁾

One by one, each of the slip systems thus chosen was then allowed to dissociate into partials, and the appropriate habit planes needing those partial dislocations as a first-shear were noted (Table 5). Finally, the appropriate coupling factor between the original plate and each of the potentially new plates under consideration was evaluated. If one of the higher positive coupling factors was obtained (>0.65), renucleation was assumed to have taken place. At this point, the effect of the triggered plate was then taken into account by noting the coupling factor between it and other possible autocatalytic nuclei produced by the original plate. Again, if a large positive coupling factor was obtained, renucleation was considered to have occurred in this case as well.

The process applied to the original plate was then followed for the autocatalytically-nucleated plates. This procedure led rapidly to the conclusion that one of two types of cycles would be followed. (For a more complete explanation of the process, see Appendix I). These are best illustrated upon stereographic projections (see Figure 26 and Figure 27). One of the cycles involves only four habit planes, and the other involves eight. The group of four corresponds to the same grouping found by Bokros and Parker.⁽²⁴⁾ The grouping of eight, which is one including "perpendicular coupling" (according to the Bokros and Parker terminology), is illustrated in Figure 28. As can readily be seen, this configuration suggests strongly the acute-angled zig-zag patterns long associated with bursting alloys.

----- PRODUCES NUCLEI FOR
 ——— ACTIVATES

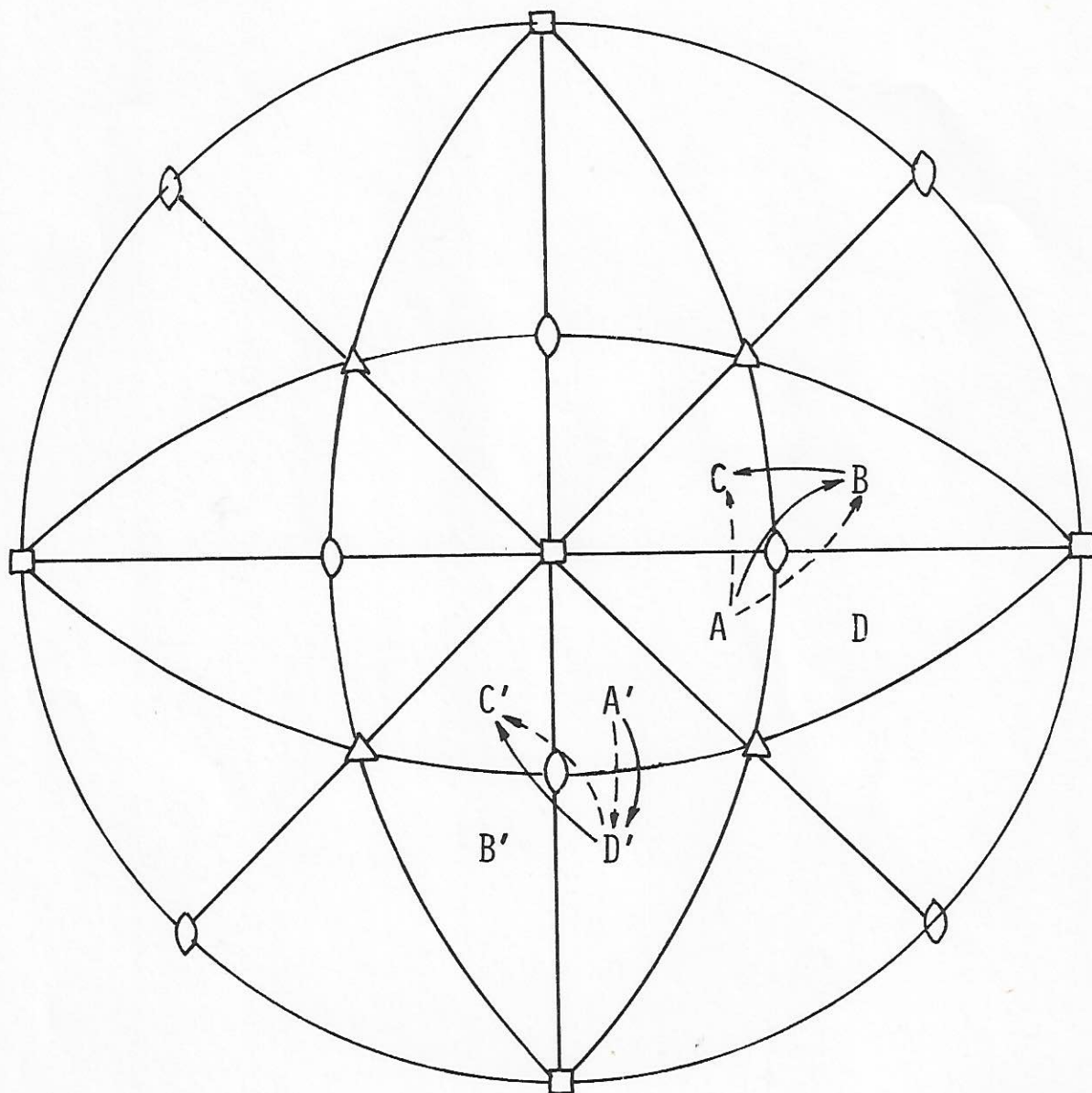


FIG. 26 POSSIBLE AUTOCATALYTIC SEQUENCES VIA
 "PARALLEL COUPLING" LEADING TO 4-HABIT VARIANT MOTIFS

1. $A \rightarrow B \rightarrow C \rightarrow D \rightarrow A$
2. $A' \rightarrow D' \rightarrow C' \rightarrow B' \rightarrow A'$

- - - - - PRODUCES NUCLEI FOR
 ——— ACTIVATES

-92-

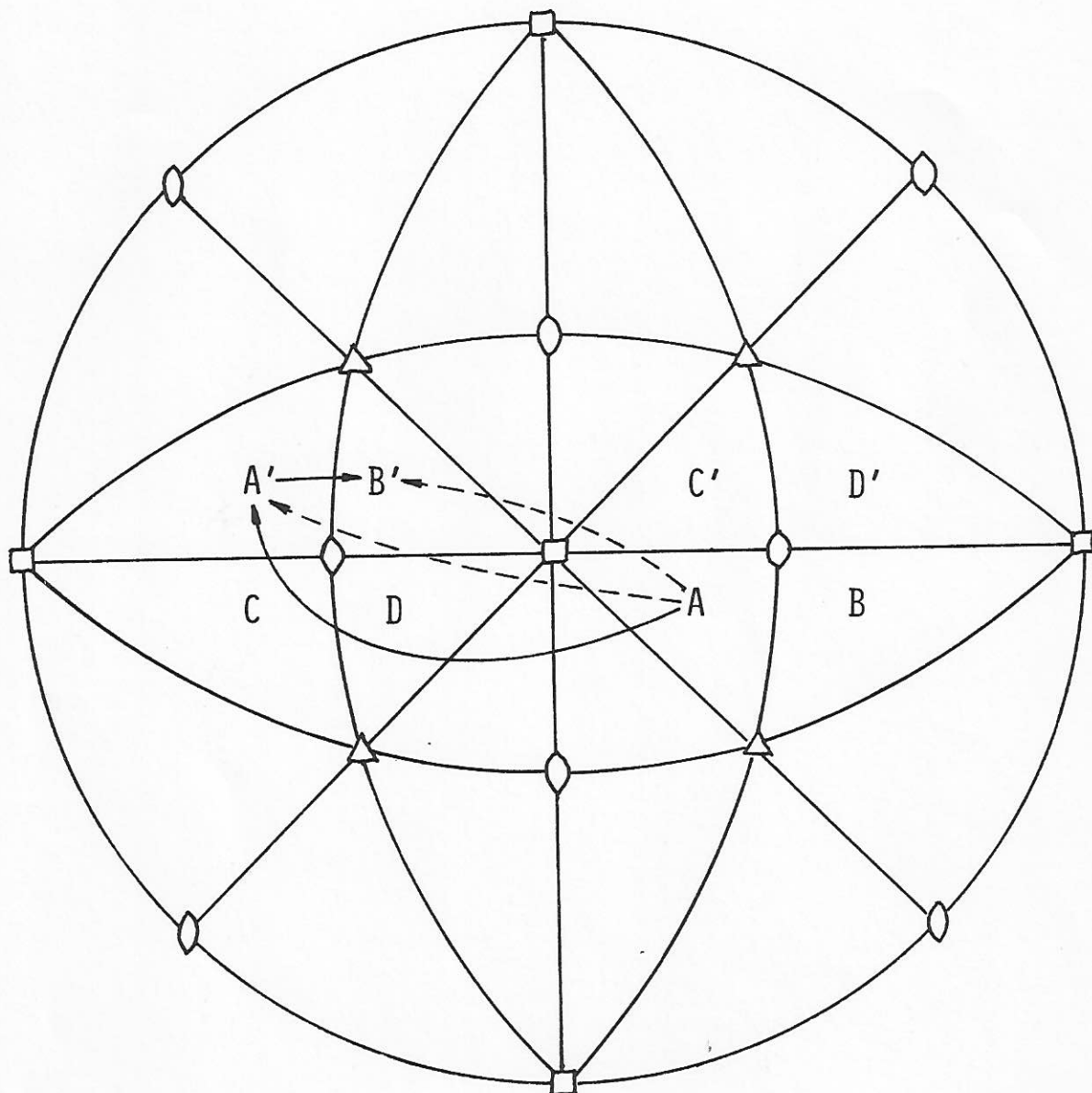


FIG. 27 POSSIBLE AUTOCATALYTIC SEQUENCE VIA
 "PERPENDICULAR COUPLING" LEADING TO 8-HABIT VARIANT MOTIF

BASIC SEQUENCE: $A \rightarrow A' \rightarrow B'$

REPETITIONS: $A' \rightarrow C' \rightarrow D', C' \rightarrow C \rightarrow D$

$B' \rightarrow B \rightarrow A$

SEQUENCES FOLLOWED: $1 \rightarrow 2 \rightarrow 3$, $2 \rightarrow 2' \rightarrow 2''$,
 $3 \rightarrow 3' \rightarrow 3''$, $3' \rightarrow 3'^+ \rightarrow 3'^{++}$

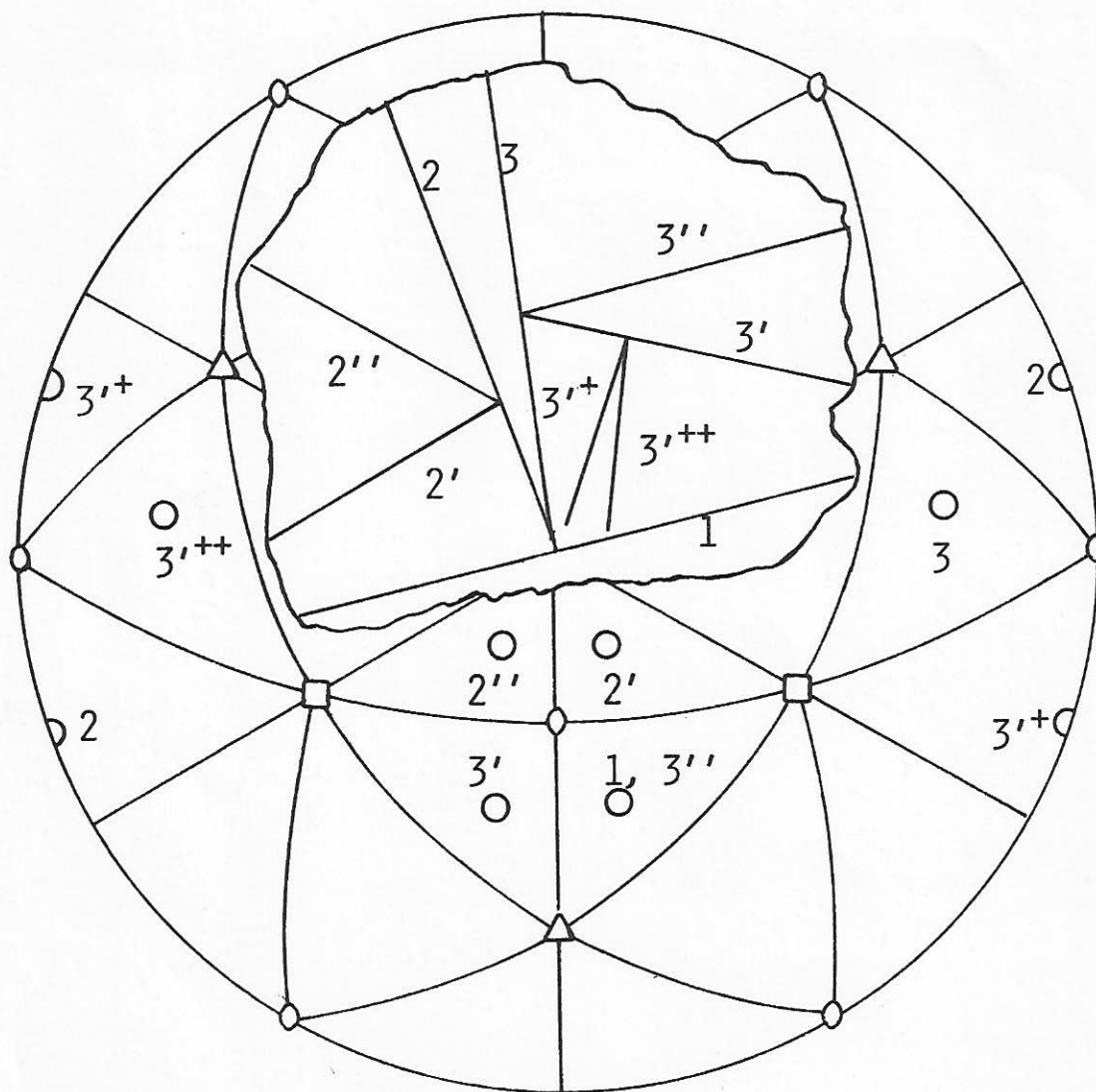


FIG. 28 A STEREOGRAPHIC PROJECTION INDICATING
 THE 8 HABIT VARIANTS OF "PERPENDICULAR COUPLING"
 AND A SIMULATED METALLOGRAPHIC SECTION SHOWING HOW
 IT LEADS TO THE ZIG-ZAG ARRAYS CHARACTERISTIC OF
 BURST MARTENSITES

Deciding upon the cyclic patterns arising from the interfacial models was easier, because the dislocations are specified by the Olson-Cohen mechanisms directly. See Table 5. Permutation of these elements leads to four possible cyclic patterns (also, see Appendix II).

The first permutation, in which the second-shear element of the first-generation plate acts as the first-shear element for an autocatalytic plate, produces two possible habits. However, both of these have unfavorable coupling factors. In determining the cyclic behavior the least unfavorable habit was chosen. The resulting cyclic arrangement is demonstrated in Figure 29.

The second permutation, in which the edge component of the interfacial dislocations acts as the first-shear element of the autocatalytic plate, also points to two possibilities. Both have favorable coupling factors. In determining the cyclic behavior, the more favorable one was chosen. This leads to the cycle exhibited in Figure 30.

The third and fourth permutations result from the screw component of the interfacial dislocation array. The third assumes that the screw dissociates in the plane of the second-shear of the initial plate, while the fourth assumes that it dissociates in the plane of the first-shear of the initial plate. Again, since two possibilities present themselves in each case, that with the more favorable coupling factor was chosen for deducing the cyclic behavior. These are presented in Figure 31 (for the dissociation in the second-shear plane) and Figure 32 (dissociation in the first-shear plane). The latter does not really seem operable, since no positive coupling factor is obtained. This permutation does not benefit from the increased value of n characteristic of the first type of permutation, and

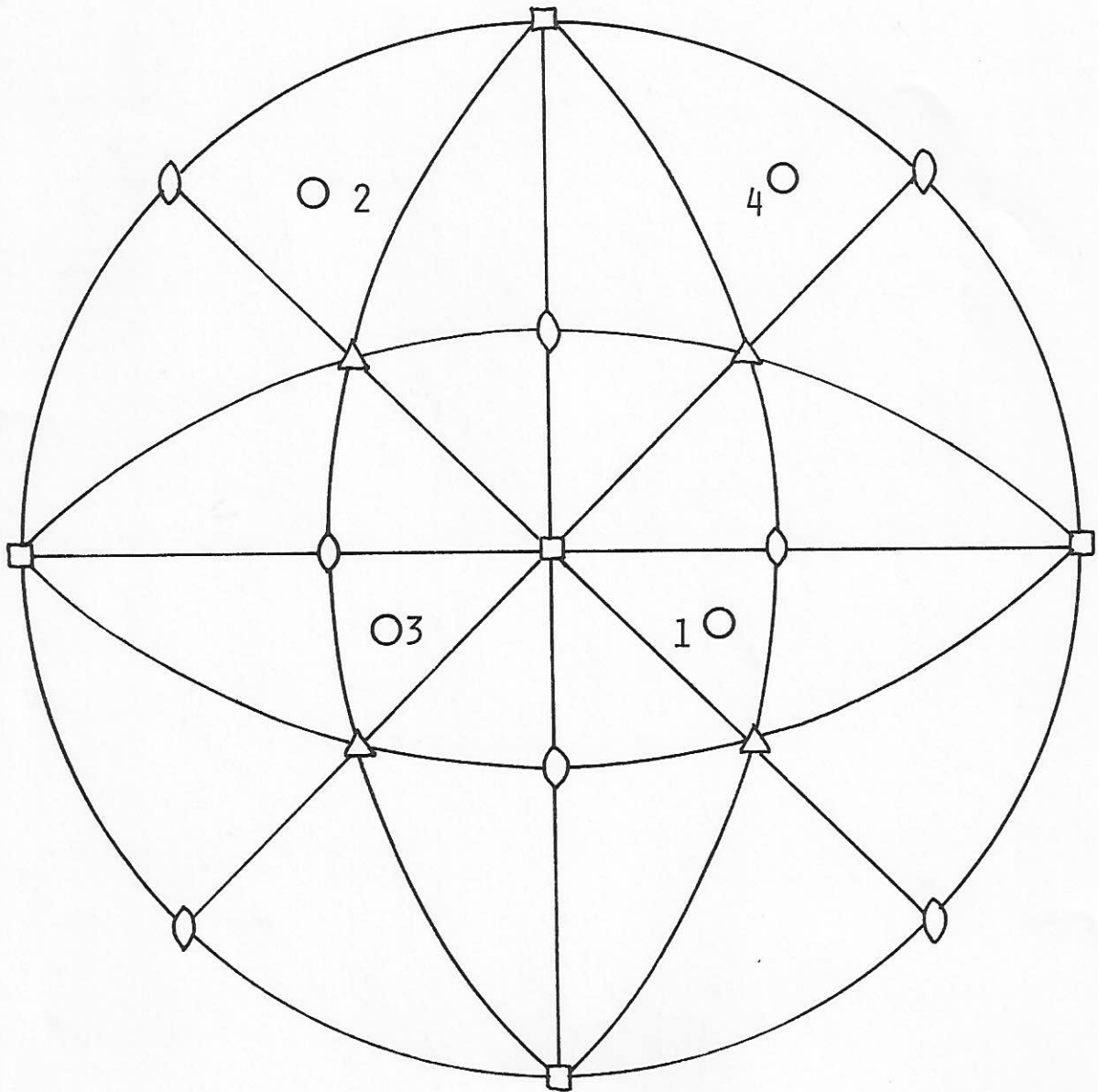


FIG. 29 AUTOCATALYTIC SEQUENCE USING SECOND-SHEAR
DISLOCATION AS FIRST-SHEAR DISLOCATION FOR AUTO-
CATALYTIC VARIANT

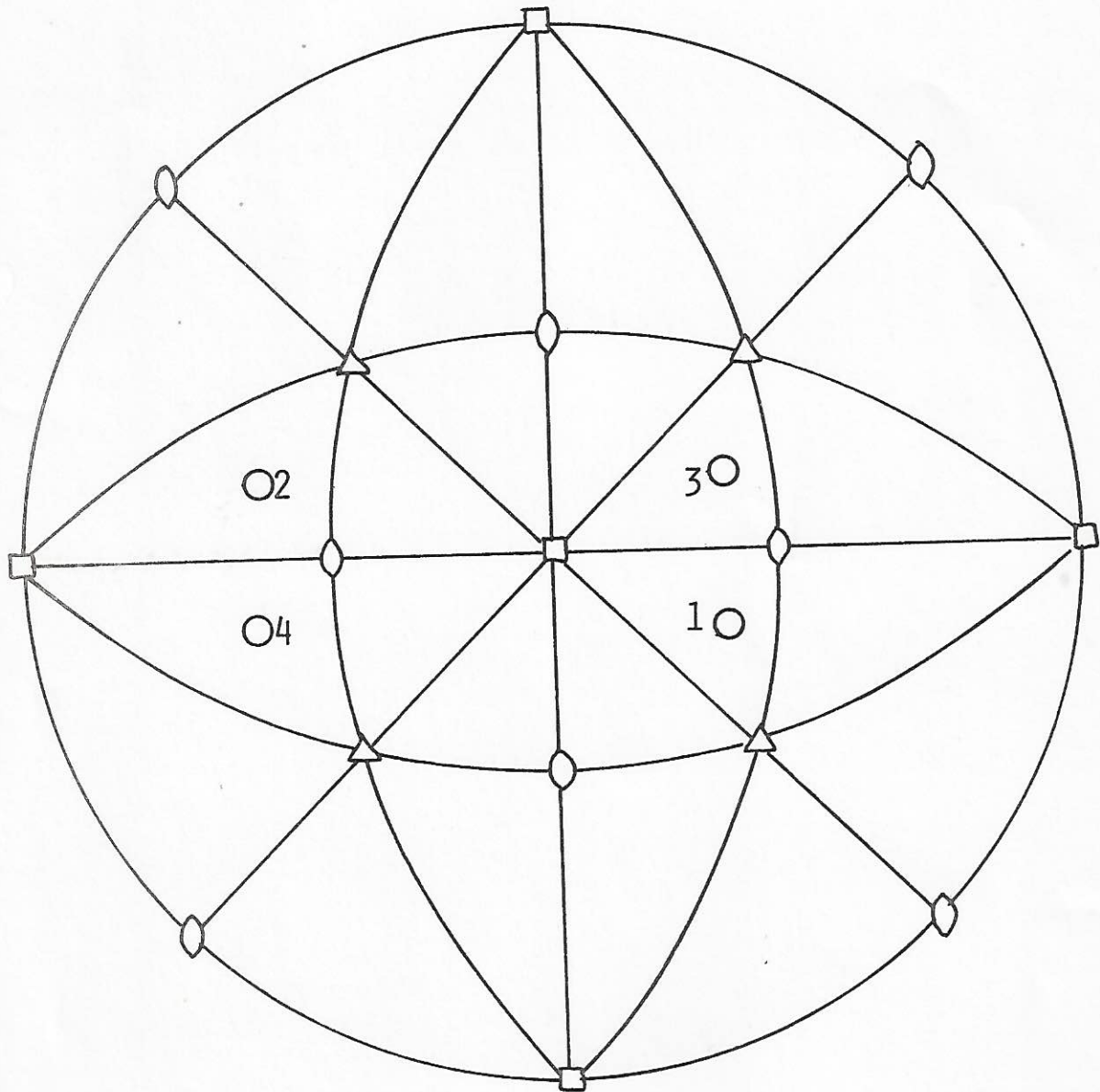


FIG. 30 AUTOCATALYTIC SEQUENCE USING "EDGE"
COMPONENT OF INTERFACIAL DISLOCATIONS FOR THE
FIRST-SHEAR DISLOCATION OF THE AUTOCATALYTIC
VARIANT

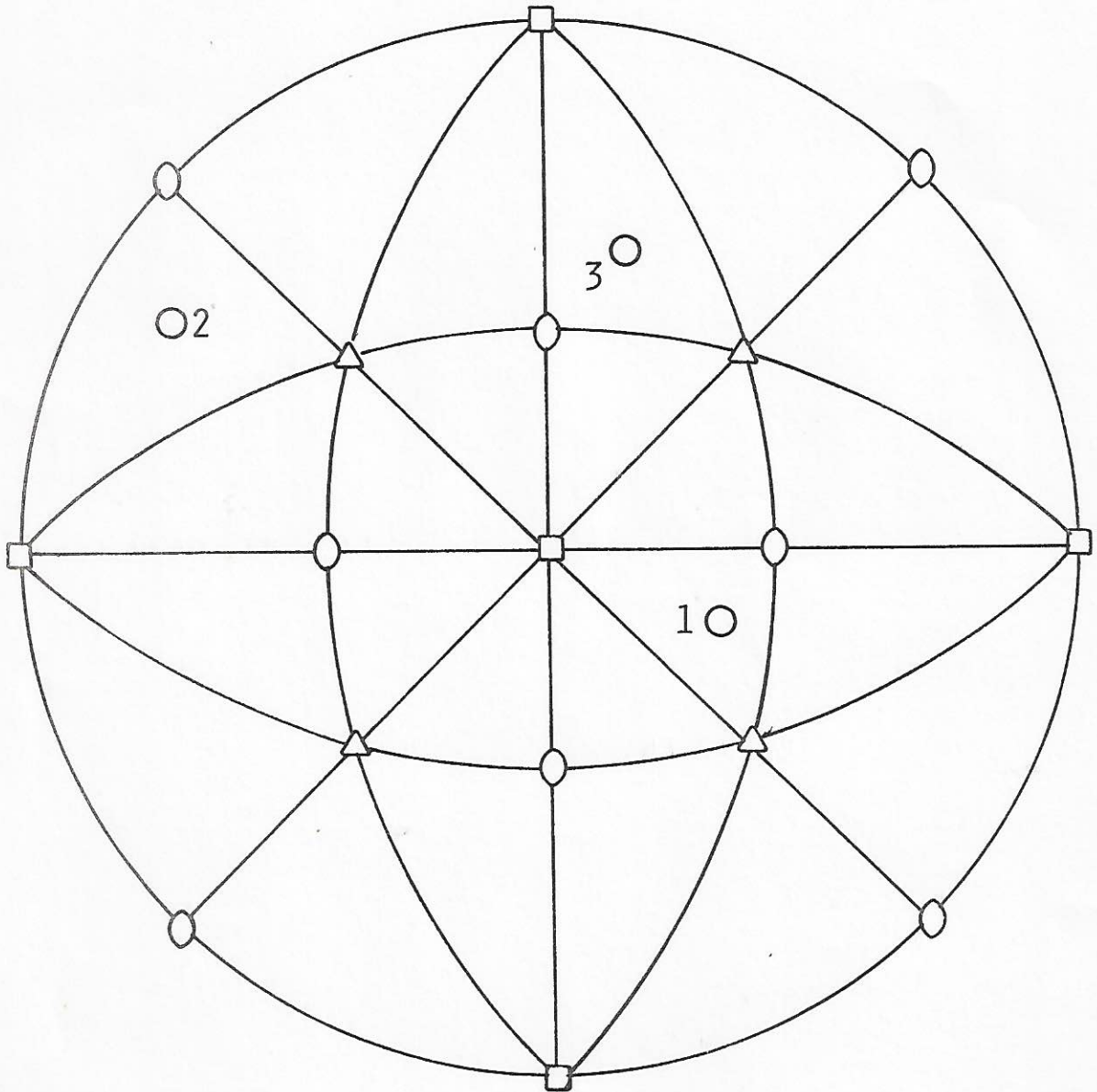


FIG. 31 AUTOCATALYTIC SEQUENCE USING "SCREW"
COMPONENT OF INTERFACIAL DISLOCATIONS FOR FIRST-
SHEAR DISLOCATION OF AUTOCATLYTIC VARIANT (SCREW
DISSOCIATES IN SECOND-SHEAR PLANE OF ORIGINAL
VARIANT)

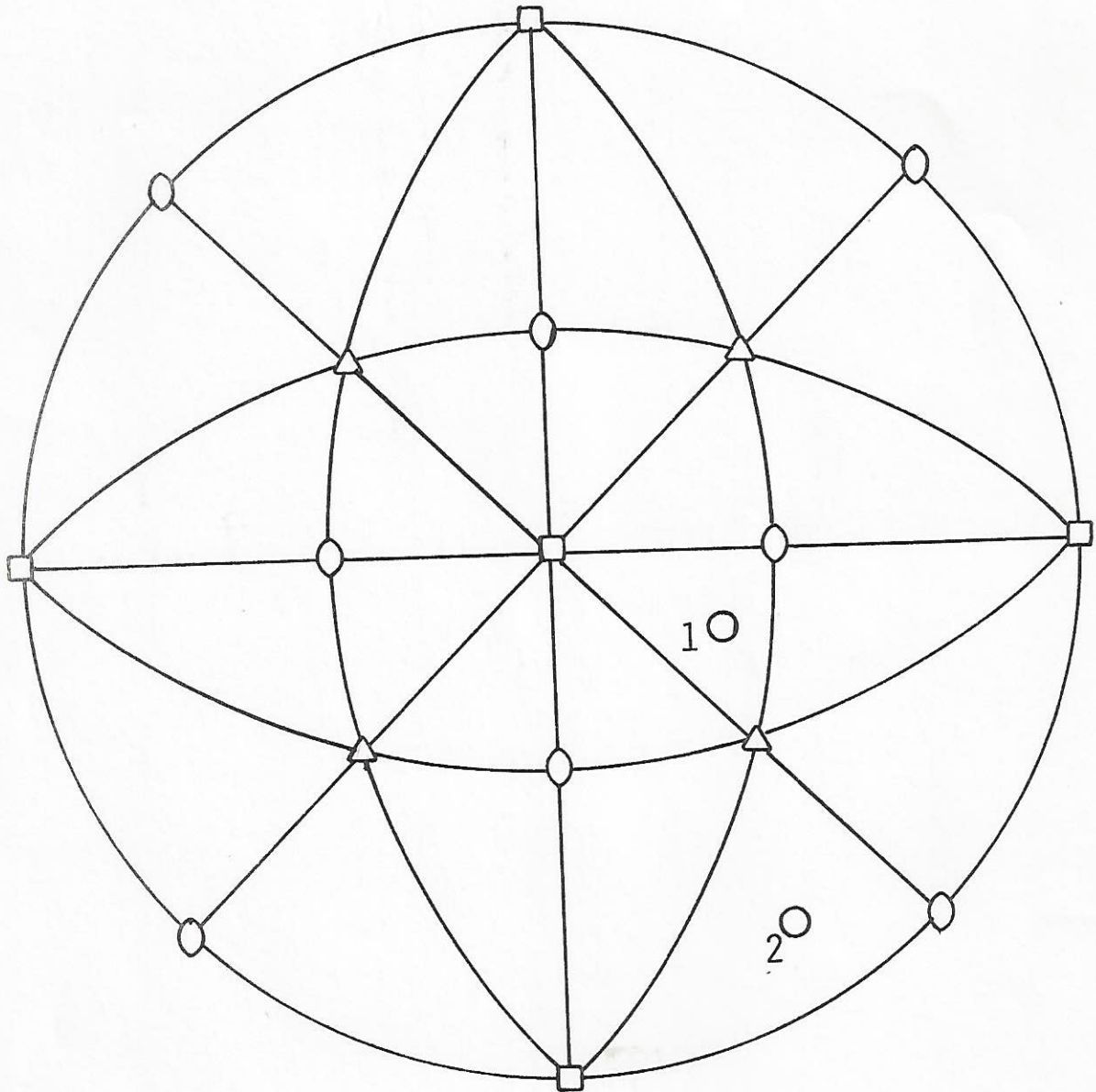


FIG. 32 SAME AS FIG. 31 EXCEPT SCREW DISSOCIATES
ON FIRST-SHEAR PLANE OF ORIGINAL VARIANT

so a positive coupling factor seems much more necessary.

Because of the complexity of the morphology, even in the regions of low martensite density, it is impossible to identify unambiguously the initial and succeeding generations with individual habit variants. This is compounded by the fact that complete serial sections were not possible because of material taken off in initial polishing and because sooner or later the sample came out of the mount. What was done, instead, was to look for repetitive motifs, and then to analyze the habit variants within these motifs. This is why such heavy emphasis was placed upon the cyclic behavior in the preceding analysis.

Examination of Figures 7 thru 22 of the previous chapter suggests that the groups of four about a common $\langle 110 \rangle$ direction are characteristic of non-deformed austenites as well as the deformed austenites of Bokros and Parker⁽²⁴⁾ and DePhilippi.⁽⁴⁶⁾ It thus appears that self-stresses generated by initial plates play an important role in the choosing of which autocatalytic variants are triggered, even though they cannot account for the whole autocatalytic energy-assist.

However, even though the predicted variants are consistent with the first-shear direction of the Olson-Cohen model, this circumstance is shared with other models,⁽⁴⁷⁻⁵¹⁾ and so cannot be taken as convincing evidence for the rest of the Olson-Cohen model. In fact, with respect to the predictions of the interfacial mechanisms, it cannot be said that the evidence supports their operation. Though the energetic analysis seems to indicate that they would be feasible, this may be because of the simplemindedness of the analysis. Another possibility is that it operates only under higher driving forces than are available in the regions where metallographic evidence is

obtainable. Finally, as previously mentioned, those processes taking place close to the interface would be most affected by the adiabatic rise in temperature associated with the initial plate formation. In the opinion of the author, this last reason is probably the determining one.

Overview and Implications of Autocatalysis

Summarizing earlier sections, autocatalysis in Fe-Ni bursting alloys has been found to result from stress-assisted nucleation of strain-induced nuclei produced by the accommodation deformation of an initial plate.

If this were a general mechanism of autocatalysis, then all martensitic transformations should exhibit similar kinetics; however, they do not. The following is an attempt to consider what variations may result, and why.

As the Ni content of binary Fe-Ni alloys is reduced below about 29 - 30 w/o, the burst tendencies of these alloys diminish rapidly.⁽³²⁾ Simultaneously, the M_b temperature rises to above the ambient, and the habit plane shifts to (2 2 5).⁽⁴³⁾ While remaining reasonably plate-like, the microstructure is quite ragged, the midrib feature is lacking, and the lattice-invariant shear system is no longer predominantly twinning (a tendency already begun in the lower Ni (3 10 15) martensites). Yet, the macroscopic shape change remains similar in magnitude and direction.^(43,79)

How do these trends affect the burst tendencies of (2 2 5) martensite?

Machlin⁽²²⁾ suggested that (2 2 5) plates could not couple as effectively as (2 5 9) because the directions of motion of the austenite of the appropriate groups are not as parallel as in the (2 5 9) case. The shear direction assumed by Machlin is not consistent with the best contemporary measurements available, however. His choice of shear direction led to the

prediction of only 12 variants, whereas there are in reality 24.

Nevertheless, the idea is helpful, and it seems worthwhile to re-investigate it. Rather than pursue his original approach, we shall adopt the method of Bokros and Parker⁽²⁴⁾ and calculate the coupling factors of the various groups.

Experimental measurements of the shape-change direction in (2 2 5) martensites⁽⁷⁹⁻⁸²⁾ have displayed large amounts of scatter, some of which has been attributed to measurements on "surface" plates.⁽⁷⁹⁾ The results of Jana and Wayman⁽⁷⁹⁾ show the least amount of scatter, and lie within the scatter limits of other investigators. We shall use their data in calculating the coupling factors, which are presented in Figure 33.

Comparison with the (3 10 15) case (plotted in Figure 34) shows immediately that Machlin was correct. The values for maximum coupling are reduced for the (2 2 5) case. Indeed, the group of four variants about a common $\langle 110 \rangle$ direction is no longer an efficient type of coupling. Furthermore, the strain-induced analysis for the (2 2 5) case (see Appendix I) indicates that only perpendicularly coupled groups (which do not occur with great frequency) are likely to form, if one uses the same cut-off point on the coupling factors as for the (3 10 15) case. Furthermore, only half the number of habits (4) are involved vs. the (3 10 15) perpendicularly coupled case (in which 8 are involved).

Consequently, it appears that the changeover from burst to non-burst characteristics is governed by steric factors in this instance.

Such arguments cannot be used for the case of ordered Fe_3Pt alloys, which are known to change from burst behavior (when disordered, and with a relatively high M_s) to thermoelastic behavior (when ordered, and with a very

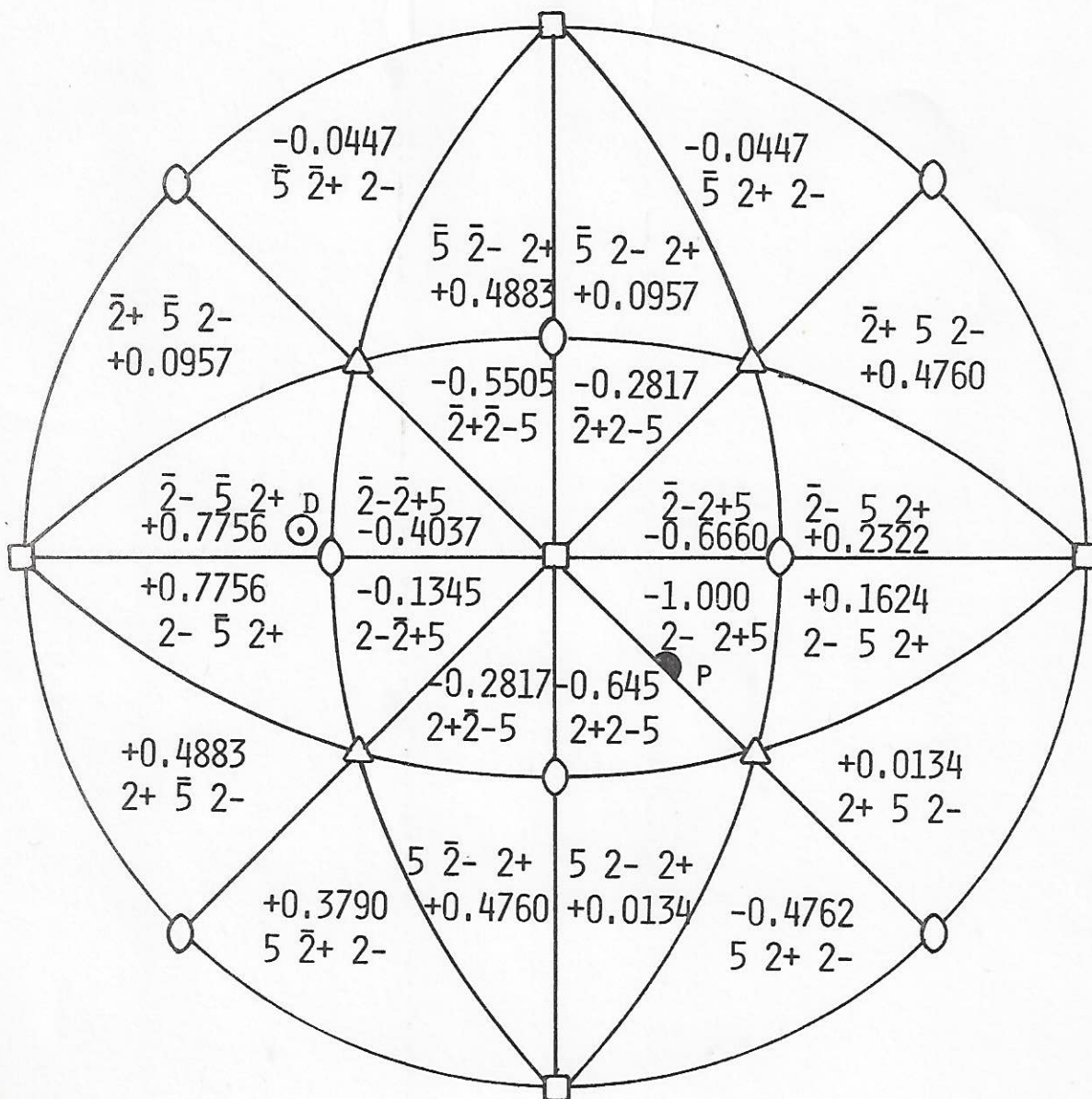


FIG.33 COUPLING FACTORS BETWEEN $(2- 2+ 5)$ AND OTHER $(2 2 5)$ -TYPE VARIANTS (P = HABIT PLANE, D = SHEAR DIRECTION)

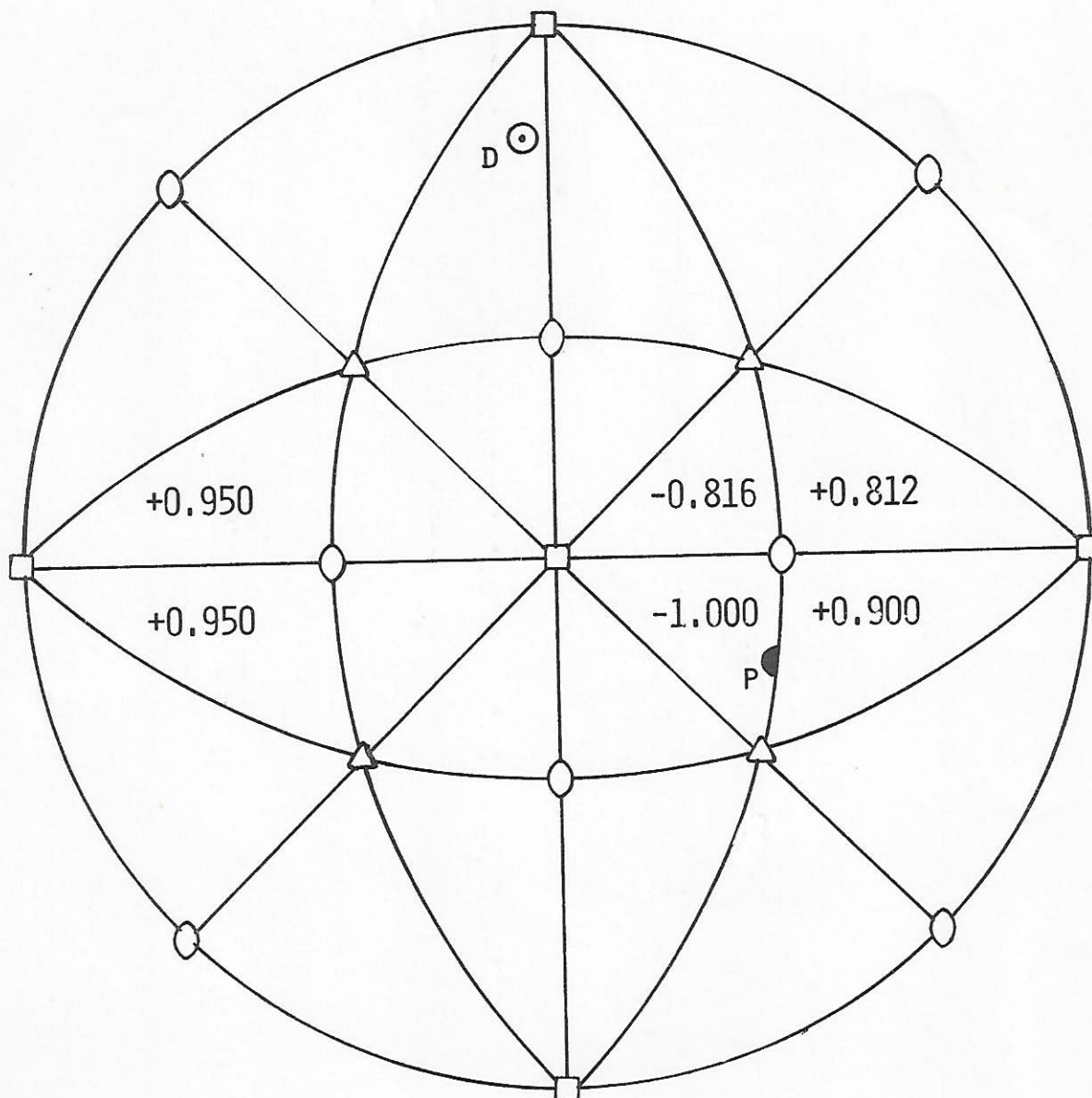


FIG. 35 SELECTED COUPLING FACTORS BETWEEN
(3 3 1)-TYPE HABIT VARIANTS (P = HABIT PLANE,
D = SHEAR DIRECTION, FOR CU-AL-NI)

2. Production of appreciable numbers of nuclei via plastic deformation. This seems to be determined by a large driving force at M_s , which ensures that purely elastic accommodation becomes unrealistic.

3. The operable nuclei must also be of an appropriate nature so that they can be stimulated by the stress field of the plate producing them.

Composition-Gradient Results

The composition-gradient experiments were undertaken because they offered some unique advantages.

They are an experimental cross-check upon the temperature-gradient experiments. Since the variables of temperature and composition were involved in both experiments, data from both types could be plotted on a single graph of temperature vs. composition. One set of results would plot vs. the composition axis at constant temperature, and the other vs. the temperature axis at constant compositions. Knowing the results from the composition-gradient experiments should, in principle, allow prediction of the results of the temperature-gradient experiment vs. composition, and vice-versa.

Additionally, the two experiments might serve to separate the differing effects upon the martensitic morphology of temperature and composition.

In retrospect, considering the difficulties encountered in quantitatively analyzing the composition gradients over small distances, the preferred approach to obtaining the autocatalytic behavior as a function of composition would be via a series of temperature gradient experiments on samples of different composition in the range of interest.

In doing the microprobe analysis of the composition-gradient samples, the nickel concentrations obtained by the technique described in Chapter 3 and listed in Table 4 were somewhat lower than expected.

First, the concentrations obtained from the probe data did not agree with the concentrations obtained by comparing the measured reaction temperatures with M_s vs. composition data in the literature.⁽³²⁾ Secondly, probe measurements taken in the high-nickel composition region indicated a lower nickel content than did the chemical analysis of that part of the sample.

Because of these discrepancies, it was decided not to use the absolute values obtained from the probe. Instead, the reaction temperatures were employed to infer the M_b compositions and the differences in composition obtained from the probe profiles then yielded the renucleation-limit and growth-limit compositions.

Because of the insensitivity with composition of $\partial \Delta G^{\gamma \rightarrow \alpha'} / \partial C|_T$ the values of $\delta \Delta G$ obtained via this method are not influenced appreciably by the shift in compositions; the values for $\Delta G^{\gamma \rightarrow \alpha'}$ at T_{\max}^{gr} are affected, however.

The modified composition-gradient results, and the Fe-31Ni temperature-gradient results are shown in Figure 36 and Table 8. It is seen that the two sets of values agree quite well.

With the exception of one point, the values lie on nearly straight lines. The value of the anomalous point is subject to question, as the standard deviation of the counting rate at the nearest measured position was about three times that for the other points measured on the same sample. The continuous scan profile also suggests that a lower concentration

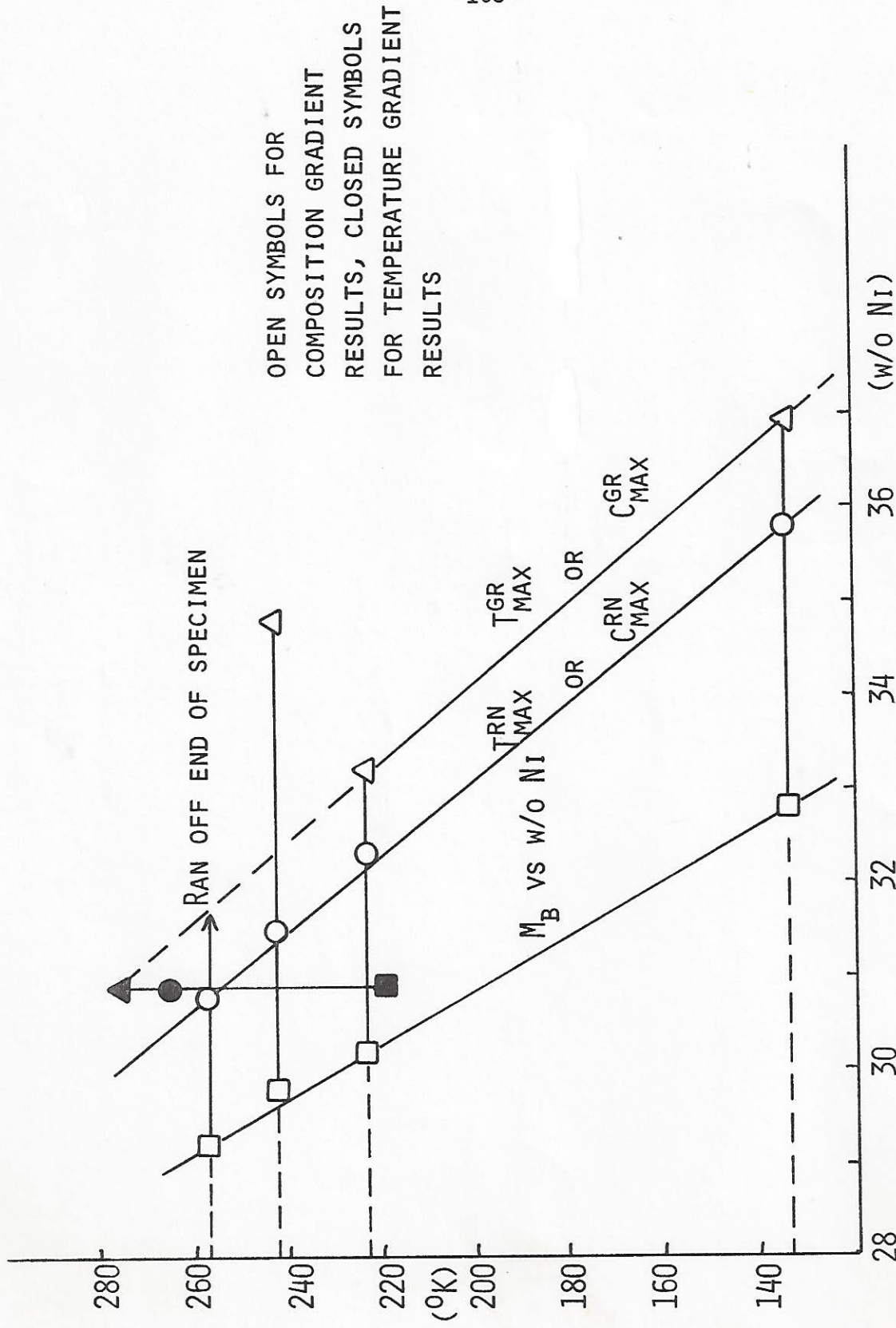


FIG. 36 TEMPERATURE GRADIENT RESULTS FOR ALLOY 4 SUPERIMPOSED UPON COMPOSITION GRADIENT RESULTS MODIFIED AS NOTED IN TEXT

Composition-gradient driving forces
using modified microprobe results

M_b	C_{M_b} (w/o Ni)	$C_{max}^{rn} - C_{M_b}$ (w/o Ni)	$C_{max}^{gr} - C_{M_b}$ (w/o Ni)
257 ^o K	29.2	1.6	2.4*
242	29.8	1.7	5.0
223	30.2	2.1	3.0
134	32.8	3.0	3.6

M_b	$\Delta G^{\gamma \rightarrow \alpha}(M_b, C_{M_b})$	$\delta \Delta G^{**}$	$\Delta G^{\gamma \rightarrow \alpha}(M_b, C_{max}^{gr})$
257	-302 cal/mole	58 cal/mole	-215*cal/mole
242	-298	62	-116
223	-306	77	-196
134	-286	112	-152

* Ran off edge of specimen, composition should be higher,
and driving force less negative.

** Calculated by multiplication of $(C_{max}^{rn} - C_{M_b}) \times \partial \Delta G / \partial C$.

Values of $\partial \Delta G / \partial C$

M_b	to calculate $\delta \Delta G$	to calculate $\Delta G(M_b, C_{max}^{gr})$
257	36.2 cal/mole/w/o Ni	36.3 cal/mole/w/o Ni
242	36.4	36.6
223	36.5	36.6
134	37.2	37.2

is proper. Physically, it is difficult to envision why the minimum driving force for growth should drop so suddenly over such a limited range.

Table 8 shows that $\delta\Delta G$ increases and $\Delta G^{\gamma\rightarrow\alpha'}$ at T_{\max}^{gr} decreases with decreasing temperature or increasing nickel content. The increase in $\delta\Delta G$ can be rationalized by considering the increase in flow stress with decreasing temperature. Data from Bolling and Richman⁽⁷⁴⁾ for Fe-32w/o Ni show that the flow stress ratio $(\sigma_y^{220}/\sigma_y^{260}) \approx 1.25$, while here the ratio of $(\delta\Delta G^{220}/\delta\Delta G^{260}) = 1.32$. The agreement between these two ratios is quite good, considering the errors involved in determining $\delta\Delta G$.

Disregarding the anomalous value for 242° K, as previously noted, the value of $\Delta G^{\gamma\rightarrow\alpha'}(T_{\max}^{\text{gr}})$ decreases with decreasing temperature. Two contributions to $\Delta G^{\gamma\rightarrow\alpha'}(T_{\max}^{\text{gr}})$ are considered in a later section, and both terms (interfacial drag and elastic accommodation energy) are proportional to the shear modulus. In ferromagnetic austenites, the shear modulus decreases with decreasing temperature. Interpolating from data of Hausch and Warlimont,⁽⁷²⁾ the shear modulus of Fe-31Ni at 273° K is about 6.5×10^4 MPa; that for Fe-37Ni at 134° K is about 5.15×10^4 MPa. The ratio of these two values (1.26), compares well with the ratio of $\Delta G^{\gamma\rightarrow\alpha'}(31 \text{ Ni}, 276^\circ \text{ K})/\Delta G^{\gamma\rightarrow\alpha'}(37 \text{ Ni}, 134^\circ \text{ K}) = 1.43$. Since the theoretical value obtained for $\Delta G^{\gamma\rightarrow\alpha'}(T_{\max}^{\text{gr}})$ was an underestimate it is quite conceivable that some other term not considered could account for the remaining decrease with temperature, if a positive temperature coefficient is postulated.

Another possibility is that the aspect ratio could decrease with decreasing temperature; comparison of the sample transformed at 134° K with the ones at 242° K or 257° K, see Figure 23, suggests that the lower temperature sample has a smaller aspect ratio. Experimental evidence for

this is sketchy. Korenko⁽⁸⁸⁾ found that the aspect ratios for plates in Fe-22.5Ni-4.0Mn transformed under magnetic fields at liquid nitrogen temperature were smaller than for samples transformed at a higher temperature. In carbon-containing alloys, there is a definite trend toward thin-plate martensite as the transformation temperature is lowered.⁽⁸⁹⁾

In summary, both temperature gradient and composition gradient data seem compatible, with their values scaling approximately as predicted by temperature and composition dependences of the flow stress and elastic shear modulus.

Polycrystalline Results

Single crystals afford experimental convenience in studying the basic processes occurring within a grain. Practical materials are almost invariably polycrystalline, and so it is natural to extend the temperature-gradient technique to polycrystalline materials.

Grain boundaries are usually considered as barriers to martensitic growth. Hence, it was of interest to see if propagation of the martensitic reaction up a temperature gradient containing varying numbers of grain boundaries could be accomplished. Additionally, comparison with the results for the single crystals should indicate whether a different nucleation controlling process might be active in the presence of grain boundaries.

A direct comparison between the single and polycrystalline nil-carbon alloys (2 & 4) indicates that the autocatalytic energy-assist for the single crystal is indeed appreciably higher (by a factor of about 1.4) as shown by the data in Table 3. Comparison of the carbon-containing alloys (1 & 3) is not unequivocal; however, the trend is similar, and one is led to the

conclusion that a different process is controlling.

We must now consider how the presence of grain boundaries might affect the processes of nucleation. In terms of the stress assistance of pre-existing nucleation sites, two possible effects present themselves. The first, an orientation affect, allows the possible rotation between grains to change the coupling factors from those calculated within a grain to somewhat different values. It is conceivable that, instead of a maximum coupling of 0.9092, a value of 1.0 could be achieved. On the aggregate, however, this probably would be of minimal effect, since the frequency of these best-possibly-coupled grains would be too low.

Secondly, there is a partitioning effect. Because dispersive interaction of stress waves with boundaries takes place, it seems likely that only the local stress field around a plate would affect nucleation sites, and the value of this stress at a distance may be lower than that in the original grain. Thus, the volume of austenite affected by a plate would be on the order of a few times the plate volume, i.e., extending not much farther than the next grain. If the next grain contains a pre-existing nucleation site, then it may be activated, triggering nucleation processes within the second grain. But if the grain size is such that no pre-existing embryo exists in the next grain, some other mechanism of grain-boundary crossing would be necessary to initiate martensite in the adjacent grain.

It is likely that a martensitic plate stopping at an "opaque" grain boundary would induce deformation in the next grain. This would seem to suggest that stress-assisted strain-induced autocatalytic nucleation should occur across grain boundaries as well as within grains. That it does not,

or does so less efficiently (comparing $\delta\Delta G^{\text{polyxtal}}$ vs. $\delta\Delta G^{\text{monoxstal}}$) may arise because of the following. As a martensitic plate grows within a grain, the volume of austenite next to it is subjected to an almost homogeneous strain field, and the conditions for producing an array of dislocations with appropriate configuration can be met over a relatively large volume. In the case of grain-boundary impingement, these conditions are fulfilled only locally, and so the probability of achieving autocatalytic nucleation drops. An alternative view is that the production of new nucleation sites occurs, but their potency in the presence of grain boundaries may be lower.

The effect of grain size helps decide between these two possibilities. The pre-existing embryo density is unaffected by grain boundaries;⁽⁵⁾ hence, the probability of triggering a site within a grain is proportional to the volume per grain. The extent of nucleation up the gradient will be decided by the point where the product of the density of sites times volume per grain drops to a small enough number. From the experiments of Cech and Turnbull,⁽²⁾ and the subsequent analysis of their data by Olson and Cohen,⁽¹¹⁾ one can obtain information about ρ (the density of pre-existing sites) vs. temperature; and from the measured grain size of the polycrystalline alloys, one obtains the grain volume \bar{V} . By modifying the ρ vs. T results to reflect the added driving force due to elastic stress around a given martensitic plate, one can plot the $\rho\bar{V}$ product vs. grain size, and compare it with the $\Delta T(= T_{\text{max}}^{\text{rn}} - M_b)$ vs. grain size data for alloy 4.

At M_b , ρ is approximately $10^6/\text{cm}^3$; for every 50°C decrease below M_b , ρ increases by about an order of magnitude. Assuming that about 35 cal/mole of energy can be supplied by the elastic stresses, the density of

embryos at $M_b + 35^\circ$ (ΔG changes by about 1 cal/mole (4.2 J/mole) per 1°C) would be about the same as at M_b without stress, though not all of these nuclei would be correctly oriented. The correction factor for orientation is in the range of 1/4 to 1/6, inasmuch as only about 4-6 variants of the 24 have large positive coupling factors. Values of $0.2 \bar{\rho}\bar{V}$ are as follows (assuming applied stress is acting):

Grain size: (in microns)	10	20	50	100	200
$\bar{V} \text{ (cm}^3\text{)}$	5.2×10^{-10}	4.2×10^{-9}	6.5×10^{-8}	5.2×10^{-7}	4.2×10^{-6}
$\rho(M_b) \text{ (\#/cm}^3\text{)}$	5×10^6				
$\rho(M_b) \times \bar{V}/5^{**}$	5.2×10^{-4}	4.2×10^{-3}	6.5×10^{-2}	5.2×10^{-1}	4.2×10^0
$\rho(M_b + 17.5)$	2.3×10^6				
$\rho(M_b + 17.5) \times \bar{V}/5^{**}$	2.4×10^{-4}	1.9×10^{-3}	3.0×10^{-2}	2.4×10^{-1}	1.9×10^0
$\rho(M_b + 35)$	10^6				
$\rho(M_b + 35) \bar{V}/5^{**}$	1.0×10^{-4}	0.8×10^{-3}	1.3×10^{-2}	1.0×10^{-1}	0.8×10^0

**These are the effective densities of embryos at the temperature noted per grain, or, the probability of nucleation within that grain at the temperature noted.

The comparison made with the alloy 4 data (Figure 37) indicates that the probabilities (the figures plotted on the graph) at the edge of the increasing part of the data envelope do not remain very constant. The slope of the data envelope is much less than lines of calculated equal probability ($\bar{\rho}\bar{V}/5 = \text{constant}$). The calculated values seem rather low also.

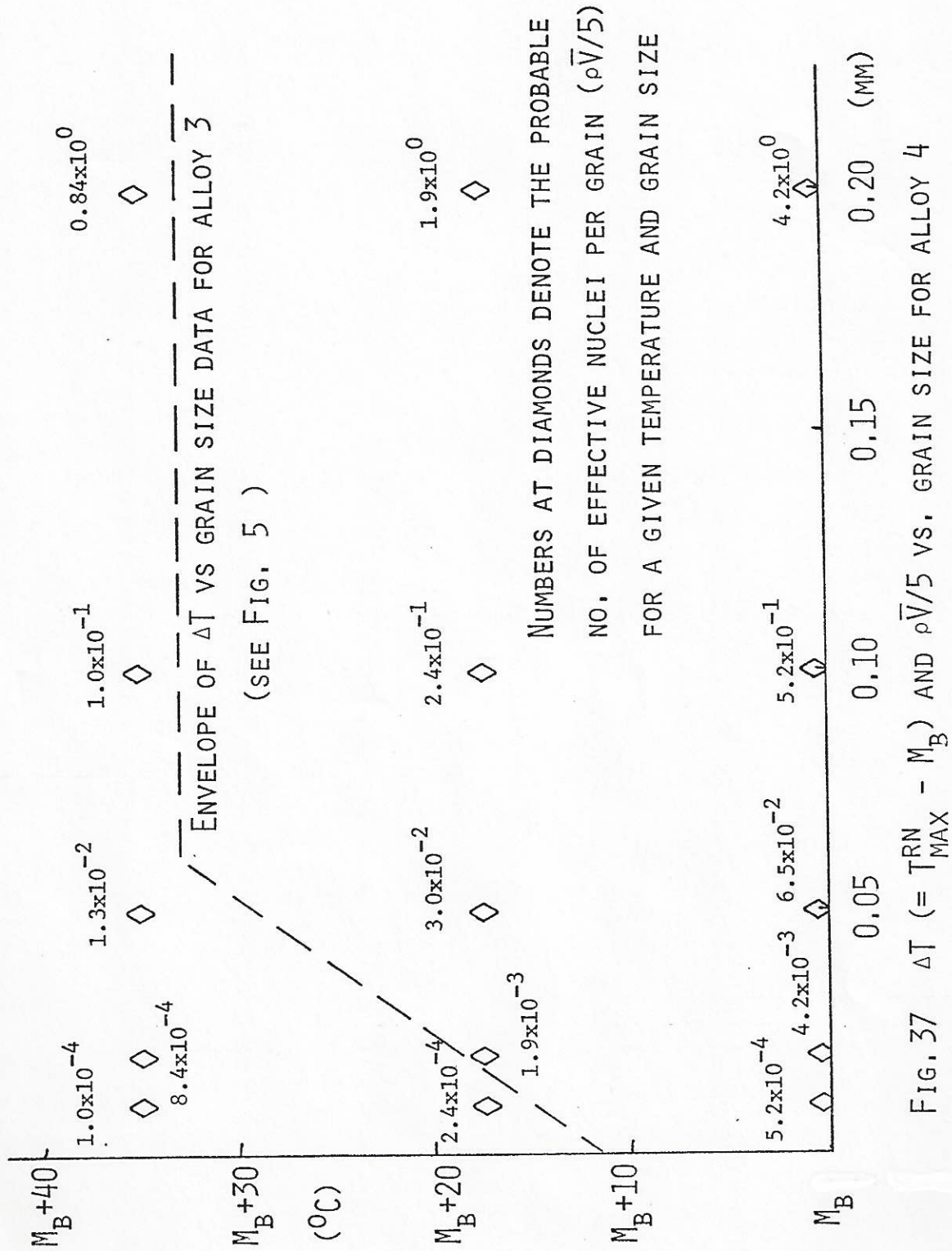


FIG. 37 ΔT ($= T_{MAX}^{RN} - M_B$) AND $\rho\bar{V}/5$ VS. GRAIN SIZE FOR ALLOY 4

These factors may suggest that, instead of the density times volume, a better correlation would be with density times grain-boundary area (which would yield calculated lines of equal probability of lower slope vs. grain size), and also that the number of nucleation sites is higher than that provided by pre-existing ones. Both factors indicate that the hypothesis of strain-induced stress-assisted autocatalysis across grain boundaries is more correct than the simple stress activation of pre-existing sites.

In summation, autocatalysis between grains appears to be less effective than autocatalysis within a grain; it also seems to be an inherently statistical phenomenon. The latter characteristic is reflected in two ways; first, greater scatter is found in the polycrystalline data for ΔT , and second, as the number of grain boundaries to be crossed increases (in small-grained samples) the effectiveness of the autocatalytic process decreases.

Implications of the Minimum Driving Force for Growth

Krisement, Houdrement, and Wever⁽⁵⁹⁾ suggested that the adiabatic-heating phenomenon (temperature recalescence) could become the criterion for M_s . They reasoned that the energy released by the phase transformation minus the work term of accommodation (w) would serve to adiabatically heat the martensite, and that the chemical driving force at the temperature reached by adiabatic heating should equal a threshold value equal to the accommodation work (w). However, in evaluating this work term, they assumed that conditions of thermodynamic reversibility existed at the temperature reached adiabatically. There is no a priori reason to make this assumption. Consequently, the value of w they calculated can be shown to be off

by the difference between their adiabatic temperature and the equilibrium temperature, multiplied by $\Delta S^2/C_p$, where C_p is the molar specific heat and ΔS is the entropy change per mole.

Hillert⁽⁹⁰⁾ later treated the same problem and pointed out the assumption that $w = -\Delta G^{\gamma \rightarrow \alpha}$ was unjustified. By setting up a pair of simultaneous equations for the values of $\Delta U^{\gamma \rightarrow \alpha'}$ and $\Delta S^{\gamma \rightarrow \alpha'}$, stating conservation of energy and that $\Delta S = 0$, he showed that the adiabatic temperature and reaction-start temperature could be calculated in terms of $\Delta U^{\gamma \rightarrow \alpha'}$, $\Delta S^{\gamma \rightarrow \alpha'}$, and the specific heat C_p . He then calculated the equilibrium temperature for the reaction under isothermal conditions (T_i), which turned out identical to the adiabatic temperature of Krisement et al. This is not surprising because the assumption of Krisement et al. that $-\Delta G^{\gamma \rightarrow \alpha'} = w$ means that equilibrium conditions obtain by definition.

For the special case of deformation-induced martensite, Hillert suggested that $w = 0$; under this condition it is correct to equate T_i with T_0 as defined by Kaufman et al.⁽³²⁾ He then calculated the remaining hysteresis predicted by the adiabatic hypothesis, and found good agreement with experiment. Setting $w = 0$ is equivalent to assuming that the maximum driving force due to mechanical work is equal to the accommodation work in forming a plate. Why these two should be equal is not obvious. Even with this assumption, the condition that $w = 0$ means that all the accommodation work is provided by plastic deformation; therefore, it also implies that the rate of martensite formation must be limited by the rate of deformation. The deformation experiments of Kaufman⁽⁹¹⁾ which produced the experimental hysteresis value were not conducted adiabatically; for that reason it seems unlikely that the adiabatic hypothesis is applicable.

Both Krisement et al. and Hillert seem to be treating M_s as a growth-controlled limit, rather than as a nucleation limit. It seems unlikely that such an approach, which neglects the effects of surface energy, would be successful in treating a nucleation problem. However, applying the concept of thermodynamic equilibrium to the process of growth may seem reasonable, and the measurement of the maximum temperature of growth accomplished in this work makes a correct application of this hypothesis plausible.

A real question as to the validity of the adiabatic assumption arises, however. When the growth comes to a halt, does it do so abruptly, or in a gradual slowing-down manner? If it does so gradually, isothermal conditions may apply, and the $\Delta G^{\gamma \rightarrow \alpha'}(T_{\max}^{\text{gr}})$ becomes a direct measure of the work term. This yields values of about 220 cal/mole (920 J/mole) for Fe-31 Ni. See Table 3. On the other hand, if the adiabatic hypothesis is accurate, a value of less than about 100 cal/mole (420 J/mole) is more nearly correct (see Figure 38).

In polycrystals, where grain boundaries exist as definite barriers, there does not seem to be any question but that the martensite growth arrest takes place under adiabatic conditions. In single crystals, on the other hand, it is quite possible that the plate may be able to slow down and come to an isothermal halt. Experimentally, the burst reaction in the temperature gradient specimens takes place too fast for the eye to follow; in most cases, the point where the reaction stops is not within the field of view anyhow. Furthermore, slow growth on a microscale might not be observable. Finally, slow growth has been observed in some Fe-Ni alloys,⁽⁹²⁾ though it has been attributed to surface martensite;⁽²³⁾ surface observations cannot

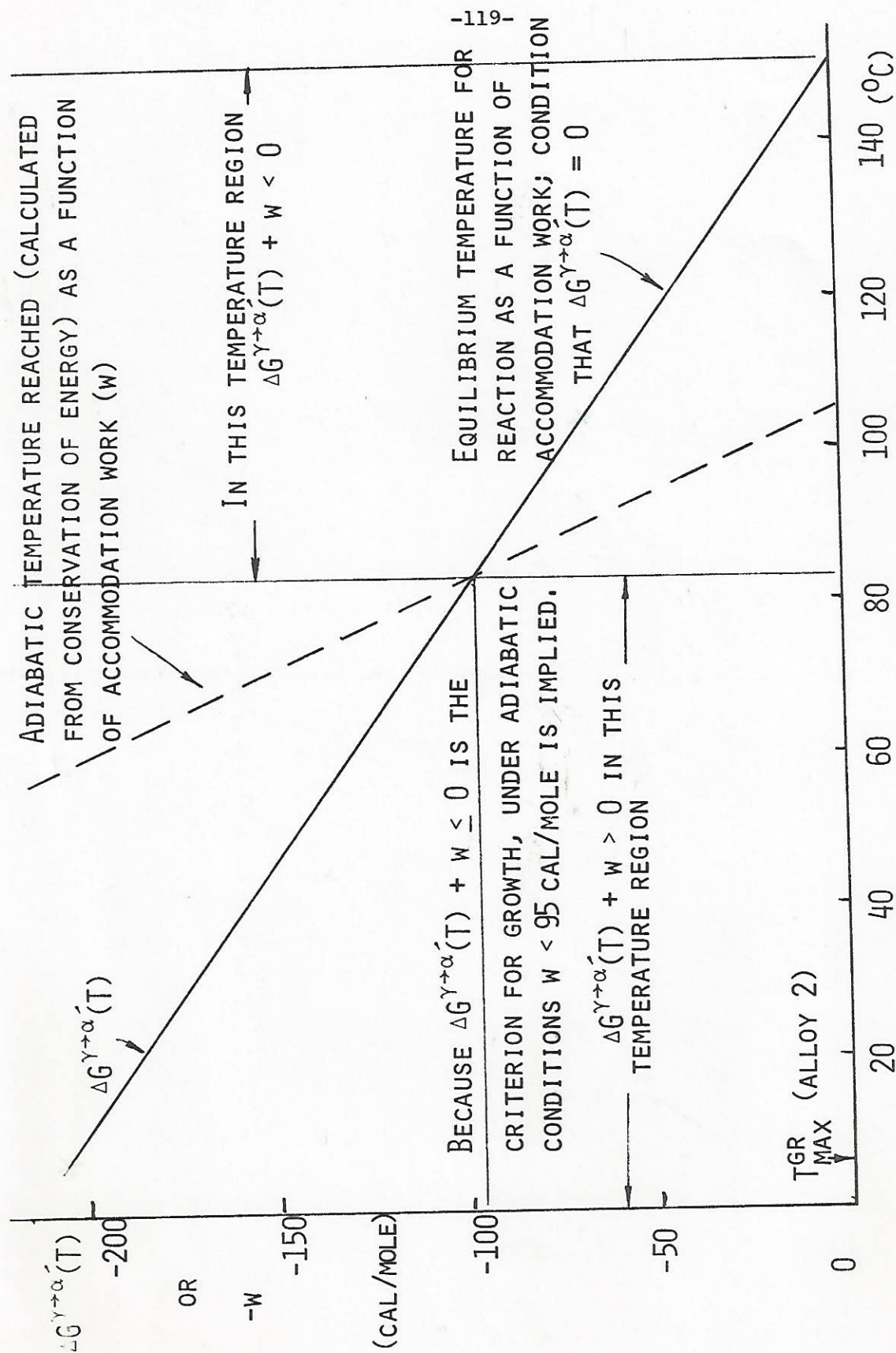


FIG. 38 APPROXIMATION TO DETERMINE THE MINIMUM DRIVING FORCE FOR GROWTH UNDER ADIABATIC CONDITIONS

always be taken as representative of bulk properties.

To decide between the two possibilities, we have only the actual magnitude of $\Delta G^{\gamma \rightarrow \alpha'}(T_{\max}^{\text{gr}})$ to go on, about 220 cal/mole, as noted in Table 3.

Slow growth of interfaces in bulk samples is observed unambiguously in one class of martensitic alloys; those exhibiting single-interface reversibility. Recently, the thermodynamic driving force necessary to make such an interface propagate has been measured in Cu-14Al-3Ni,⁽⁹³⁾ and can be taken as the intrinsic drag force that such an interface experiences under isothermal conditions, where no elastic accommodation work is present. If this value for Cu-Al-Ni can be scaled to Fe-31 Ni, and a term for the accommodation work added, their sum should yield an estimate for an isothermal $\Delta G^{\gamma \rightarrow \alpha'}(T_{\max}^{\text{gr}})$.

Friction stresses on dislocations are calculated as a fraction of the shear modulus;⁽⁹⁴⁾ it thus seems appropriate to scale the Cu-Al-Ni value by the ratio of the shear moduli. Moreover, since the transformation strain of Fe-31Ni is greater (0.226 vs. 0.096), it also seems reasonable to scale the Cu-Al-Ni value by the ratio of transformation strains as well. (Twice the shear angle implies twice the density of dislocations in the interface, hence twice the energy is required to move the interface a given distance.) The value for the minimum driving force due to drag is 5.7 cal/mole (23.8 J/mole) in Cu-14Al-3Ni; applying the above two correction factors raises it to about 45 cal/mole (188 J/mole) for Fe-31Ni.

Neglecting the strain energy due to volume expansion, the accommodation energy (per unit volume of martensite in an infinite matrix) is given by the equation:⁽⁹⁵⁾

$$E_v^\infty = \frac{\mu\pi(2-\nu)c}{8(1-\nu)a} \gamma^2 \quad (5.4)$$

Choosing a value of c/a equal to 2×10^{-2} (the steady-state aspect ratio as calculated by Raghavan and Cohen⁽⁹⁶⁾), and setting $\nu = 1/3$, $\gamma = 0.2$, and $\mu = 6.5 \times 10^4$ MPa yields a value of about 85 cal/mole (356 J/mole).

Summation of the accommodation energy and the drag energy provides an estimate of the minimum driving force for growth under isothermal conditions in Fe-31Ni equal to 130 cal/mole (544 J/mole).

To arrive at an estimate of ΔG_{\max}^{gr} under adiabatic conditions one must modify somewhat the above values.

First, the aspect ratio should be that of the midrib only; as a consequence c/a will be smaller by at least an order of magnitude, and the elastic accommodation energy will become negligible.

Secondly, by analogy to dislocation drag forces, the interfacial drag term should increase according to the strain-rate sensitivity of the lattice. This has previously been shown to be very small for lattice dislocations in fcc Fe-31Ni. Transformation dislocations are a somewhat special case, however, and they show behavior intermediate between fcc and bcc. Shock deformation of bcc structures has produced yield stresses which are several times those of static-deformed specimens.⁽⁹⁷⁾ It is conceivable, therefore, that the drag force on the interface could increase from a static value of 45 cal/mole (188 J/mole) to a higher value. Unfortunately, assigning a numerical value is impossible at this stage.

Accordingly, these considerations do not allow one to choose unambiguously between the adiabatic and isothermal hypotheses. Both analyses are underestimates. In the isothermal calculation, the c/a ratio plays an

important role; the value chosen is a theoretically-predicted one, and indeed the experimentally-determined values are about twice as large.

Using a value of $c/a = 4 \times 10^{-2(5)}$ would yield an overall value of $\Delta G^{\gamma \rightarrow \alpha}(T_{\max}^{\text{gr}})$ equal to 215 cal/mole (900 J/mole).

Without relying upon structural inhomogeneities which would act to stop the advancing interface abruptly (and which would probably yield a much larger scatter in the T_{\max}^{gr} values than was observed), it is the opinion of the author that a gradual halt is physically more probable. Thus, the isothermal value is more likely to be correct.

One final observation worth noting is that the maximum temperature of growth correlates well with the observed morphological transition between plate-type and stringer-type deformation-induced martensites.⁽³³⁾ One explanation could be that the stringer-type martensites cannot grow beyond the slip bands where they are nucleated because the chemical driving force is insufficient for growth. (If the accommodation work for the transformation is being provided by the external deformation, it would not be available outside of the shear bands, where the stringer-type martensite is only observed.)

CHAPTER VI

CONCLUSIONS

1. The mechanism of autocatalysis in martensitic burst transformations in Fe-Ni single-crystal alloys is due to the stress-assisted nucleation of strain-induced high potency nuclei produced by the accommodation deformation of an initial plate of martensite. No evidence has been found to confirm the interfacial mechanism proposed by Olson and Cohen; this mechanism may be inhibited by local adiabatic heating effects.

2. In polycrystals, the process of spreading across grain boundaries also involves a strain-induced production of nuclei; but the process is less efficient than in single crystals. It is by nature a statistical phenomenon; the more grain boundaries to cross, the less likely the spreading mechanism becomes.

3. Composition-gradient and temperature-gradient experiments are in substantial agreement on the values measured for the energy-assist in autocatalytic nucleation and the minimum driving force for martensitic growth.

4. The variation of the autocatalytic assist appears to correlate well with the compositional and temperature dependence of the yield stress; while the minimum driving force for growth correlates with the temperature and composition dependencies of the elastic modulus.

5. A set of necessary conditions are proposed for the occurrence of efficient autocatalysis in martensitic transformations.

6. The martensitic burst temperature does not seem to be a function of either grain size or austenitizing temperature if spurious chemical changes are avoided. (See Appendix III).

CHAPTER VII

SUGGESTIONS FOR FURTHER RESEARCH

1. This work should be extended to other martensitic systems which exhibit burst tendencies, and also to non-bursting alloy systems.
2. Measurement of the minimum driving force for growth should be carried out in other alloy systems, and experimental resolution of the question of isothermal vs. adiabatic growth arrest should be attempted.
3. An electron microscope study of the dislocation arrangements near the martensitic plates in regions where $T_{\max}^{\text{rn}} < T < T_{\max}^{\text{gr}}$, to characterize the dislocation arrays produced by accommodation may prove significant.
4. A study introducing well-characterized grain boundaries within the temperature gradient would serve to clarify the mechanism of grain-boundary crossing by autocatalysis. This could be combined advantageously with the study mentioned in 3.
5. Thermodynamic driving-force equations for the ternary Fe-Ni-C system require further refinement.
6. Use of the gradient technique may provide an effective trigger for high-speed photography techniques. This kind of investigation might yield autocatalytic-plate sequence data, as opposed to the motif data obtained in this thesis.

APPENDIX I

AUTOCATALYSIS VIA THE STRESS-ASSISTED STRAIN-INDUCED NUCLEI MECHANISM

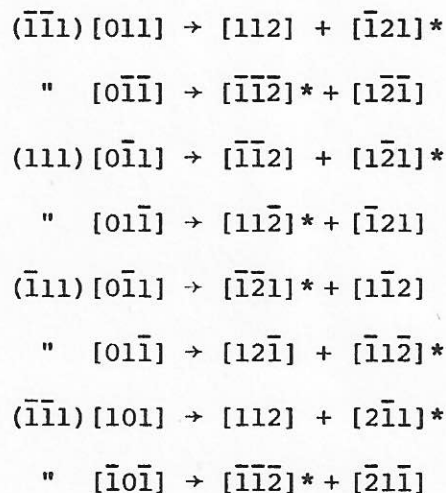
Starting with a (3 10 15) habit, the independent slip systems acted upon by the highest shear stresses and their Schmid factors are:

$(\bar{1}\bar{1}1)[011]$	0.883
$(111)[0\bar{1}1]$	0.795
$(\bar{1}11)[0\bar{1}1]$	0.668
$(\bar{1}\bar{1}1)[101]$	0.657
$(1\bar{1}1)[011]^*$	0.580
$(\bar{1}11)[\bar{1}\bar{1}0]**$	0.498

*This system is not independent; it will be disregarded.

**This system is independent, but its Schmid factor is relatively low; it, too, will be disregarded.

These perfect dislocations can then dissociate: (into intrinsic faults)



The asterisked partials are twinning type (as opposed to anti-twinning), and can act as possible first-shear dislocation elements for the Olson-Cohen theory, if they are properly stacked.

Each partial can result in two possible habit planes, one for each of the two possible second-shear elements that can team with it. If we consider the slip system with the highest coupling factor, the two asterisked partials will provide four potential habit nuclei. The plates which result, and their coupling factor (see Figure 34) with respect to the original (3 10 15) are:

$(\bar{3} \bar{10} 15)$	-0.7984
$(15 10 \bar{3})$	-0.2645
$(\bar{3} \bar{15} 10)$	+0.9092
$(\bar{15} \bar{3} 10)$	+0.4981

Of these, then, the most likely to trigger is $(\bar{3} \bar{15} 10)$. Assuming that it does trigger, the coupling factors between $(\bar{3} \bar{15} 10)$ and the remaining nuclei produced by (3 10 15) using the chosen slip system are:

$(\bar{3} \bar{10} 15)$	+0.6751
$(15 10 \bar{3})$	+0.2827
$(\bar{15} \bar{3} 10)$	-0.4395

Thus, if the growing $(\bar{3} \bar{15} 10)$ plate passes nearby to one of the $(\bar{3} \bar{10} 15)$ nuclei created by the original plate, the latter nucleus is likely to be triggered also. If this sequence (where a first plate creates the nuclei for a second and third plate, and simultaneously triggers the second plate, which in turn activates the third habit variant) continues, each triggered plate will re-initiate the whole process, and the eight habit variants about the two [110] type directions perpendicular to the [100] axis will eventually all be produced. See Figure 27 where the plates involved in the basic sequence are noted A, A', B'.

Repeating the same process for the next three slip systems with successively lower Schmid factors leads to two other cycles:

When the $(111)[0\bar{1}1]$ system is chosen, the nuclei for these four potential habits (and their coupling factors) are:

(3 10 15)	-1.000
(15 10 3)	-0.4395
(3 15 10)	+0.6751
(15 3 10)	+0.2827

This tabulation suggests that (3 15 10) will be activated. The coupling factors between (3 15 10) and the remaining nuclei are:

(3 10 15)	+0.6751
(15 10 3)	+0.2827
(15 3 10)	+0.2827

Hence, (3 10 15) should be triggered, and this leads to a short cycle linking only (3 10 15) and (3 15 10).

For the system $(\bar{1}11)[0\bar{1}1]$ the appropriate habits and coupling factors are:

$(\bar{3} 10 15)$	-0.8493
$(\bar{1}\bar{5} 10 3)$	-0.2645
$(\bar{1}\bar{5} 3 10)$	+0.3936
$(\bar{3} 15 10)$	+0.7770

Accordingly, $(\bar{3} 15 10)$ should be activated, which then couples to the remaining nuclei:

$(\bar{3} 10 15)$	+0.6751
$(\bar{1}\bar{5} 10 3)$	+0.2827
$(\bar{1}\bar{5} 3 10)$	-0.4395

This step triggers $(\bar{3} \ 10 \ 15)$. Using symmetry arguments, it can be seen that a $(3 \ 10 \ 15) \rightarrow (\bar{3} \ 15 \ 10) \rightarrow (\bar{3} \ 10 \ 15) \rightarrow (3 \ 15 \ 10)$ cycle (noted in Figure 26 as A, B, C, D respectively) containing just four habit variants is produced.

For the system $(\bar{1}\bar{1}1)[101]$ the habits and coupling factors are:

$(10 \ 3 \ \bar{1}5)$	-0.5633
$(10 \ 15 \ \bar{3})$	+0.3936
$(\bar{3} \ \bar{1}5 \ 10)$	+0.9092
$(\bar{1}5 \ \bar{3} \ 10)$	+0.4981

$(\bar{3} \ \bar{1}5 \ 10)$ triggers, but couples to the remaining nuclei very poorly:

$(10 \ 3 \ \bar{1}5)$	+0.2827
$(10 \ 15 \ \bar{3})$	-0.6712
$(\bar{1}5 \ \bar{3} \ 10)$	+0.2827

Hence, this system leads to no new cyclic behavior.

Exactly the same type of analysis can be applied to the case of $(2 \ 2 \ 5)$ martensite, with the exception that a new set of coupling factors between plates, and a new set of Schmid factors must be calculated. These are listed in Figure 33, and in the table below, respectively.

$(\bar{1}\bar{1}1)[101]$	0.7860
$(\bar{1}\bar{1}1)[0\bar{1}\bar{1}]$	0.7642
$(111)[01\bar{1}]$	0.7285
$(1\bar{1}\bar{1})[01\bar{1}]^{**}$	0.4833
$(\bar{1}\bar{1}\bar{1})[\bar{1}01]^*$	0.4615
$(1\bar{1}\bar{1})[\bar{1}\bar{1}0]^{**}$	0.4174

*This system is not independent; it will be disregarded.

**These systems are independent, but their Schmid factors are relatively

low; they, too, will be disregarded.

For the (2 2 5) habit planes, the dislocation elements are identical to those in the (3 10 15) case, for the habits corresponding to the same unit triangle of the stereographic projection. The difference in habit arises from the differing lattice-invariant shear chosen later on in the growth process.

The identical procedure is then followed to decide which habits are produced by the stress-assisted strain-induced mechanism.

Because the (2 2 5) habit lies right on the boundary of the unit triangle, it and its twin related habit are not distinguishable by only the habit plane; however, the two shear directions are distinguishable. For this reason the 2+, 2- notation is introduced to make this distinction. Refer to Figure 33 to see which habit is being discussed.

For the slip system $(\bar{1}\bar{1}1)[101]$, the habits resulting from the initial plate (2- 2+ 5) are:

$(\bar{2}- \bar{5} 2+)$	+0.7756
$(\bar{5} \bar{2}- 2+)$	+0.4883
$(\bar{2}+ \bar{2}- 5)$	-0.5505
$(\bar{2}+ \bar{5} 2-)$	+0.0957

$(\bar{2}- \bar{5} 2+)$ is triggered and couples with the remaining habits:

$(\bar{5} \bar{2}- 2+)$	-0.4762
$(\bar{2}+ \bar{2}- 5)$	+0.0134
$(\bar{2}+ \bar{5} 2-)$	-0.6450

The resulting coupling factors are small, and so none of these is triggered.

For the slip system $(\bar{1}\bar{1}1)[0\bar{1}\bar{1}]$, the resulting habits and coupling factors with the initial plate are:

$(\bar{2}- \bar{2}+ 5)$	-0.4037
$(\bar{5} \bar{2}+ 2-)$	-0.0447
$(\bar{2}- \bar{5} 2+)$	+0.7756
$(\bar{5} \bar{2}- 2+)$	+0.4883

Again, $(\bar{2}- \bar{5} 2+)$ is triggered. It couples with the remaining nuclei as follows:

$(\bar{2}- \bar{2}+ 5)$	+0.1624
$(\bar{5} \bar{2}+ 2-)$	+0.0134
$(\bar{5} \bar{2}- 2+)$	-0.4762

None of these would be triggered.

For the slip system $(111)[0\bar{1}\bar{1}]$, the resulting habits and coupling factors with the initial plate are:

$(2- 2+ 5)$	-1.000
$(5 2+ 2-)$	-0.4762
$(2- 5 2+)$	+0.1624
$(5 2- 2+)$	+0.0134

None of these would be expected to be triggered.

Thus, only one cyclic pattern (A,A!C!C) is predicted, and this is shown in Figure 27.

Thus, since there are far fewer possibilities for autocatalytic nucleation via the mechanism discussed in this chapter, it is not surprising that the burst tendencies of (2 2 5) habit martensites are sharply reduced when compared with (3 10 15) habit martensites.

APPENDIX II

INTERFACIAL RENUCLEATION MODEL

Starting with a (3 10 15) habit, which uses:

first-shear	second-shear	"edge"	"screw"
(111) [1 $\bar{2}$ 1]	($\bar{1}\bar{1}$ 1) [$\bar{1}$ 21]	($\bar{1}\bar{1}$ 1) [$\bar{1}\bar{1}$ 2]	(111) [1 $\bar{1}$ 0]

If the second-shear is to act as a potential first-shear for an autocatalytic variant, this would lead to nucleation of the following variants (refer to Table 5), and their coupling factors:

($\bar{3}$ $\bar{1}$ 0 15)	-0.7984
($\bar{1}$ 5 $\bar{1}$ 0 3)	-0.2645

Relying upon the possible large "n" with this mechanism ($\bar{1}$ 5 $\bar{1}$ 0 3) is more likely to be nucleated because of less hindrance from the original plate's stress field.

The second-shear of ($\bar{1}$ 5 $\bar{1}$ 0 3) (found in Table 5) would lead to the following variants and coupling factors (with ($\bar{1}$ 5 $\bar{1}$ 0 3)):

(3 $\bar{1}$ 0 15)	-0.2645
(15 10 3)	-0.7984

(3 $\bar{1}$ 0 15) is more likely; the second-shear of this habit leads to either:

($\bar{3}$ 10 15)	-0.7984
($\bar{1}$ 5 10 3)	-0.2645

It can be shown similarly that the second-shear of ($\bar{1}$ 5 10 3) will lead to (3 10 15), with a coupling factor of -0.2645. This leads to a cyclic behavior given by:

$$\begin{array}{ccccccc} (3 \ 10 \ 15) & \rightarrow & (\bar{1}5 \ \bar{1}0 \ 3) & \rightarrow & (3 \ \bar{1}0 \ 15) & \rightarrow & (\bar{1}5 \ 10 \ 3) \text{--} \\ & & \uparrow & & & & \downarrow \\ & & \hline & & & & \end{array}$$

This is plotted stereographically in Figure 29.

Another possibility of the interfacial model is that either the "edge" or "screw" dislocations in the interface can act as first-shears for another plate (as noted in Chapter 5, they are not of the correct stacking density).

The "edge" case, again starting with (3 10 15), leads to the following variants and coupling factors:

$$(\bar{3} \bar{1} \bar{5} 10) \quad +0.9092$$

$$(\bar{1} \bar{5} \bar{3} 10) \quad +0.4981$$

Choosing ($\bar{3} \bar{1} \bar{5} 10$) as having nucleated, this leads to:

$$(\bar{3} 10 15) \quad +0.9092$$

$$(\bar{1} \bar{5} 10 3) \quad +0.4981$$

Choosing ($\bar{3} 10 15$) as having nucleated, this leads to:

$$(15 \bar{3} 10) \quad +0.4981$$

$$(3 \bar{1} \bar{5} 10) \quad +0.9092$$

Choosing (3 $\bar{1} \bar{5} 10$) as having nucleated, this leads to:

$$(3 10 15) \quad +0.9092$$

$$(15 10 3) \quad +0.4981$$

which leads to the cyclic process:

$$\begin{array}{ccccccc} (3 \ 10 \ 15) & \rightarrow & (\bar{3} \ \bar{1} \bar{5} \ 10) & \rightarrow & (\bar{3} \ 10 \ 15) & \rightarrow & (3 \ \bar{1} \bar{5} \ 10) & \rightarrow \\ \uparrow & & & & & & & \downarrow \\ \hline \end{array}$$

This is plotted stereographically in Figure 30.

For the "screw" case, the perfect dislocation can dissociate in either the first-shear plane or the second-shear plane.

If it does so on the second shear plane, starting again with (3 10 15):

$$(\bar{1} \bar{1} 1) [1 \bar{1} 0] \rightarrow [1 \bar{2} \bar{1}] + [2 \bar{1} 1]$$

$(\bar{1}\bar{1}1)[2\bar{1}1]$ is the first shear for:

$$(\bar{1}\bar{0} \bar{3} 15) \quad -0.5633$$

$$(\bar{1}\bar{0} \bar{1}\bar{5} 3) \quad +0.3936$$

Choosing $(\bar{1}\bar{0} \bar{1}\bar{5} 3)$ as having nucleated leads to:

$$(\bar{1}\bar{5} 3 10) \quad +0.3936$$

$$(\bar{3} 15 10) \quad -0.5633$$

Choosing $(\bar{1}\bar{5} 3 10)$ as having nucleated leads to:

$$(3 10 15) \quad +0.3936$$

$$(15 10 3) \quad -0.5633$$

which results in the cycle:

$$(3 10 15) \rightarrow (\bar{1}\bar{0} \bar{1}\bar{5} 3) \rightarrow (\bar{1}\bar{5} 3 10) \rightarrow$$

↑ _____ ↓

This is plotted stereographically in Figure 31.

If the dissociation takes place on the first-shear plane:

$$(111)[\bar{1}\bar{1}0] \rightarrow [2\bar{1}\bar{1}] + [1\bar{2}1]$$

$(111)[1\bar{2}1]$ is the first shear for:

$$(3 10 15) \quad -1.000$$

$$(15 10 3) \quad -0.4395$$

This process cannot rely upon a large value of "n" so it is not likely to proceed because both possibilities have negative coupling factors.

Should $(15 10 3)$ nucleate it would produce $(3 10 15)$ again, which is shown on Figure 32.

If the mechanism of this chapter operated, the autocatalytic motifs produced would contain habit variants as noted in Figures 29-32. Such motifs are not evident in the results shown in Chapter 4.

APPENDIX III

MARTENSITIC BURST TEMPERATURE VS. AUSTENITIC GRAIN SIZE

Some controversy exists as to whether the martensitic start (M_s) or martensitic burst (M_b) temperature is influenced by either the austenitizing treatment or the austenitic grain size.

Under conditions where obvious compositional changes occur (i.e., carbides precipitating or dissolving, decarburization, etc.), it is not difficult to understand a functional dependence upon austenitizing temperature for the M_s or M_b . However, in cases where there are no obvious chemical changes, it is less certain that such a dependence exists.

A number of authors have presented data tending to show that M_s or M_b increases with increasing austenitic grain size. Scheil⁽²¹⁾ reported a difference of about 30°C between fine-grained and coarse-grained samples (reported as containing average surface area per grain of much less than 0.01 mm², and of 0.1 mm², respectively). His approach was to produce two large-grained specimens by extensive high-temperature heat treatment (8hr @ 1200°C). One of these specimens he transformed to martensite; the other he deformed and recrystallized at temperatures of 600°, 700°, and 800°C, transforming the specimen to martensite after each such recrystallization step. The M_s of the 600°C sample was 35°C below the M_s of the coarse-grained sample. The M_s temperatures of the 700° and 800° samples were slightly higher, but still well below (at least 20°C) the original M_s . McReynolds,⁽²⁸⁾ with a similar alloy, produced samples of two widely different grain sizes ($\bar{L} = 0.028$ and 0.260 mm), measured their M_s , and then contrived to reverse the grain sizes by recrystallization of the large-grained samples and grain growth of the small-grained samples.

Because the M_s temperatures switched with the grain sizes (small grain size - lower M_s ; large grain size - higher M_s), he concluded that no spurious compositional change took place during the heat treatment. Machlin et al.⁽¹³⁾ also showed that samples of different grain size produced by widely varying austenitizing conditions could produce a lower M_b in samples of finer grain sizes.

All three of the above-mentioned investigators, working with the same alloy system (Fe-29.5 Ni), found that M_s (or M_b) could be depressed by as much as 40°C with decreasing grain size.

Entwisle and Feeney,⁽⁵⁴⁾ in a series of Fe-Ni-C bursting alloys, examined the transformation behavior vs. austenitizing temperature (from 800° to 1200°C), and concluded that austenitizing temperature rather than grain size was the important parameter controlling M_b . Umemoto and Owen,⁽⁹⁸⁾ in a similar but more extensive series of experiments, came to exactly the opposite conclusion, basing their argument on the results obtained from 2-step austenitizing treatments on both an Fe-Ni and Fe-Ni-C alloy.

Maki et al.⁽⁹⁹⁾ have noted that M_s rises spectacularly with austenitizing temperature in similar Fe-Ni-C alloys to that studied by Umemoto et al. M_s changed from below -196°C when austenitized at 800° to about -70°C when austenitized at 1200°C in an Fe-31Ni-0.23 C alloy. In an attempt to discover if decarburization had occurred, they plated some specimens with Ni. When the results of these specimens agreed well with an earlier unplated series, they concluded that decarburization had not taken place.

In summary, the evidence as reported is not self-consistent, but seems to favor the conclusion that M_s or M_b rises with either increasing grain

size or austenitizing temperature. In contrast, the results of the present research indicate that M_b is not a function of either grain size or austenitizing temperature, notwithstanding a variation of grain size over an order of magnitude, and a range of austenitizing temperatures from 800° to 1200°C. How then are the previous results reported in the literature to be rationalized?

First, let us consider the group of results on Fe-Ni specimens. These include the findings of Scheil, McReynolds, Machlin et al., and Umemoto et al.

A possible explanation for the effect of austenitizing temperature on M_b lies in the phenomenon of stabilization by two-phase separation into ferrite and austenite, the latter being of higher Ni content than the overall alloy composition. The evidence for this type of compositional change is provided by experiments measuring M_s from austenite produced by the reversion of martensite. Krauss et al.⁽¹⁰⁰⁾ noted that samples heated rapidly to the A_f temperature do not exhibit a subsequent lower-than-normal M_s whereas samples reheated slowly do. Combining this observation with x-ray determination of austenite lattice parameters, together with resistivity and metallographic data, they showed that M_s is depressed by the prior formation of low-Ni ferrite, thus increasing the remaining austenite in Ni content. Evidence presented by Maksimova et al.,⁽¹⁰¹⁾ and by Golovchiner et al.,⁽¹⁰²⁾ indicates that this effect (though reduced in magnitude) can persist to austenitizing temperatures as high as 900°C, especially when combined with deformation of the sample before re-austenitizing. Presumably, the retention of the M_s depression despite austenitization within the austenitic phase region is a result of the slow dissolution

kinetics of the ferrite formed during slow heating.

In the previously mentioned literature, not all the investigators started with a quenched martensitic structure; however, most started with a cold-worked structure, and in several cases the deformation was carried out below the M_d temperature. It is known that plastic deformation serves to hasten the austenite decomposition to ferrite and austenite in the two-phase region of the Fe-Ni system.⁽¹⁰³⁾ Thus, presence of prior martensite may not be entirely necessary for ferrite separation during the reheating.

At austenitizing temperatures above 900°C, the ferrite should be completely redissolved, yet Umemoto et al. noted that the M_b temperature continued to rise. This might be explained by a surface reaction either due to carbon loss (although these alloys already contained less than 0.01 w/o C, other results have shown that decarburizing from 0.02 to 0.004 w/o C allows an increase in M_s in an Fe-25Ni alloy from 107° to 130°-150°C depending upon cooling rates), or conceivably to silicon contamination from the encapsulation. For example, Yeo⁽¹⁰⁴⁾ has shown that adding up to 1% Si will raise M_s in an Fe 22.5Ni alloy by about 50°C. Experimental evidence obtained in the course of the present work on this confusing effect is suggested by the following: when a number of samples of alloy 4 exhibiting different M_b temperatures and different grain sizes were annealed in a common capsule at 800°C for 1 hour, they all exhibited the same M_b (regardless of grain size) upon subsequent transformation. Previous austenitizing treatments were all above 1000°C for these samples, so any ferrite should have been completely redissolved. The samples were undeformed, and entirely austenitic to start with (the martensite-containing end produced by reacting in the gradient had been removed prior to encapsulation), so no

ferrite was formed upon reheating.

The Fe-Ni-C results seem explainable by less subtle effects. Notwithstanding the attempt to prevent decarburization by Maki et al. by Ni-plating their samples, their reported dramatic rise in M_b as a function of austenitizing temperature (also noted by Umemoto et al. in unplated samples) can largely be explained by decarburization. At temperatures of 1000°C, the solubility of carbon in Ni (about 0.25 w/o) causes the plating to act as a carbon sink, rather than as a protective barrier.

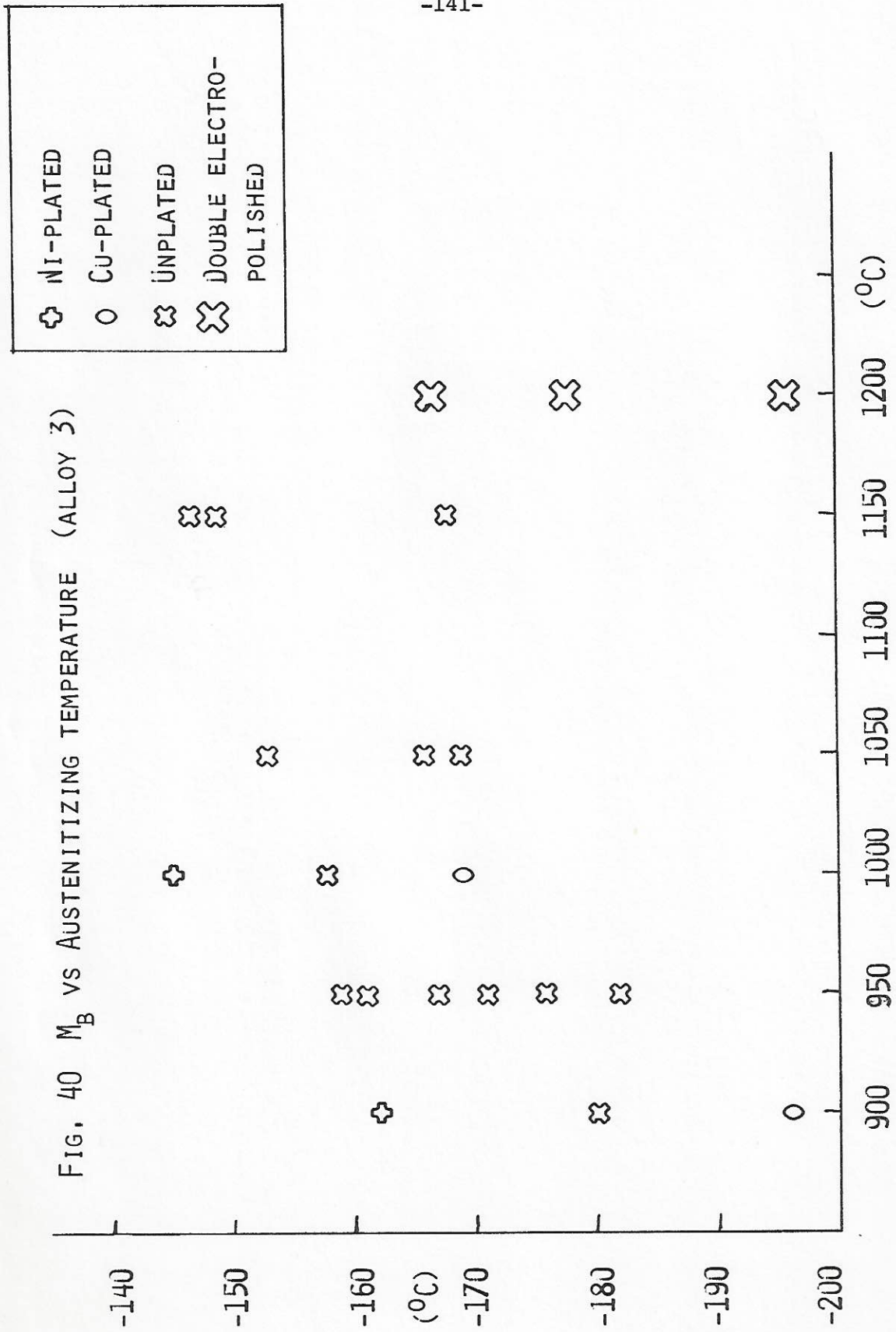
An experiment with three samples having identical thermal histories was carried out in the present study to demonstrate the decarburizing effect. The samples, one Cu-plated, one Ni-plated, and one unplated, were austenitized together at 1000°C for 1 hour. After cooling to the ambient, the plated layers were removed by electropolishing (the unplated sample was also electropolished), and the specimens were then transformed by subcooling. The Cu-plated sample had the lowest M_b (-165°C), and the Ni-plated sample the highest (-145°C). The unplated sample M_b (-158°C) was below that reported by Umemoto et al. for a similar grain size (about -135°C). A difference between this study and that of Umemoto was the use of argon-back-filled encapsulation in this study vs. vacuum encapsulation in the latter.

Experiments were also carried out to test the question of the M_b dependence on grain size or austenitizing temperature in the Fe-Ni-C alloy (alloy 3). As described in Chapter 2, the samples were electropolished after each austenitization treatment in the sequence: 950°C/cool to M_b /1050°C/cool to M_b /1150°C/cool to M_b /950°C/cool to M_b (all heat treatments were for 1 hour). The results of this cycle indicated that M_b was not a

function of grain size over the range of 50 to 150 microns grain size (see Figure 39). However, a slight increase in M_b seemed to be occurring with increasing austenitizing temperature. For this reason, a final cycle at 1200°C was carried out, and at the same time, the amount of material electropolished off after austenitization was doubled. This brought the M_b back down to the level noted after the 950°C cycle (see Figure 40). It was concluded therefore that M_b was not a function of grain size or austenitizing temperature, and that a surface reaction (possibly Ni depletion, or Si pick-up) had occurred as a function of increasing austenitizing temperatures. Because of the high temperatures involved, the diffusion distance of carbon should be much greater than the amount of material removed by the electropolishing; hence it seemed unlikely that the further increase in M_b could be accounted for by carbon depletion. Any gradient in carbon across the thickness removed by electropolishing would be very small, and thus the M_b temperature would not be expected to return to its "normal" value upon electropolishing.

+	NI-PLATED
o	CU-PLATED
⊗	UNPLATED
⊗	DOUBLE ELECTRO- POLISHED





BIBLIOGRAPHY

1. F.C. Frank, NPL Conference on Relations between Structure and Strength in Metals and Alloys, (1963), HMSO London, 248
2. R.E. Cech and D. Turnbull, Trans. A.I.M.E., (1956), 206, 124
3. C.L. Magee, Phase Transformations, ASM, Metals Park, Ohio, (1970), 121
4. S.R. Pati and M. Cohen, Acta Met., (1969), 17, 189
5. S.R. Pati and M. Cohen, Acta Met., (1971), 19, 1329
6. D.G. Mc Murtrie and C.L. Magee, Met Trans., (1970), 1, 3185
7. C.H. Shih, B.L. Averbach and M. Cohen, Trans. A.I.M.E., (1955), 203, 183
8. V. Raghavan and A.R. Entwisle, Iron and Steel Inst. Special Report No. 93, (1965), 30
9. C.L. Magee, Met. Trans., (1971), 2, 2419
10. V. Raghavan and M. Cohen, Met. Trans., (1971), 2, 2409
11. G.B. Olson and M. Cohen, First J.I.M. International Symposium, Kobe, Japan, 1976 (in press)
12. C.L. Magee, Phase Transformations, ASM, Metals Park, Ohio, (1970), 123
13. E.S. Machlin and M. Cohen, Trans. A.I.M.E., (1951), 191, 746
14. R. Brook and A.R. Entwisle, J.I.S.I., (1965), 203, 905
15. P.J. Fisher, Ph. D. Thesis, Univ. of New South Wales, Australia, 1974
16. A.L. Titchener and M.B. Bever, Trans. A.I.M.E., (1954), 200, 303
17. G.V. Kurdjumov and L.G. Khandros, Journal of Technical Physics U.S.S.R., (1949), 19, 761
18. F. Forster and E. Scheil, Zeitschrift fur Metallkunde, (1936), 28, 245
19. F. Forster and E. Scheil, Zeitschrift fur Metallkunde, (1940), 32, 165
20. G. Benediks, J.I.S.I., (1908), 77, 153.

21. E. Scheil, Zeitschrift fur Anorganische und Allgemeine Chemie, (1932), 207, 21
22. E.S. Machlin, Sc. D. Thesis, M.I.T., Cambridge, Ma., 1950
23. J.A. Klosterman, Iron and Steel Inst. Special Report No 93, (1965), 20
24. J.C. Bokros and E.R. Parker, Acta Met., (1963), 11, 1291
25. see for example R.W.K. Honeycombe, The Plastic Deformation of Metals, St. Martens, (1968)
26. A.R. Entwisle, Met. Trans., (1971), 2, (1971), 2395
27. J.R. Patel and M. Cohen, Acta Met., (1953), 1, 531
28. A.W. Mc Reynolds, J. Appl. Phys., (1949), 20, 896
29. S. A. Kulin, M. Cohen and B.L. Averbach, Trans. A.I.M.E., (1952), 194, 661
30. R.H. Richman and G.F. Bolling, Met. Trans., (1971), 2, 2451
31. M.G.H. Wells and D.R.F. West, J.I.S.I., (1962), 200, 710
32. L. Kaufman and M. Cohen, Progress in Metal Physics, (1958), 7, 165
33. P.C. Maxwell, A. Goldberg and J.C. Shyne, Met. Trans., (1974), 5, 1305
34. I. Tamura, T. Maki and H. Hato, Trans. I.S.I. Japan, (1970), 10, 163
35. J.F. Breedis and W.D. Robertson, Acta Met., (1963), 11, 547
36. C.L. Magee, Phase Transformations, ASM, Metals Park, Ohio, (1970), 130
37. G.V. Kurdjumov, Journal of Technical Physics U.S.S.R., (1948), 18, 1011
38. G.B. Olson and M. Cohen, Met. Trans., (in press)
39. F.C. Frank, Acta Met., (1953), 1, 15
40. R. Bullough and B.A. Bilby, Proc. Phys Soc. London B, (1956), 69, 1276
41. W.S. Owen, F.J. Schoen and G.R. Srinivasan, Phase Transformations, ASM, Metals Park, Ohio, (1970), 157

42. H. Warlimont and L. Delaey, Progress in Materials Science, (1974), 18, 103
43. C.M. Wayman, Introduction to the Crystallography of Martensitic Transformations, Macmillan, New York, (1964)
44. M.S. Wechsler, D.S. Lieberman and T.A. Read, Trans. A.I.M.E., (1953), 197, 1503
45. J.S. Bowles and J.D. Mackenzie, Acta Met., (1954), 2, 129, 138, 224
46. J.D. De Philippi, Ph.D. Thesis, Carnegie Inst. of Tech., Pittsburgh, Pa., 1965
47. A.J. Bogers and W.G. Burgers, Acta Met., (1964), 12, 255
48. C. Zener, Elasticity and Anelasticity of Metals, Chicago University Press, Chicago, (1948), 19
49. Z. Nishiyama, Sci. Rept. (Tohoku Univ. Sendai), (1934), 23, 637
50. M.A. Jaswon, Inst. of Metals Monograph No. 18, (1956), 173
51. P.M. Kelly and J. Nutting, J.I.S.I., (1961), 197, 199
52. H. Haneman, H. Holman and H.J. Wiester, Archiv fur Eisenhüttenwesen, (1932), 6, 199
53. T. Honma, Journal of the Japanese Inst. of Metals, (1957), 21, 263
54. A.R. Entwistle and J.A. Feeney, Inst. of Metals Special Report No. 33, (1969), 156
55. T.O. Ziebold and R.E. Ogilvie, Anal. Chem., (1964), 36, 322
56. L. Kaufman and H. Nesor, Zeitschrift fur Metallkunde, (1973), 64, 249
57. J.C. Fisher, Trans. A.I.M.E., (1949), 185, 688
58. L. Kaufman, Personal communication, (1976)
59. O. Krisement, E. Houdrement and F. Wever, Revue de Metallurgie, (1954), 51, 401
60. M. Cohen, E.S. Machlin and V.G. Paranjpe, Thermodynamics in Physical Metallurgy, ASM, Cleveland, Ohio, (1949), 242
61. R.L. Patterson and C.M. Wayman, Acta Met., (1966), 14, 347
62. T. van Karman, NDRC Report A29, OSRD 365, (1942)

63. G. Thomas, Met. Trans., (1971), 2, 2373
64. W.S.Owen, F.J. Schoen, and G.R. Srinivasan, Phase Transformations, ASM, Metals Park, Ohio, (1970), 157
65. J.W. Christian, Iron and Steel Inst. Special Report No. 93, (1965), 1
66. K. Shimizu and Z. Nishiyama, Met. Trans., (1972), 3, 1055
67. R.H. Bush and J.C. Bokros, Acta Met., (1964), 12, 102
68. A.S. Tetelman and A.J. McEvily, Fracture of Structural Materials, John Wiley and Sons, New York, (1967), 180
69. R.F. Rolsten, Trans. N.Y. Academy of Sciences, (1974), 36, 416
70. R.A. Graham, D.H. Anderson and J.R. Holland, J. Appl. Phys., (1967), 38, 223
71. Technical Datasheet for "Compensator 30", Carpenter Technology, Carpenter Steel Division
72. G. Hausch and H. Warlimont, Phys. Letters, (1972), 41A, 437
73. G.B. Olson and M. Cohen, J. Less Common Metals, (1972), 28, 107
74. G.F. Bolling and R.H. Richman, Phil. Mag., (1969), 19, 247
75. T. Maki and C.M. Wayman, First J.I.M. International Symposium, Kobe, Japan, (1976), (in press)
76. W.T. Read Jr., Dislocations in Crystals, McGraw-Hill, New York, (1953), 155
77. J.F. Breedis, Trans. A.I.M.E., (1964), 230, 1583
78. J.P. Hirth and J. Lothe, Theory of Dislocations, McGraw-Hill, New York, (1968), 280
79. S. Jana and C.M. Wayman, Met. Trans., (1970), 1, 2815
80. B.C. Muddle, P. Krakulis and J.S. Bowles, Acta Met., (1969), 17, 371
81. D.P. Dunne, J.S. Bowles, Acta Met., (1969), 17, 201
82. A. J. Morton and C.M. Wayman, Acta Met., (1966), 14, 1567
83. D.P. Dunne and C.M. Wayman, Met. Trans., (1973), 4, 137, 147

84. D.P. Dunne and C.M. Wayman, Met. Trans., (1973), 4, 147
85. G.B. Olson and W.S. Owen, First J.I.M. International Symposium, Kobe, Japan, (1976), (in press)
86. G.V. Kurdjumov, J. Metals, (1959), 11, 449
87. H. Pops and T.B. Massalski, Trans. A.I.M.E., (1964), 230, 1662
88. M.K. Korenko, Sc.D. Thesis, M.I.T., Cambridge, Ma., 1973
89. T. Maki, S. Shimooka, S. Fujiwara and I. Tamura, Trans. J.I.M., (1975), 16, 35
90. M. Hillert, Acta Met., (1958), 6, 122
91. L. Kaufman, Sc. D. Thesis, M.I.T., Cambridge, Mass, 1955
92. R.G.B. Yeo, Trans. A.S.M., (1964), 57, 48
93. R.J. Salzbrenner, Personal communication (1976)
94. J.P. Hirth and J. Lothe, Theory of Dislocations, McGraw-Hill, New York, 1968, 196, 216
95. J.D. Eshelby, Roy. Soc. London Proc., (1957), A241, 376
96. V. Raghavan and M. Cohen, Acta Met., (1972), 20, 779
97. S.A. Novikov, V.A. Sinitsyn, A.G. Ivanov and L.V. Vasil'yev, Fiz. Metal. Metalloved., 21, 452, (English tr. 21, No. 3, 135)
98. M. Umemoto and W.S. Owen, Met. Trans., (1974), 5, 2041
99. T. Maki, S. Shimooka and I. Tamura, Met. Trans., (1971), 2, 2944
100. G. Krauss Jr. and M. Cohen, Trans. A.I.M.E., (1963), 227, 278
101. O.P. Maksimova and A.I. Nikonorova, Problems of Metallography and the Physics of Metals, Fourth Symposium, (1955), 69, (AEC tr 2924)
102. Ya.M. Golovchiner and Yu.D. Tyapkin, Problems of Metallography and the Physics of Metals, Fourth Symposium, (1955), 141, (AEC tr 2924)
103. G. Sachs and J.W. Spretnak, Metals Technology, (1940), 7, TP 1246
104. R.B.G. Yeo, Trans. A.I.M.E., (1963), 227, 884

Gerald Albert Knorovsky was born in Chicago, Illinois on Oct. 19, 1949. His education through high school took place in that city's public school system. Graduating from Gage Park High School in 1966, he entered the Illinois Institute of Technology, majoring in Metallurgical Engineering. While at I.I.T., he participated in its Junior Year Abroad program, spending his junior year at the Institut National des Sciences Appliquees, Villeurbanne, France. After graduating from I.I.T. in 1970, he came to M.I.T. in Sept. 1970. At M.I.T. he was a Teaching Assistant until June 1972 and then became a Research Assistant. He married Margery Zinser in July 1971, and a son, Matthew, was born in May, 1972.

After receiving his doctorate, he plans to move to Albuquerque, New Mexico, where he has accepted a position at Sandia Laboratories.